Hybrid Kerosene-Hydrogen Flames Modeling and Topology Analysis

From a Computational Perspective

D.T.A. Tavernier

Thesis Report

Monday 6th July, 2026

Delft University of Technology

TU Delft Ergon research

Hybrid Kerosene-Hydrogen Flame Modeling and Topology Analysis

From a Computational Perspective

by

D.T.A. Tavernier

to obtain the degree of Master of Science

at the Delft University of Technology,
to be defended publicly on **20-07-2026** at **14:00**.

Thesis committee:	Prof.dr. A.Gangoli Rao	TU Delft, Chair
	Dr.ir. A.H.van Zuijlen	TU Delft, External Examiner
	Dr. F.De Domenico	TU Delft, Supervisor
	Dr. L.Palanti	Ergon Research s.r.l, Supervisor
	Dr. L.Mazzei	Ergon Research s.r.l, Supervisor

Place: Faculty of Aerospace Engineering, Delft

Student number: 5640539

Cover: Geometrical shape associated with a wrinkled flame, basis of the image is adapted from https://www.freepik.com/app

TU Delft Ergon research

Preface

Initially, I chose to study engineering to develop skills that could help address pressing global challenges. The existential threat that climate change poses to humanity is undoubtedly one of the most complex and urgent problems facing society today. Therefore, I am proud to have contributed to a project that advances sustainability.

I want to express my sincere gratitude to Dr. Lorenzo Mazzei for granting me this opportunity, which allowed me to work under the supervision of Dr. Lorenzo Palanti. I am deeply thankful to him for introducing me to the fascinating field of computational combustion, for his guidance and support throughout this thesis, and for his contribution to my development as an engineer. I am also grateful to my supervising professor, Dr. Francesca de Domenico, for her enthusiasm in taking on this project and for her continuous guidance throughout the thesis.

This thesis brought me to Florence, where I had the opportunity to experience life in this beautiful city and be part of an Italian office, which was a unique, valuable, and enriching experience. To everyone in the office who made me feel welcome: thank you for including me, for the sporting activities, for the adventures, and please, take good care of the cave.

To Mickey, with whom I shared the experience of moving to Florence and living together for the first time. You have been a great source of support during my thesis, and I greatly enjoyed exploring Florence and Italy together. Thank you.

This work also marks the end of my time as a student. I am grateful for the friends I have made during this period—friends who encouraged me to persevere when needed and to celebrate successes together. I am especially grateful for the group of friends I met during my bachelor's thesis in Amsterdam, with whom I also pursued the pre-master, supporting each other throughout. The same gratitude goes to the friends I met during my time in Delft; thank you for enriching this period of my life.

Finally, leaving student life also marks the conclusion of my time in the education system. I would like to express my deepest gratitude to my parents for their unconditional encouragement, support, and guidance throughout this journey, always having my best interests at heart. This work is dedicated to you.

Dries Tavernier
Monday 6th July, 2026

Contents

List of Figures

List of Tables

List of Symbols and Abbreviations

Symbols

Latin Symbols

A_f	Frontal area of a particle
A_T	Sectional area
$a_{C,k}, a_{H,k}, a_{O,k}$	Atom count (C, H, O) in species k
$a_{C,\text{kero}}, a_{H,\text{kero}}$	Atom count (C, H) in kerosene surrogate
c	Progress variable
C_d	Drag coefficient
D	Molecular diffusivity
D'	Thickened-flame diffusivity
D_{lam}	Laminar diffusion term
D_{turb}	Turbulent diffusion term
D_{32}	Sauter Mean Diameter
d_p	Particle diameter
E_a	Activation energy
E	Efficiency Function
f_{SBES}	SBES shielding function
F	Thickening Factor
$\vec{F}$	External force on particle
FH	Flame Height
FI	Flame Index
$\text{FI}_{\text{C}_{11}\text{H}_{22}}$	Flame Index, kerosene
FI_{H_2}	Flame Index, hydrogen
FI_{m_f}	Multi-fuel Flame Index
$\vec{g}$	Gravitational acceleration
h	Heat transfer coefficient
H_2	Hydrogen
H_2O	Water / Water vapor
HPS, HPS_g	(Global) Hydrogen Power Share
HRR, HRR_{max}	(Max) Heat Release Rate
k	Reaction rate constant
LHV	Lower Heating Value
LoH	Lift-off Height
M_i, M_H, M_C	Atomic mass (element i, H, C)
$\dot{m}$	Mass flow rate
m_l	Liquid fuel mass flow rate
m_p	Particle mass
n	Temperature dependence exponent
N	Thickening constant
$n_{i,k}$	Atom count of element i in species k
NO	Nitrogen Monoxide
NO_x	Nitrogen Oxides
OH	Hydroxyl radical
OH^*	Excited hydroxyl radical
P	Pressure
q	Rosin–Rammler spread parameter
$\dot{q}$	Heat flux
Q	Cumulative droplet volume fraction
R	Universal gas constant
Re, Re_Δ	(Sub-grid) Reynolds number
S_L	Laminar flame speed
$\mathcal{S}$	Flame sensor value
T, T_∞	Temperature, ambient temperature
Ta	Takeno number
t_{wall}	Artificial wall thickness (TCR)
u_Δ	Turbulent velocity at scale Δ
$\vec{u}, \vec{u}_p$	Fluid, particle velocity
V	Particle volume
w	Particle–fluid relative velocity
$W_{\text{H}_2}, W_{\text{kero}}, W_k$	Molar weight (H_2, kero, species k)
X	Representative diameter (R–R)
$\vec{X}$	Particle position vector
Y_i	Species mass fraction
y^+	Non-dimensional wall distance
Z_i, Z_H, Z_C	Elemental mass fraction (elem. i, H, C)
Z_{H,H_2}	Elemental H from H_2 fuel
$Z_{H,\text{kero}}$	Elemental H from kerosene

Greek Symbols

α, α_g	(Global) hydrogen mass fraction
β	Flame sensor exponent
β_{fuel}, β_{ox}	Fuel/oxidizer Bilger contributions
Γ	Gamma function parameter
Δ	Local mesh size / filter scale
ΔP	Pressure drop
$\delta_l, \delta_l^{\text{TFM}}$	Laminar (thickened) flame thickness
μ, μ_L	Dynamic viscosity (gas, liquid)
∇	Gradient operator
Ξ	Flame wrinkling

ξ, ξ_{st}	(Stoichiometric) mixture fraction
ρ, ρ_A, ρ_p	Density (fluid, gas/air, particle)
σ_L	Surface tension of liquid
τ_{ij}	Stress tensor
τ_r	Particle relaxation time
ϕ, ϕ_g	(Global) equivalence ratio
Ω, Ω_0	Flame sensor parameter, reference value
$\bar{\omega}$, $\bar{\omega}'$	Mean reaction rate (thickened)
$\dot{\omega}_k$, $\dot{\omega}'_k$	Species reaction rate (thickened)

Abbreviations

AAI	Axial Air Injection
AFR, AFR_{st}	(Stoichiometric) Air-Fuel Ratio
AIAA	American Institute of Aeronautics and Astronautics
ALR	Air-to-Liquid mass flow Ratio
AS	Anchored & Stable
ASC	Axially Staged Combustor
BC	Boundary Condition
CAD	Computer-Aided Design
CDC	Colourless Distributed Combustion
CFD	Computational Fluid Dynamics
CHT	Conjugate Heat Transfer
CRZ	Center Recirculation Zone
DAC	Dual Annular Combustor
DDES	Delayed Detached Eddy Simulation
DNS	Direct Numerical Simulation
DPM	Discrete Phase Model
DTF	Dynamic Thickened Flame
EDC	Eddy Dissipation Concept
EDC-PaSR	Eddy Dissipation Concept with Partially Stirred Reactor
EU	European Union
EXP	Experimental
FGM	Flamelet Generated Manifold
GFO	Gradient Fuel-Oxidizer
HOPE	Hydrogen Optimized multi-fuel Propulsion system for clean and silEnt aircraft
HPS	Hydrogen Power Share
HSD	Hydrogen Share Definition
ICAO	International Civil Aviation Organization
IDT	Ignition Delay Time
IEA	International Energy Agency
IPCC	Intergovernmental Panel on Climate Change
IRENA	International Renewable Energy Agency
IRZ	Inner Recirculation Zone
LBO	Lean Blow-Off
LDI	Lean Direct Injection
LDV	Laser Doppler Velocimetry
LEAF	Lean Azimuthal Flame
LES	Large Eddy Simulation
LFL	Lean Flammability Limit
LRZ	Local Recirculation Zone
LS	Lifted & Stable
LTO	Landing and Take-Off (cycle)
LU	Lifted & Unstable
ORZ	Outer Recirculation Zone
PDF	Probability Density Function
PFR	Product Formation Rate
PRZ	Pilot Recirculation Zone
QL	Quasilaminar
RANS	Reynolds-Averaged Navier-Stokes
RFL	Rich Flammability Limit
SAF	Sustainable Aviation Fuel
SBES	Stress-Blended Eddy Simulation
SC	Solid-Cone (atomizer)
SGS	Subgrid-Scale
SMD	Sauter Mean Diameter
SNR	Signal-to-Noise Ratio
SST	Shear Stress Transport
TAPS	Twin Annular Premixed Swirler
TCC	Thermal Contact Conductance
TCI	Turbulence-Chemistry Interaction
TCR	Thermal Contact Resistance
TFM	Thickened Flame Model
TU Delft	Delft University of Technology
UHBR	Ultra High Bypass Ratio
UHC	Unburned Hydrocarbons
URANS	Unsteady Reynolds-Averaged Navier-Stokes
VU	Lifted & Very Unstable
WALE	Wall-Adapting Local Eddy-viscosity

Summary

Modern aviation depends heavily on fossil fuel, which causes detrimental effects on the climate. A shift towards carbon-free aviation is therefore desired, with hydrogen representing one of the possible enablers currently being explored. The push towards sustainable aviation using hydrogen is, among other factors, limited by operational restrictions due to existing infrastructure being dedicated to kerosene combustion. An aircraft capable of operating exclusively on pure hydrogen would face significant operational limitations, as only a limited number of airports currently provide hydrogen refueling infrastructure. This constraint would substantially restrict its operational flexibility, thereby reducing its competitiveness compared with existing kerosene-based aviation systems. The HOPE (Hydrogen Optimized multi-fuel Propulsion system for clean and silEnt aircraft) is a project to overcome this limitation by developing a multi-fuel combustor. A fuel-flexible system bridges the gap, an aircraft can use the existing kerosene infrastructure today, and switch to hydrogen wherever refueling is available, supporting a gradual infrastructure transition rather than requiring an abrupt one. This study is conducted within the framework of the HOPE project, with the objective to advance the development of the HOPE combustor as well as to contribute to the knowledge on multi-fuel combustion. More specifically, this work focuses on how various fuel blends of kerosene and hydrogen affect the flame topology and explores how the design performs under limiting engine operating conditions.

The current HOPE combustor is manufactured and tested in the Delft University Sustainable Propulsion Lab under reduced power compared to aircraft operating conditions and is placed in an ambient environment. High-fidelity Stress-Blended Eddy Simulations (SBES) were performed to reproduce this test setup, resulting in validated simulations which can be utilized to further understand the interaction between kerosene and hydrogen. The simulations showed that hydrogen combusts upstream of kerosene, enhancing kerosene evaporation and thereby promoting its subsequent combustion downstream.

The validity of the numerical approach was further assessed by comparing the simulation results with the available experimental data. The SBES simulation reproduces the pure hydrogen case well. For pure kerosene, the predicted flame shape broadly matches experiments, though notable discrepancies remain. The multi-fuel cases show premature flame anchoring at the mixing tube outlet, with the SBES simulations predicting an attached flame at lower hydrogen contents, compared to the experiments. The premature anchoring is most likely caused due to the adiabatic boundary conditions, which result in artificially elevated temperatures (near the walls) exceeding the autoignition temperature of hydrogen. Consequently, hydrogen can autoignite independently of the kerosene combustion process, resulting in flame anchoring at the mixing tube outlet. Another prospective improvement concerns the spray. The combustor design employs a solid-cone SIMPLEX atomizer, which exhibits characteristics of both hollow-cone and solid-cone sprays, whereas the SBES simulations were performed using a purely solid-cone spray model. The discrepancies between the simulations and the experiments are expected to be minimized even further by combining a hollow-cone/solid-cone spray, more accurately representing the experimental spray conditions.

The exploration of the HOPE-combustor performance in actual limiting operating conditions has been performed using lower-fidelity simulations due to restrictions imposed by the computational cost associated with simulating the engine operating conditions. The most critical operating condition is a take-off powered exclusively by hydrogen, as this condition is associated with the highest laminar flame speed. Consequently, the risk of upstream flame propagation is increased, potentially resulting in structural degradation. The simulation showed that an unfeasible pressure drop was present in the current design. Therefore, the swirler design was scaled-up, reducing the pressure drop across the swirler; however, this resulted in flame stabilization in the nozzle of the swirler. A design adjustment will be proposed while also raising questions regarding the objective operational requirements of the system. A possible solution is to introduce hydrogen diffusion flames resistant to flashback and upstream propagation to enable operation under pure hydrogen take-off conditions, accepting an NOx penalty. However, it can be argued that if such a pure hydrogen take-off capability is required, it may necessitate complex and costly systems for a marginal operating case, given the dominance of kerosene-based infrastructure.

1

Introduction

This chapter explains the need for the research by outlining the broader context of aviation's dependence on fossil-based propulsion and the associated environmental, geopolitical, and technological challenges. Background on the HOPE project will be provided, as this research is conducted within this initiative.

1.1. The Imperative of Sustainable Aviation

The era of industrialization began with the invention of the steam engine, which brought great prosperity. The heart of this technology is the combustion process. In this day and age, fossil fuel remains dominant in the energy and transportation industries. The share of coal, oil and natural gas in global energy supply has stuck around 80% for decades according to the IEA (International Energy Agency) [1]. In aviation, fossil fuel is even more dominant. The energy consumption of the global aviation sector is nearly exclusively fossil fuel-powered, according to the IRENA (International Renewable Energy Agency)[2].

Although combustion-based technologies have fueled the modern lifestyle and aviation would doubtlessly never have taken off without them, they possess a fundamental drawback. The emissions from fossil combustion have caused a global increase in surface temperature observed between 2011 and 2020 relative to the pre-industrial period. As a result, many weather and climate extremes have been observed across the globe [3]. Furthermore, according to the WHO (World Health Organization), this shift affects the physical environment as well as all aspects of both natural and human systems. The vast majority of anticipated health impacts of climate change are negative and are predicted to far outweigh potential positive health effects (e.g., lower health risks from extreme cold) worldwide [4]. More specifically, climate change will cause an increased risk of morbidity and mortality due to undernutrition in poorer regions, reduced labor productivity, heat waves, and associated fires [5].

Beyond environmental concerns, the transition to sustainable aviation is of utmost importance to the strategic autonomy of Europe. The European Union's reliance on imported fossil fuels creates economic and geopolitical vulnerabilities, as noted in the Versailles Declaration [6]. By developing sustainable technologies, Europe aims to decouple its transport sector from external energy dependencies while securing its technological leadership and intellectual property [7]. Therefore, developing these sustainable technologies is essential to maintain or strengthen the continent's industrial competitiveness in a global market [8].

Kerosene-based propulsion remains the standard for aviation, yet it drives both environmental degradation and geopolitical energy vulnerability. According to ICAO projections, global air passenger demand is expected to maintain a steady growth rate of approximately 4% per year, potentially reaching over 10 billion passengers by 2050 [9]. The demand for aviation services is growing, while emissions and fossil fuel imports are expected to decrease in absolute terms. Therefore, to simultaneously adhere to ICAO's vision, "A safe, secure and sustainable international civil aviation system that connects the world for the benefit of all nations and people" [10], and to the EU goals of strategic autonomy, developing and improving clean aviation technologies is a fundamental prerequisite.

1.2. Objectives of HOPE

Hydrogen can be produced through various pathways, one of which is green hydrogen. Green hydrogen refers to hydrogen generated via electrochemical water splitting; when the electricity input is sourced from renewable energy, both hydrogen and oxygen are produced without direct CO_2 emissions [11]. Electricity production can be ensured by European renewable production facilities (e.g. solar, wind energy or nuclear), therefore through hydrogen combustion, Europe can also control its availability to aviation fuel. However, several challenges are ahead regarding (pure) hydrogen operations. The production, storage, transport, and onboard integration require further development activities [12]. Moreover, the adoption of hydrogen technology in aviation is hindered by a circular dependency: the commercialization of fueling infrastructure depends on sufficient hydrogen demand, while the widespread use of hydrogen-powered vehicles depends on the availability of that very infrastructure [13]. Fuel flexible operations where both hydrogen and kerosene can be utilized both independently and simultaneously breaks the dilemma. Several European development projects have started developing fuel flexible technologies [14, 15, 16].

The current research is part of HOPE (Hydrogen Optimized multi-fuel Propulsion system for clean and silEnt aircraft) [17], which is one of the projects that advances fuel-flexible technologies in aviation. HOPE is a consortium consisting of aviation-related companies and research institutes. The thesis will be a combined effort between the TU Delft and Ergon Research s.r.l. This research is supported by the Horizon Europe research and innovation program and co-funded by UK Research and Innovation (UKRI) under the UK government's Horizon Europe funding guarantee. The main objectives of HOPE are listed below:

1. Minimize the combustion and noise emissions during landing and takeoff (LTO), hence the impact on air quality and noise annoyance near airports, without the trade-off of cruise emissions

2. Retrofit the existing aircraft configuration, allowing the substantial emission reduction to be achieved within a short time

3. De-risk the use of hydrogen solely in existing tube-wing aircraft configurations

4. Smoothens aviation's energy transition through assessment and exploitation of several greener propulsion technologies at different maturity levels.

In measurable terms HOPE aims at ensuring the following objectives: LTO NOx: -50%, CO: -50%, soot: -80%, perceived noise: -20% (3 dB per operation), and climate impact: -30%, compared to state-of-the-art technology in 2020 (A320neo). One of the tasks concerning HOPE is to model, experiment, and demonstrate for the first time a low emission multi-fuel combustion technology burning H_2+kerosene for future UHBR (Ultra High Bypass Ratio) turbofan engines. The thesis is developed in accordance with this objective.

2

Theoretical Background

Throughout this research, several widely established theories and methods have been employed; therefore, they are treated as supporting tools rather than the primary focus of the study. Accordingly, an overview of these subjects is provided in this chapter.

2.1. One-step Stoichiometric Combustion of Hydrogen and Kerosene

Combustion is an exothermic chemical reaction that increases the temperature of the flow and its surroundings, thereby providing the energy conversion that forms the basis of gas turbine power generation. Chemical reactions occur when fuel and oxidizer molecules collide with sufficient energy and appropriate orientation [18]. Stoichiometrically balanced reactions for hydrogen and kerosene combustion are presented in Table 2.1. During combustion, reactants are consumed while products are formed. The exact composition of kerosene may vary; however, the carbon number typically ranges from C_9 to C_{13} [19]. In scientific literature, kerosene is commonly represented using surrogate mixtures [20]. In the present work, kerosene is modeled as $C_{11}H_{22}$.

Table 2.1: Stoichiometric combustion of hydrogen and kerosene

Fuel	**Molecule**	**Balanced Reaction**
Hydrogen	H_2	$2\,H_2 + O_2 \rightarrow 2\,H_2O$
Kerosene (Jet A)	$C_{11}H_{22}$	$2C_{11}H_{22} + 33O_2 \rightarrow 22CO_2 + 22H_2O$

The stoichiometric condition refers to the state in which fuel and oxidiser are present in exact proportions such that both are completely consumed without excess fuel or oxidiser [18]. This condition corresponds to a specific fuel-to-oxidiser mass flow rate ratio. The equivalence ratio is defined as the ratio of the actual fuel-to-oxidiser mass flow rate to the stoichiometric fuel-to-oxidiser mass flow rate, as given in Equation 2.1.

$$\phi = \frac{(\dot{m}_{\text{fuel}}/\dot{m}_{\text{oxidizer}})}{(\dot{m}_{\text{fuel}}/\dot{m}_{\text{oxidizer}})_{\text{stoichiometric}}} \tag{2.1}$$

2.2. Basic Flame Types

Various types of flames can be distinguished based on their physical and chemical characteristics. A first classification relates to the phase of the reactants. In homogeneous flames, both fuel and oxidiser are in the same phase, such as in methane–air combustion, both gaseous. In heterogeneous flames, such as spray combustion, liquid fuel interacts with gaseous air. In addition to phase considerations, combustion processes may be either approximately steady or highly unsteady, depending on operating conditions.

Another important way to classify combustion systems is based on mixing behaviour. Figure 2.1 illustrates this classification. In many practical combustion systems, fuel and oxidiser enter the reaction zone separately and mix while reacting. This combustion mode is referred to as non-premixed or diffusive. In contrast, premixed combustion occurs when fuel and oxidiser are already mixed prior to entering the reaction zone.

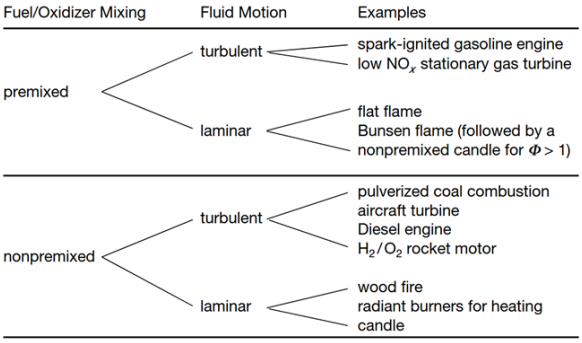

Figure 2.1: Example of combustion systems ordered with respect to premixedness and flow type [21]

Flame types can be further subdivided into laminar and turbulent regimes. In the case of the HOPE combustor, the flow is expected to be highly turbulent. Nevertheless, laminar flame theory remains relevant, as it provides the fundamental basis for understanding and modeling turbulent combustion.

2.2.1. Premixed Flames

Laminar premixed combustion in a duct is shown in Figure 2.2a. The combustion process propagates through a thoroughly premixed fuel–air mixture. This propagation speed is called the laminar flame speed S_L. The freely propagating laminar flame configuration of CANTERA is used in this research and represents an idealised premixed system in a duct without wall effects. The corresponding structure of such a laminar flame reaction zone is shown in Figure 2.2b. The combustion reaction zone, or flame, is typically very thin, of the order of a few millimetres for hydrocarbon fuels under ambient conditions. The thickness of the reaction zone in the laminar regime is referred to as the laminar flame thickness δ_l. In the preheat zone, the temperature of the unburnt mixture rises gradually from the mixture temperature towards the reaction zone. As the temperature approaches the ignition temperature of the fuel, chemical reactions accelerate rapidly, marking the onset of the flame front. Within the flame, the reaction rate increases sharply and subsequently decreases as fuel and oxidiser are consumed and combustion products are formed. The laminar flame speed strongly depends on the chemical reaction rate and, consequently, on the flame temperature and equivalence ratio. The maximum flame temperature is reached for slightly rich mixtures, resulting in the highest flame speeds.

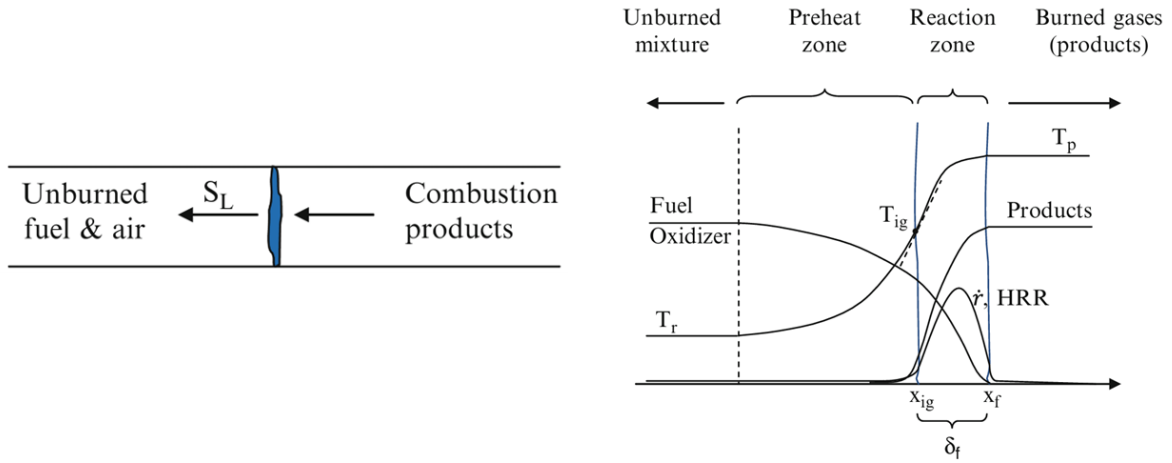

(a) Representation of the duct

(b) Premixed flame structure within the duct

Figure 2.2: Sketch of a premixed flame propagating [22]

Increasing the temperature of the unburned mixture increases the flame speed primarily because chemical reaction rates increase significantly with temperature, while transport processes such as thermal diffusion also change and can further support faster flame propagation. This temperature effect is shown in Figure 2.3a, which also indicates an increase in flame speed with equivalence ratio in the lean regime. For most hydrocarbon–air mixtures, increasing the pressure decreases the laminar flame speed. Higher pressure reduces thermal diffusivity and therefore slows flame propagation. The pressure effect on the laminar flame speed for hydrogen–air mixtures is shown in Figure 2.3b.

As a combustible mixture deviates from stoichiometric conditions, becoming either too lean or too rich, the flame temperature decreases, and the laminar flame speed drops significantly. Eventually, combustion can no longer be sustained, and the flame is extinguished. The corresponding limits of flammability are referred to as the lean flammability limit (LFL) and the rich flammability limit (RFL).

Laminar premixed flame speed is primarily influenced by equivalence ratio, reactant temperature, pressure, and mixture composition. Higher reactant temperatures increase flame speed, whereas increasing pressure typically reduces it for hydrocarbon flames, although temperature remains the dominant influence.

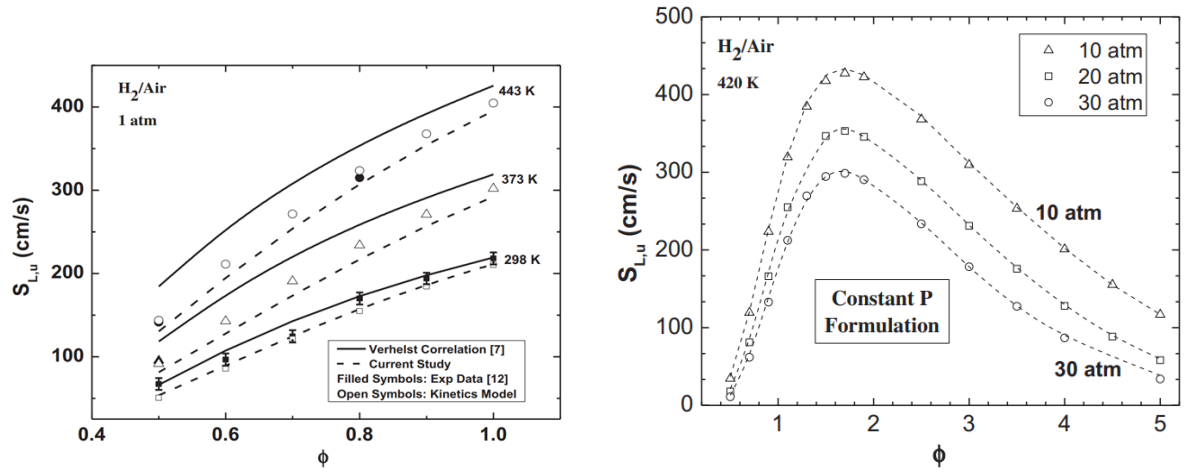

(a) Effect of unburned gas temperature on S_L

(b) Effect of pressure on S_L

Figure 2.3: Dependence of laminar flame speed S_L on thermodynamic conditions for hydrogen-air mixtures [23]

Experimental observations show that premixed flames propagate significantly faster in turbulent flows than in laminar flows. The main reason for this enhancement is that turbulence increases the transport of momentum, heat, and mass through the motion of eddies. A turbulent flame speed is defined to represent the average propagation rate of a flame interacting with turbulent flow structures. The turbulent flame speed is often approximated using the laminar flame speed S_L and a characteristic turbulence velocity scale.

Furthermore, as a premixed flame propagates upstream towards the unburnt mixture, it may reach the injector and cause damage to the system. This phenomenon is known as flashback. Flashback occurs when upstream flame propagation leads to the flame travelling against the flow, which happens when the unburnt flow velocity is lower than the turbulent flame speed.

2.2.2. Non-premixed Flames

Non-premixed flames (or diffusion flames) are characterised by the separation of fuel and oxidiser prior to combustion [22]. Chemical reactions occur in regions close to stoichiometric conditions, where temperatures are relatively high. The mixture composition varies throughout the flame and flow field due to the spatial separation of fuel and oxidiser. The stability characteristics of diffusion flames are generally higher than those of premixed flames, as combustion is confined to the stoichiometric mixture fraction. Under turbulent conditions, the flame structure can become highly complex, as turbulent mixing enhances the interaction between fuel and oxidiser streams. Diffusion flames are not prone to flashback due to the spatial separation of reactants at the injector; however, they may exhibit less favourable emissions characteristics, such as higher soot formation and NOx production depending on operating conditions.

2.3. Liquid Fuel Atomization

Based on the preceding discussion, the liquid fuel primarily evaporates and burns before sufficient mixing can occur; consequently, a uniform mixture is not established prior to combustion. As a result, spray flames are predominantly diffusive in nature. The performance of liquid fuel combustion depends on the atomization process, which increases the specific surface area of the fuel, resulting in enhanced mixing and evaporation rates [24]. In most combustion systems, a reduction in mean fuel droplet size leads to higher volumetric heat release rates, easier ignition, a wider operating range, and lower exhaust pollutant emissions [25]. Spray combustion involves several stages and characteristic processes. Figure 2.4 shows a typical spray and its associated atomization and evaporation stages.

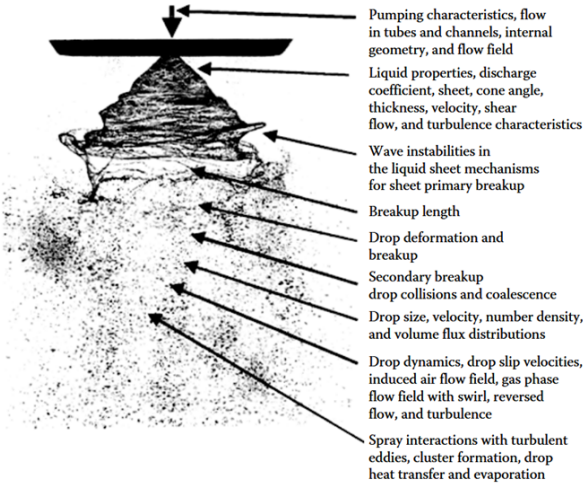

Figure 2.4: Example of a spray illustrating atomization characteristics [24]

The spray originates at the injection nozzle, where the liquid exits under conditions determined by injection pressure, internal geometry, and internal flow conditions. Subsequently, liquid sheet formation occurs as the liquid emerges from the nozzle and develops into a thin sheet. Primary instability then develops as the liquid sheet becomes unstable due to interaction with the surrounding air, shear forces, and turbulence, leading to the formation

of surface waves. Primary breakup occurs when these instabilities grow until the liquid sheet disintegrates into ligaments. The axial distance over which this occurs is referred to as the breakup length. Ligament and droplet formation follows, during which ligaments stretch and break into droplets, forming the initial droplet size distribution. After this stage, secondary breakup may occur, where larger droplets further disintegrate due to aerodynamic forces, while droplet collisions and coalescence may take place. Spray development describes the evolution of the spray into a cloud of droplets characterized by distributions of size, velocity, and number density. During droplet dynamics, droplets interact with the surrounding gas and are influenced by turbulence as well as large-scale flow structures such as swirl or recirculation. Finally, evaporation and mixing occur as droplets exchange heat with the surrounding gas, evaporate, and mix with air, which is essential for combustion processes.

2.3.1. Sauter Mean Diameter

The Sauter Mean Diameter (SMD), also denoted as D_{32}, is a characteristic droplet size widely used in spray and atomization analysis [24]. It is defined as given in Equation 2.2, where D_i represents the diameter of the i^{th} droplet.

$$D_{32} = \frac{\sum_i D_i^3}{\sum_i D_i^2} \tag{2.2}$$

The Sauter Mean Diameter represents the diameter of a droplet that has the same volume-to-surface-area ratio as the entire spray. This can be understood by noting that D_i^3 is proportional to droplet volume (or mass), while D_i^2 is proportional to droplet surface area. Thus, D_{32} can be interpreted as shown in formulation 2.3.

$$D_{32} = \frac{\text{Total droplet volume}}{\text{Total droplet surface area}} \tag{2.3}$$

This property makes D_{32} particularly important in processes involving mass transfer, evaporation, and chemical reactions. Since these processes occur at the droplet surface, a smaller D_{32} corresponds to a larger surface area per unit volume, leading to enhanced evaporation and reaction rates. Therefore, in atomization systems such as fuel injection, achieving a lower Sauter Mean Diameter is beneficial for improving mixing, combustion efficiency, and overall system performance.

2.3.2. Atomizers

An atomizer is a device that breaks a liquid into fine droplets (a spray), typically using high relative velocity between a liquid and a gas [24]. Different kinds of atomizers can be distinguished, and they are commonly grouped into three main classes. Pressure atomizers use the liquid pressure to force the fluid through a nozzle at high velocity, where the resulting velocity and turbulence induce primary breakup into droplets. Rotary atomizers rely on mechanical rotation, where the liquid spreads over a spinning disk and centrifugal forces lead to droplet formation. Airblast atomizers use the kinetic energy of a high-speed gas stream interacting with a slower liquid stream, producing fine droplets.

In this work, the focus is on pressure atomizers, and more specifically on the SIMPLEX atomizer. The concept of the simplex atomizer is shown in Figure 2.5a. The liquid is pressurized through a nozzle containing swirling vanes, which induce angular momentum to the flow and generate a rotating liquid sheet that forms a hollow-cone spray (see Figure 2.5b). The atomizer shown in Figure 2.5a is classified as a solid-cone SIMPLEX atomizer. In this configuration, a portion of the liquid bypasses the swirling vanes and is discharged directly into the flow field, leading to liquid saturation near the center of the cone.

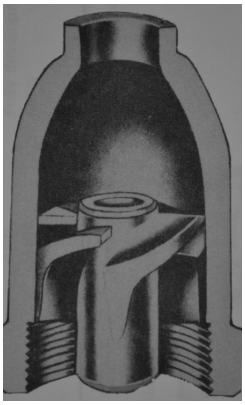

(a) SIMPLEX pressure atomizer producing a solid-cone and hollow-cone spray [24]

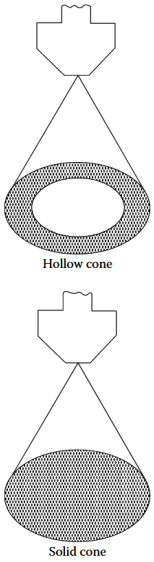

(b) Comparison between hollow cone and solid cone spray patterns [24]

The spray quality in pressure atomizers is strongly dependent on the pressure drop across the atomizer. Figure 2.6 illustrates the influence of pressure on spray quality. At low pressure levels, relatively large droplets are produced. The droplet diameter decreases as the pressure increases, eventually leading to the formation of a fine spray.

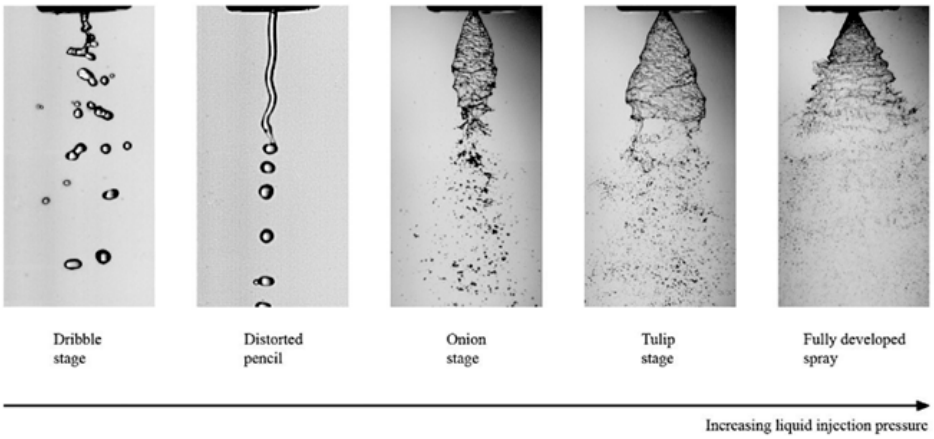

Figure 2.6: A simplex atomizer applied under various pressures, showing its relation with spray quality.[24]

2.4. Pollutant formation and modeling

Understanding the behaviour of pollutants in combustion is fundamental for their eventual reduction and the transition towards sustainability. Although pollutants are generated by all types of combustion systems, this study focuses specifically on pollutant formation in aeroengine combustors. Figure 2.7 illustrates the combustion process in terms of emissions of a kerosene-powered aeroengine. Kerosene fuel, consisting of carbon, hydrogen, and components, is burned in a jet engine. Contrail formation can subsequently occur due to the mixing of hot exhaust gases with cold surrounding air. The exhaust contains pollutants, which are intended to be minimized. Carbon dioxide is a pollutant; however, it is a product of hydrocarbon oxidation. Hydrogen combustion does not contain any carbon and is therefore free of carbon dioxide emissions. However, other by-products/pollutants are generated, which are harmful and can be reduced through a more efficient combustion process. For example, carbon monoxide is toxic and mainly affects the cardiovascular system. Nitrogen oxides NO_x contribute to lung irritation, reduced resistance to respiratory infections, and impaired lung function. Additionally, unburned hydro-

carbons (UHC) can irritate the eyes, along with neurological symptoms such as headaches and reduced memory. Furthermore, soot and sulfur oxides SO_x are associated with premature mortality and cardiovascular diseases [26].

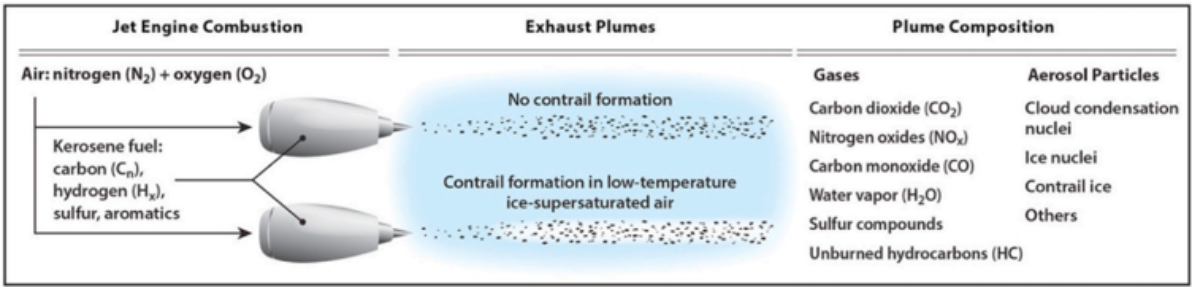

Figure 2.7: The pollutants of kerosene combustion [27]

2.4.1. NOx Emissions

NO_x emissions are formed through several distinct mechanisms [28]. In aircraft engine combustion, the majority of NO_x is generated in high-temperature regions where molecular nitrogen in the air reacts with oxygen. The primary formation pathway is thermal NO_x, which predominantly occurs at temperatures above 1850 K. This process can be described by the Zeldovich mechanism, which is represented by reactions (Equation 2.4)–(Equation 2.6) [28].

$$O + N_2 \rightleftharpoons N + NO \tag{2.4}$$

$$N + O_2 \rightleftharpoons O + NO \tag{2.5}$$

$$N + OH \rightleftharpoons NO + H \tag{2.6}$$

NO_x emissions can be partially controlled through appropriate combustion design. NO_x emissions are of considerable concern in hydrogen combustion due to increased local temperatures resulting from its higher reactivity compared to kerosene, which promotes thermal NO_x formation.

2.4.2. CO Emissions

CO is produced in one of the final steps of hydrocarbon fuel oxidation and is subsequently converted to CO_2, mainly through Equation 2.7. As noted in [28], CO emissions are influenced by three main factors. First, under rich combustion conditions, insufficient oxygen is available to fully oxidize CO, leading to higher emissions. Second, near the lean extinction limit, the burning rate is very slow, preventing complete oxidation within the available residence time. Finally, at high gas temperatures, product dissociation can occur, shifting the equilibrium in Equation 2.7 toward CO formation. Pure hydrogen combustion does not contain carbon and therefore does not produce CO under ideal conditions, assuming no contamination from oils or other carbon-containing substances.

$$CO + OH \rightleftharpoons CO_2 + H \tag{2.7}$$

2.4.3. Unburned Hydrocarbons and Soot

Unburned hydrocarbons (UHC) are gaseous hydrocarbon species originating from the fuel that escape complete oxidation during combustion. In some definitions, this category also includes partially oxidized hydrocarbons formed as combustion intermediates. Overall, UHC emissions consist of fuel molecules that are not consumed by the flame. Factors that increase the survival of these unreacted hydrocarbons contribute directly to UHC formation. Lower temperatures reduce reaction rates and combustion efficiency, thereby increasing UHC emissions. Similarly, flame quenching near walls and in gaps prevents complete combustion. Reduced residence time at high temperature also limits oxidation, increasing the likelihood of unburned hydrocarbons. Additionally, rich

mixtures (high equivalence ratios) promote UHC formation due to limited oxygen availability and a higher concentration of fuel molecules [22].

Soot, on the other hand, consists of solid carbon particles that form during the incomplete combustion of hydrocarbon fuels. It is produced mainly in fuel-rich regions where there is insufficient oxygen to fully oxidize the fuel. Under these conditions, fuel molecules break down, forming intermediate species that subsequently grow into soot particles. In pure hydrogen combustion, no carbon is present in the fuel; hence, H_2 is not a source of UHC or soot.

2.4.4. The Influence of Temperature and Mixture Properties on Emissions

Several factors influence emission formation, of which mixture properties and temperature are often dominant. These two factors are also highly interrelated, as illustrated in Figure 2.8. Mixture properties are represented by the equivalence ratio, while temperature peaks near the stoichiometric condition. The two regions on either side of the peak temperature (approximately the lean and rich regimes) typically exhibit monotonic behaviour (see Figure 2.8a). In Figure 2.8b, the typical behaviour of CO, NO_x, and UHC (HC in the figure) is shown. During lean combustion, CO and UHC emissions are significant. The relatively low temperatures lead to incomplete combustion, resulting in CO formation and an increased likelihood of unburned hydrocarbons. Near the stoichiometric condition, temperatures are high and hydrocarbon oxidation is largely complete, minimizing CO and UHC emissions. However, these high temperatures promote nitrogen oxidation, leading to increased NO_x formation. NO_x emissions then decrease with further increase of the equivalence ratio toward the rich side. As temperature decreases again under rich conditions, CO and UHC emissions increase. The figure suggests an optimal operating point on the lean side, just before significant nitrogen oxidation occurs and after the sharp reduction in CO and UHC emissions. One strategy to minimize emissions is to design combustion systems to operate predominantly within this optimal regime. A premixed flame enables locally lean operation with reduced peak temperatures and consequently lower thermal NO_x formation, whereas diffusion flames develop reaction zones at locally stoichiometric conditions.

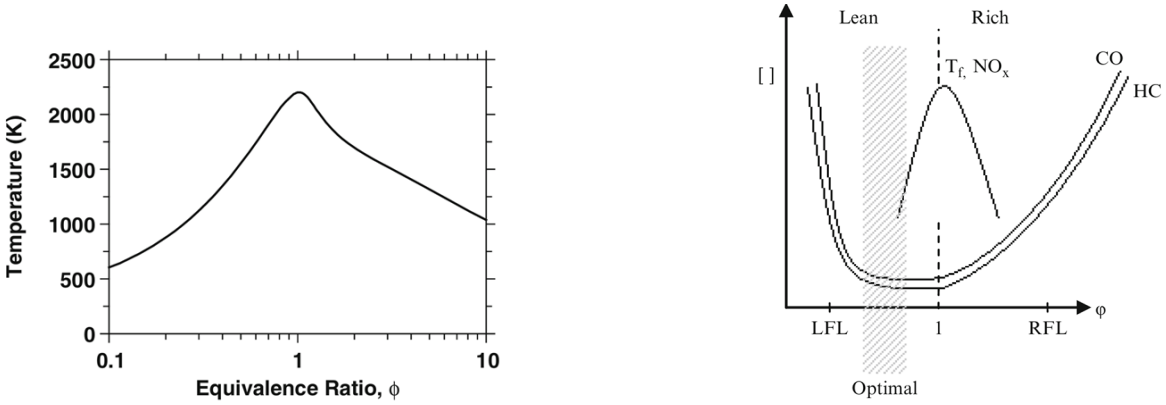

(a) Temperature and equivalence ratio

(b) Typical emissions as a function of equivalence ratio

Figure 2.8: Fundamental relationships between temperature, equivalence ratio, and emissions in combustion [22]

2.5. Reaction Mechanisms

The reaction mechanism contains all relevant information concerning the chemical interactions between species and the reactions involved. The rate of each reaction is determined by the rate constant and the concentrations of the reacting species. As an example, the consumption rate of species [A] is given in Equation 2.8.

$$\frac{d[A]}{dt} = -k[A]^a[B]^b[C]^c \tag{2.8}$$

Here, $[A]$, $[B]$, and $[C]$ represent the concentrations of the reacting species, k is the reaction rate constant, and a, b, and c are the reaction orders. The term $\frac{d[A]}{dt}$ represents the rate of change of species A. The negative sign indicates that species A is consumed during the reaction. The reaction rate depends on both the rate constant and

the concentrations of the reactants. The rate constant is defined in the reaction mechanism file and is typically expressed in terms of the pre-exponential factor A, the activation energy E_a, temperature T, and the universal gas constant R. The temperature dependence can additionally be modified through the exponent n. Pressure dependence is often not directly included in the Arrhenius expression (see Equation 2.9); instead, it is incorporated through third-body collision partners M, which represent surrounding gas molecules that collide with the reactants and thereby account for pressure effects via their concentration $[M]$.

$$k = AT^n \cdot \exp\left(-\frac{E_\mathrm{a}}{RT}\right) \tag{2.9}$$

In Table 2.2, part of the Z79 reaction mechanism is presented, describing the rate constant in terms of the pre-exponential factor A, the temperature exponent n, and the activation energy E_a. The table presents a subset of reactions included in the Z79 mechanism. The first group lists reactions associated with the kerosene surrogate $C_{11}H_{22}$, while the second group contains analogous reactions for H_2 fuel. The third group includes radical and intermediate species reactions. The final two groups describe the formation pathways of the one-step global products of kerosene and hydrogen combustion, namely H_2O and CO_2, respectively.

Table 2.2: Incomplete representation of the reactions in the Z79 reaction mechanism ($k = AT^n \exp(-E_a/RT)$). [29]

#	Reaction	A	n	E_a
	$C_{11}H_{22}$ fuel chemistry			
1	$C_{11}H_{22} + O_2 \rightarrow C_{11}H_{21} + HO_2$	2.00E+15	0.0	50150
4	$C_{11}H_{22} + HO_2 \rightarrow C_{11}H_{21} + H_2O_2$	2.12E+14	0.0	17690
	H_2 fuel chemistry			
6	$H_2 + O \rightarrow H + OH$	1.80E+10	1.0	8826
7	$H_2 + OH \rightarrow H + H_2O$	1.17E+09	1.3	3626
	Radical and intermediate chemistry			
12	$C_2H_3 + CH_4 \rightarrow C_2H_4 + CH_3$	3.02E+13	0.0	12580
5	$H + HO_2 \rightarrow 2\ OH$	1.50E+14	0.0	1004
	H_2O formation reactions			
15	$C_{11}H_{22} + OH \rightarrow C_{11}H_{21} + H_2O$	3.00E+07	1.9	58
17	$2\ OH \rightarrow H_2O + O$	6.00E+08	1.3	0
18	$HO_2 + OH \rightarrow H_2O + O_2$	2.00E+13	0.0	1000
19	$CH_3 + O \rightarrow CH_2O + H$	6.80E+13	0.0	0
	CO_2 formation			
22	$CO + OH \rightarrow CO_2 + H$	1.51E+07	1.3	-758

2.6. Swirl Stabilized Combustion

The airflow characteristics in the combustion chamber are of fundamental importance for flame stability [28]. A common method is to employ swirling flow, inducing recirculation of a portion of the hot combustion products, which mix with the unburnt mixture. The flow is rotated and, as a consequence, the static pressure decreases in the core. When the rotational strength of the flow is sufficiently high, flow reversal occurs. This phenomenon is also referred to as vortex breakdown and is illustrated in Figure 2.9a. Vortex breakdown occurs when the ratio of tangential to axial momentum, commonly referred to as the swirl number, exceeds a critical value. In Figure 2.9b, the flow field of a typical swirl-stabilised combustor is depicted. The swirling flow gives rise to an IRZ (Inner Recirculation Zone) and an ORZ (Outer Recirculation Zone). Between these regions, shear layers are formed, where the local flow conditions are favourable for flame anchoring.

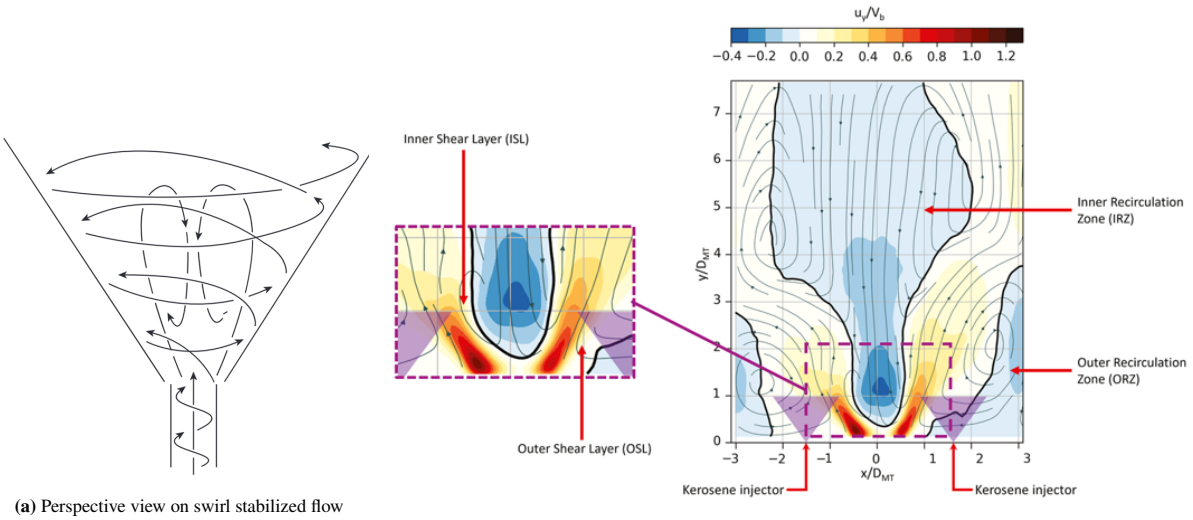

(a) Perspective view on swirl stabilized flow [28].

(b) Detailed planar view of a swirl stabilizing flow [30].

Figure 2.9: Swirl-stabilized flame and flow field.

2.7. Computational Fluid Dynamics

Computational Fluid Dynamics (CFD) is a numerical framework for solving the Navier–Stokes equations that govern fluid motion. Depending on how turbulence is treated, three main approaches are used: DNS, LES, and (U)RANS [31].

Direct Numerical Simulation (DNS) solves the full Navier–Stokes equations without any turbulence modeling. All turbulent scales are resolved explicitly, from the largest energy-containing eddies to the smallest dissipative scales. DNS requires very fine spatial and temporal resolution and is computationally feasible only for low Reynolds numbers and simple geometries. Large Eddy Simulation (LES) solves the spatially filtered Navier–Stokes equations. In LES, large turbulent structures are resolved directly, while the effects of smaller, subgrid-scale motions are modeled using a subgrid-scale model. LES provides a balance between accuracy and computational cost and is suitable for capturing unsteady, large-scale turbulent dynamics. Reynolds-Averaged Navier–Stokes (RANS) solves time-averaged Navier–Stokes equations, where all turbulent fluctuations are modeled using turbulence models. It provides only mean flow quantities and does not resolve instantaneous turbulence. RANS is computationally efficient. Unsteady RANS (URANS) extends RANS by retaining time dependence of the mean flow, allowing prediction of large-scale unsteady behaviour while still modeling all turbulence.

Research comparing Large Eddy Simulation (LES) with Reynolds-Averaged Navier–Stokes (RANS) models and experimental data for aeronautical gas turbine combustors demonstrates the significant potential of LES for industrial design [32]. LES, by accurately resolving unsteady turbulent reacting flows, provides critical information such as flame–turbulence interaction, flame–acoustic coupling, and large-scale mixing dynamics that are not accessible using conventional RANS methods. Compared to RANS, LES predicts sharper mean temperature fields and higher peak temperatures in reacting zones, a difference attributed to the inherent smoothing (or numerical diffusion) associated with RANS modeling. A comparison between URANS and LES for combustion systems

was performed by [33]. The study highlighted that LES is associated with a significant computational cost due to the requirement for very fine near-wall resolution in all directions. A common strategy to mitigate this limitation is the use of hybrid LES–RANS approaches, in which RANS is applied near the walls while LES is employed in the core flow region, thereby leveraging the computational efficiency of URANS for unsteady flows. Efforts must continue to extend the applicability of LES to complex, industrially relevant systems while maintaining reasonable computational cost. At the same time, improvements in the accuracy of existing turbulence modeling approaches remain necessary.

3

Literature Review

The advancements in the literature will be discussed, providing an overview of the current state of knowledge in the field. The objective is to describe what has already been done and how the literature on the topic has evolved, thereby establishing the basis for the research and, more specifically, the research gap.

3.1. Development of Kerosene Combustion in Aviation

Human flight requires effective propulsion to overcome gravitational forces. The internal combustion engine enabled heavier-than-air aircraft in the early 20th century. Early aviation engines adapted automotive designs, but increasing performance demands led to purpose-built engines and specialized fuels [34].

3.1.1. Advancements in Aviation Fuel

A major milestone in the development of aircraft combustion was the invention of the turbojet engine around the time of World War II. This innovation imposed new requirements on aviation fuels, initiating a jet fuel development cycle [35]. The table provided outlines the major milestones and developments in kerosene-based jet fuels. Advancements were made in terms of volatility (the tendency of fuel to vaporize, which can cause vapor lock and engine malfunction at altitude), lubricity (the ability of fuel to lubricate moving parts such as metering pumps to prevent wear), vapor pressure (the pressure exerted by fuel vapors, which can lead to boil-off losses at high altitudes), flash point (the minimum temperature at which fuel produces ignitable vapors, essential for shipboard and passenger safety), freeze point (the temperature at which fuel solidifies, limiting usability in high-altitude or cold-weather operations), and thermal stability (the resistance of fuel to degradation at high temperatures).

Table 3.1: Evolution of Kerosene [35]

Fuel	Year	Deployment	Key Improvement
Avgas	1939	Standard for piston aircraft; used during early jet development	Baseline fuel; unsuitable for jets due to volatility, poor lubricity, and contamination
JP-1	1944	First dedicated turbine fuel (US Army Air Corps)	Introduced kerosene range for better energy density and cleaner combustion

Continued on next page

Fuel	Year	Deployment	Key Improvement
JP-2 / JP-3	1945–47	Experimental fuels for improved supply flexibility	Increased availability; JP-3 abandoned due to high vapor pressure and boil-off
JP-4	1951	USAF primary operational fuel	Improved availability and reduced cost while managing volatility
JP-5	1950s	US Navy carrier operations	High flashpoint enhanced shipboard safety
Jet A / A-1	1960s	Commercial aviation standard	Kerosene-based fuel reduced volatility, improving passenger safety
JP-TS / JP-6	1950s–60s	High-performance aircraft (U-2, XB-70)	Enabled operation at elevated temperatures (up to 218°C)
JP-7	1960s	SR-71 (Mach 3+)	Exceptional thermal stability
JP-8	1970s–95	Standardized military fuel	Safer kerosene base with additives reduced volatility
JP-8 +100	1990s	Advanced military aircraft systems	Increased heat sink capacity, providing improved cooling

Recent advancements in kerosene-based fuels have primarily been targeted at military applications. The standard jet fuel used in commercial aviation today is Jet A/A-1, as it is optimized for passenger safety and operational reliability. In recent years, the development of carbon-based fuels has shifted toward Sustainable Aviation Fuel (SAF). The drive toward sustainable aviation has been the main motivation for continued SAF development efforts. Table 3.2 outlines several of the most recent major developments in SAF technology.

Table 3.2: Evolution of SAF (Sustainable Aviation Fuel) [36]

Fuel	Year	Feedstock	Considerations
FT-SPK	2009	Wood waste or household trash	Can be made from abundant waste materials; however, production facilities are expensive to build and operate
HEFA	2011	Used cooking oil and animal fats	Most mature and widely used pathway; however, limited feedstock availability constrains global scaling
SIP	2014	Fermented sugars	Provides high energy content; however, currently limited to a 10% blend with conventional jet fuel
FT-SPK/A	2015	Wood waste or household trash	Improved compatibility with older engines and seals; however, the production process is complex
ATJ	2016	Plant-derived alcohols	Leverages existing alcohol supply chains; however, conversion to jet fuel adds cost and complexity
ATJ-ethanol	2018	Corn or sugar ethanol	Expands potential fuel supply significantly; however, sustainability concerns exist regarding food crop usage
HH-SPK	2020	Algae	Very high biomass productivity without requiring arable land; however, harvesting and processing remain expensive
Solar Fuel	Emerging	Sunlight, water, and CO_2	Direct solar-driven process; however, still in early research and difficult to scale

Although the development of SAF is a noteworthy effort, the current state of this technology is not yet sufficient for large-scale production and operation.

3.1.2. Advancements in Injector Designs for Reduced Emissions

The invention of the turbojet engine not only initiated the development cycle of aviation fuels. The fuel injector itself has undergone major improvements over the years and remains an active field of research. Specialized strategies for combustor design can be found for a variety of applications and objectives. The focus here is to outline some of the main concepts of modern low-emissions technologies for aero gas turbine engines.

The first concept to discuss is the Double Annular Combustor (DAC). In this configuration, annular staging is applied to control the stoichiometry and therefore the temperature. In Figure 3.1a, such a concept is illustrated. Two radial regions can be distinguished: the “P” zone, referring to the pilot, and the “M” zone, indicating the main combustion zone, both equipped with dedicated injectors. At low power settings, only the pilot combustion zone is active (located at the outer circumference of the combustor), while the main zone is not supplied with fuel. This increases the equivalence ratio, thereby mitigating the risk of blow-off instability. At higher power settings, the main zone is supplied with fuel, providing the required power while operating at a lower equivalence ratio compared to a conventional combustor. Multiple radial stages can be employed for even more precise control. A similar concept is the Axial Staged Combustor (ASC) (see Figure 3.1b). In this configuration, the main stage is placed downstream of the pilot stage, improving combustion stability and reducing the risk of local quenching caused by unfuelled airflow in the DAC concept. In addition, hot gases from the pilot provide a continuous source of heat and ignition for the main stage. As a result, the pilot exhaust enhances main-stage combustion efficiency and stability, enabling low CO and UHC emissions. However, this arrangement introduces challenges related to casing structural integrity. Furthermore, axial staged combustors require a longer axial length compared to conventional combustors to accommodate the main stage, which poses challenges for aircraft integration.

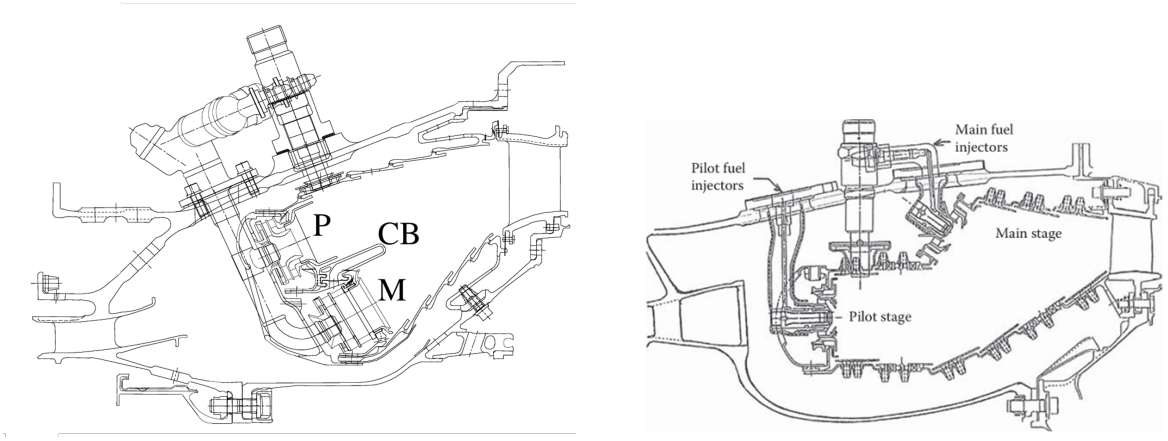

(a) DAC **(b)** ASC

Figure 3.1: Layouts of Dual Annular Combustor (DAC) and Axially Staged Combustor (ASC) [37, 28]

The TAPS (Twin Annular Premixed Swirler) concept can be regarded as an advancement of the DAC configuration. However, it integrates the pilot and main stages into a single injector while utilizing partially premixed combustion technology. The pilot stage is located at the center and provides a small, stable flame for ignition and idle operation. The pilot fuel interacts with axial air streams to create the Pilot Recirculation Zone (PRZ). The main stage surrounds the pilot stage and is activated during high-power operation. Fuel is injected into a cavity where it interacts with a high-velocity swirling air stream, creating the Center Recirculation Zone (CRZ). This configuration allows (partial) premixing of fuel and air prior to combustion, helping to maintain a more uniform flame temperature and thereby reducing emissions. The Local Recirculation Zone (LRZ) transfers heat and reactive radicals from the pilot stage to the main stage. This energy transfer from the pilot enables stable combustion in the main stage, even under very lean operating conditions. Another related concept is Lean Direct Injection (LDI), which also employs radial staging within the injector along with rapid mixing mechanisms considering the design shown in Figure 3.2b. The LDI concept injects fuel directly into the combustor and rapidly mixes it with a large fraction of air. Whereas TAPS relies on intense swirling for mixing, LDI utilizes wide spray angles and rapid evaporation within dedicated pilot and main-stage flow paths.

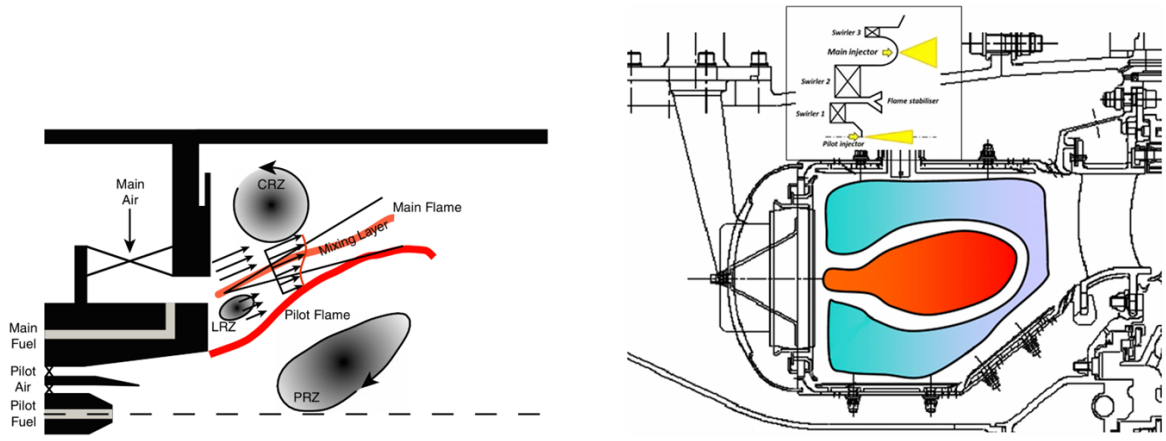

(a) TAPS **(b)** LDI

Figure 3.2: Layouts of Twin Annular Premixed Swirler (TAPS) and Lean Direct Injection (LDI) combustors [38, 39]

3.2. The Challenge of Transitioning from Kerosene to Hydrogen

Differences in fuel properties are fundamental to understanding the challenges associated with H_2 combustion compared to kerosene combustion. The most important fuel property differences are listed in Table 3.3.

The lower heating value (LHV) of H_2 is considerably higher than that of kerosene. Consequently, H_2 contains more energy per unit mass. However, H_2 has a very low density, resulting in a significantly lower volumetric energy density compared to kerosene. In addition, the boiling point of H_2 is far below ambient conditions. The high weight to energy ratio of hydrogen makes it an attractive energy carrier for aviation applications. However, its low volumetric energy density and extremely low boiling point introduce significant challenges for onboard storage. In particular, achieving sufficient energy capacity requires large storage volumes, especially when hydrogen is not stored in liquid form. Even when cryogenic liquid hydrogen is used, storage system integration remains complex due to insulation requirements, thermal management, and volumetric constraints [40]. Consequently, the integration of hydrogen storage tanks into existing aircraft architectures represents a major engineering challenge, motivating several ongoing research and development initiatives such as the Clean Aviation H2ELIOS project [41].

Another important characteristic of H_2 fuel is its increased flame speed. Although flame speed depends on temperature and equivalence ratio, H_2 exhibits a higher flame speed than kerosene across the entire equivalence ratio range [42, 43]. The risk of flashback and upstream flame propagation in aeronautical combustors increases with higher flame speeds, as the flame can propagate upstream more rapidly against the incoming flow, potentially reaching and damaging the fuel injection system, thereby requiring higher local flow velocities to prevent flashback.

The adiabatic flame temperature of H_2 is significantly higher than that of kerosene, which may further increase NOx formation. The adiabatic flame temperature represents the maximum theoretical flame temperature that can be achieved if all chemical energy released during combustion is converted into thermal energy without losses. In practical combustion systems, however, heat losses occur through radiation and convection, preventing the flame from reaching this theoretical maximum temperature. The equivalence ratio strongly influences flame chemistry and temperature. The highest flame temperatures are typically observed near stoichiometric conditions. At very high temperatures, dissociation of combustion products becomes significant, which absorbs energy and thereby reduces the flame temperature [28].

H_2 also possesses a considerably higher autoignition temperature than many hydrocarbon fuels, requiring more intense heating for spontaneous ignition in the absence of an ignition source. However, the required ignition energy is relatively low, meaning that even weak ignition sources can ignite H_2-air mixtures. The flammability limits of H_2 are also substantially wider than those of kerosene. H_2 can burn over a range of approximately 4–75% by volume in air (ambient conditions), whereas kerosene combustion occurs over a much narrower range of approximately 0.6–5% by volume. The wider flammability range of hydrogen must be considered in the design of H_2-based aviation systems to ensure safe operation, as it increases the likelihood of ignition over a broader range of fuel–air mixtures.

Another notable characteristic of pure H_2 flames is their low visible luminosity, as hydrocarbon flames are typically visible due to soot radiation. This might necessitate safety measures for the detection of H_2 flames, particularly in maintenance and research facilities.

The next major distinction between kerosene and hydrogen combustion is that, in H_2 flames, mass diffusion dominates thermal diffusion, whereas in kerosene flames the two diffusion processes are more comparable in magnitude. This is reflected in the Lewis number, which serves as an indicator of the relative rates of heat and mass diffusion. The Lewis number difference contributes to distinct combustion instability dynamics [44]. These instabilities must be carefully considered in H_2 combustion systems to ensure safe, reliable, and stable operation across the full range of operating conditions.

Finally, the primary combustion product of H_2 is H_2O, whereas kerosene combustion produces well-known carbon-containing emissions. This property underpins the feasibility of carbon-free aviation and thus serves as a key driver for ongoing advancements and research in H_2-powered propulsion and power generation systems.

Table 3.3: Comparison of H_2 and kerosene fuel properties [45, 46, 47]

Property	Hydrogen	Kerosene
Lower Heating Value (MJ/kg)	~120	~43
Volumetric Energy Density (MJ/L)	~8.5 (LH_2)	~34.7
Density (kg/m^3)	~70 (LH_2)	~800
Boiling Point (K)	20.28	423–573
Flame Speed	Very high	Moderate
Autoignition Temperature (K)	~858	~483
Adiabatic Flame Temperature (K)	~2400	~2100
Ignition Energy	Very low	Higher
Flammability Limits (vol%)	4–75	0.6–5
Flame Visibility	Invisible	Visible (luminous)
Lewis Number (-)	~0.3	~1–2
Combustion Products	H_2O (NO_x in air)	CO_2, H_2O, NO_x, CO, soot, UHC

3.3. Experimental Research of Multi-Fuel Systems

Experiments on H_2-kerosene blending began over forty years ago in the 1980s, demonstrating the feasibility of hybrid kerosene–H_2 fuels [48]. The motivation for these early studies originated from the desire to reduce emissions and to explore future scenarios in which H_2 could be produced sustainably using nuclear or solar energy. A modified gas turbine burner equipped with an air-blast atomizer was used. This atomizer included a thin annular slit through which gaseous H_2 was injected. It took until the 2000s for new experimental studies in this field to re-emerge. Stricter environmental regulations for aviation triggered renewed interest, particularly concerning CO and NOx emissions during idle and taxiing conditions at airports. Both [49] and [50] addressed these challenges. In contrast to the laboratory-scale burners of the 1980s, these studies employed industrial aeronautical fuel injectors. The latter study investigated idle engine conditions, corresponding to temperatures of 500K and a pressure of 3 bar. As the focus shifted toward ultra-low-emission combustion concepts, researchers began investigating the Lean Premixed Prevaporised (LPP) concept for blended H_2-kerosene fuel [51] (considering only moderate H_2 enrichment levels of up to 10% by mass). Further efforts to reduce soot and NOx emissions led to the development of a novel burner concept [52]. This burner primarily used H_2 to stabilise the flame while still relying on kerosene as the main fuel, reflecting the current limitations of H_2 storage. The LEAF (Lean Azimuthal Flame) combustor was introduced as a hexagonal chamber in which air jets are injected at an angle from the top, generating a swirling flow field. Kerosene is injected from the bottom into this swirling flow, while H_2 is used to stabilize the flame in a fixed position. More recent studies have focused on fuel-agnostic engine development, enabling operation on various mixtures of kerosene and H_2 [53]. These experiments were conducted under preheated air conditions with temperatures (T_{air}) up to 673 K. Moreover, [54] performed experimental studies on the HOPE combustor configuration considered in the subsequent chapters of this work. The corresponding experimental findings are discussed alongside the numerical results in Chapter 7, facilitating direct comparison and further insight.

Table 3.4: Experimental conditions and combustor configurations of key kerosene-H_2 blending studies

Reference	P [bar]	T_{air} [K]	Power	ϕ	Combustor Configuration
Hiroyasu (1980) [48]	1.0	Ambient	Constant	Varied	Air-blast spray + annular H_2 slit
Juste (2006) [49]	–	–	Varied	Varied	Industrial aero-injector; non-premixed H_2
Frenillot (2009)[51]	1.0	473	13.3 kW	0.3–1.0	Lean Premixed Prevaporized (LPP)
Burguburu (2011)[50]	3.0	500	86 kW	0.35–0.58	Industrial aero-injector
Miniero (2023) [52]	1.0	Ambient	15–25 kW	0.77–0.83	Lean Azimuthal Flame (LEAF) hexagonal
Singh (2025) [53]	1.0	473–673	23–37 kW	0.14–0.7	Low-swirl burner; H_2 jet-in-crossflow

3.3.1. Hydrogen Blending Effect on Flame Topology and Stability

In the previous section, the most significant experimental studies were presented and discussed. In this section, the same studies will be analysed with a focus on flame topology and stability. The chronological order will be followed, starting with the first experiment [48].

The influence of multi-fuel operation on flame stability is a key finding of this work, as the authors report that the lean blow-off (LBO) limit shifts significantly towards leaner conditions with the addition of H_2. When the H_2 fraction (R_h), defined as the ratio of the combustion heat released by H_2 to the total heat release, reaches 10%, the stabilisation effect becomes sufficiently strong that the LBO limit is effectively shifted beyond the typical operating range. In terms of flame structure, the authors classify hybrid combustion into three distinct regimes based on the value of R_h. In the first regime ($R_h < 10\%$), the flame appearance remains similar to that of a pure kerosene flame, characterised by strong yellow luminosity. In the second regime ($10\% < R_h < 50\%$), a transition occurs in which the flame color changes from bright yellow to yellow–blue as the kerosene fraction decreases. Finally, for $R_h > 50\%$, the flame behaviour approaches that of a pure H_2 flame, appearing violet or transparent purple.

In the experiments reported by [49], it is shown that the addition of H_2 significantly lowers the lean blow-off (LBO) limit in an actual aeronautical fuel injector. This extension of the stable combustion envelope enables ultra-lean operating regimes that were previously not attainable with pure kerosene, thereby increasing the operational margin for engine operation at lower global equivalence ratios.

In the next study [51], four distinct flame topologies were identified based on the equivalence ratio and H_2 share (see figure 3.3b):

- Anchored & Stable (AS): The flame is attached to the burner exit.
- Lifted & Stable (LS): The reaction zone moves away from the burner but remains steady.
- Lifted & Unstable (LU): The flame becomes visually unstable with low-frequency pressure fluctuations.
- Lifted & Very Unstable (VU): Occurring near the lean limit, the flame periodically nears complete extinction, accompanied by strong pressure oscillations.

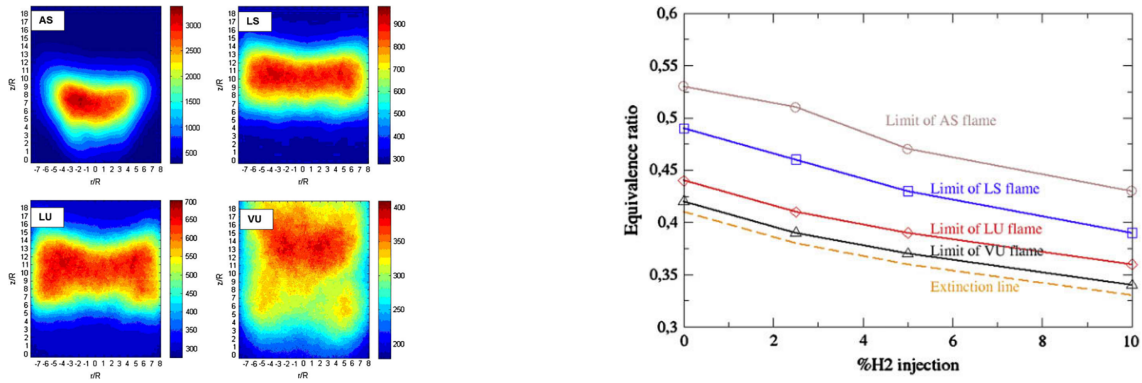

(a) Observed flame structures by CH imaging

(b) Stability limits of the flames by H_2 dilution

Figure 3.3: Observed flames with variation of H_2 dilution [51]

The study revealed that H_2 addition acts as a strong stabilizing agent, shifting the stability limits of flame structures towards leaner equivalence ratios. For instance, a 10% H_2 enrichment allowed the flame to remain anchored and stable at equivalence ratios at which a pure kerosene flame would have already been extinguished.

In [50], experiments were conducted under engine idle pressure and temperature conditions, where OH chemiluminescence was used to identify the reaction zones. The results show that H_2 enrichment enhances combustion intensity, particularly in the region near the injector exit. This enrichment effectively reduces the mean flame length compared to pure kerosene, resulting in a more compact reaction zone as the H_2 energy contribution increases. Furthermore, it is confirmed that H_2 addition extends the lean blow-off (LBO) limit.

A major challenge in modern aero-engine design is maintaining flame stability at low ratios of atomization air to kerosene mass flow, as encountered in airblast atomizers, since these conditions reduce the pressure drop across the fuel nozzle. However, under such low atomization-air-to-fuel conditions, pure kerosene flames tend to become unstable. In [52], it was shown that the addition of a small fraction of H_2 acts as a flame stabilising agent. By injecting H_2, the authors were able to maintain a stable flame structure under low ALR conditions where kerosene alone would have failed. This effectively extends the stable operating window towards more engine-relevant regimes.

Consider again [53], which investigates combustion under elevated inlet air temperatures. It was found that H_2 addition extends the lean blow-off (LBO) limit across all inlet air temperatures, although the effect is not linear. For H_2 contents up to 30%, the stabilisation effect remains relatively consistent across different T_{air} conditions. The authors attribute this to limited H_2 radial jet penetration and the continued dominance of Jet-A1 in the combustion process [53]. Once H_2 exceeds 30%, the higher reaction rates and diffusivity of the gaseous fuel lead to a significant reduction in the LBO equivalence ratio. Interestingly, the study shows that a 90% H_2 blend can operate at leaner conditions than pure H_2. This is attributed to residual Jet-A1 modifying the local mixture distribution and providing a stabilising effect that pure gaseous fuel does not exhibit. The flame topology was characterised using high-speed OH^* chemiluminescence imaging, with the lift-off height (LOH) defined as the axial position where 5% of the total integrated intensity is detected. While higher temperatures increase flame speed and slightly reduce LoH across all fuel blends, H_2 concentration is identified as the primary driver of flame shape changes. Up to 15% H_2, the reduction in LoH is minimal, as H_2 jets do not yet significantly penetrate the crossflow, resulting in a flame structure similar to pure Jet-A1 operation. Beyond 30% H_2, increased radial penetration leads to H_2 accumulation near the nozzle walls, shifting the reaction zone closer to the burner exit and producing a more compact, attached flame structure. This movement towards the nozzle indicates that, while H_2 improves stability, it also brings the system closer to flashback limits. However, axial air injection was shown to maintain a safe operating margin even at 100% H_2. This behaviour of H_2 blending is illustrated in Figure 3.4.

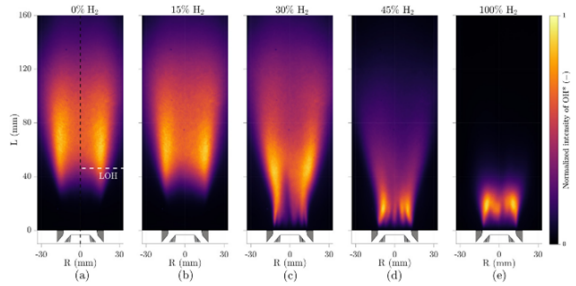

Figure 3.4: Time-averaged OH∗ chemiluminescence images of flame for different H_2 and Jet-A1 fuel splits at air preheating temperature of Tair = 473 K [53]

3.3.2. Hydrogen-Blending Effect on Emissions

Now that the flame topology and stability characteristics have been clarified, a closer examination of the emissions behaviour is presented. The same structure is maintained, following the chronological order and starting with the first experiment [48]. Throughout this study, the total combustion heat release was kept constant. In the first regime (R_h < 10%), the changes in soot and NOx emissions are relatively limited, although a slight increase in NOx emissions was observed. A significant reduction in emissions occurs during the second regime (10% < R_h < 50%). While NOx emissions begin to decrease, the reduction in soot concentration within the exhaust gases is particularly pronounced. In the third regime (R_h > 50%), where the flame behaviour approaches that of pure H_2 combustion, NOx emissions show only a minor further decrease. In contrast, soot emissions continue to decrease steadily due to the substantial replacement of carbon-based fuel with H_2. The overall reduction in NOx emissions throughout the study is primarily attributed to the leaner combustion conditions enabled by H_2 addition while maintaining constant heat release.

The primary motivation for the next study was the reduction of pollutant emissions during the Landing and Take-Off (LTO) cycle [49], particularly during low-power operating conditions such as taxiing and idling, where carbon monoxide (CO) emissions are typically high. The results confirmed that H_2 addition is a highly effective strategy for emission reduction under these conditions. The study found that even a modest H_2 energy contribution of

1.4% resulted in a 50% reduction in CO emissions. This reduction is attributed to the replacement of carbon-based fuel by H_2, as well as the increased concentration of hydroxyl radicals (OH), which promote the complete oxidation of CO into CO_2. However, unlike the clear trends observed for CO and soot reduction, the influence on NOx emissions remained less certain. The study reported that, for a constant kerosene mass flow rate, NOx emissions could increase due to higher local flame temperatures. Nevertheless, it was concluded that the ability to operate at leaner equivalence ratios, enabled by the improved flame stability, could ultimately result in lower NOx emissions.

Regarding the pollutant emissions reported in [51], the results confirmed that CO emissions decrease significantly with increasing H_2 share at constant power. However, the behaviour of NO_x emissions was found to be governed primarily by the equivalence ratio, largely independent of H_2 enrichment or combustion power. Therefore, the main benefit of H_2 for NO_x reduction in LPP systems is not necessarily associated with direct chemical effects, but rather with its ability to sustain stable combustion at ultra-lean equivalence ratios, where NO_x formation is inherently lower.

Consider again the study conducted under engine idle pressure and temperature conditions [50]. The experiments demonstrated that H_2 enrichment is highly effective in reducing CO emissions, which decreased significantly even for relatively small H_2 energy contributions. This effect is attributed to the increased availability of OH radicals provided by H_2 combustion, which enhances the oxidation of CO into CO_2. However, the study also identified an environmental trade-off regarding NO_x emissions. While CO emissions were reduced, the H_2 injection mode resulted in a notable increase in NO_x, with differences observed between combustor configurations. The authors concluded that the thermal NO_x mechanism was the dominant contributor. The anchored pilot flames present in the investigated combustor configuration created localised high-temperature regions near the injector, thereby promoting thermal NO_x formation.

Recall the innovative combustor design presented in [52]. The LEAF concept achieved near-zero soot emissions at the exhaust. High-speed imaging revealed that, although soot was formed within the primary reaction zone at low ALR conditions, the long residence times and high mixing rates associated with the azimuthal flow ensured that these particles were fully oxidised before exiting the combustor. The simultaneously reduced NO and CO emissions demonstrated that a novel swirling-flow combustor with H_2 injection can enable a clean and efficient combustion regime for liquid fuels.

Consider again the study by [53], in which inlet air temperatures (T_{air}) up to 673 K were investigated. Regarding pollutant emissions, the study identifies a complex and non-linear relationship between H_2 addition and inlet air temperature. For H_2 shares up to 45%, an increase in T_{air} is observed to reduce NO_x emissions. This is attributed to accelerated evaporation of the kerosene spray and improved premixing at higher temperatures, which reduces the formation of local hot spots. However, beyond the 45% threshold, the high adiabatic flame speed and temperature associated with H_2 become dominant, leading to a sharp increase in NO_x emissions. In contrast, CO emissions exhibit a consistent and rapid decline with increasing H_2 content; even a modest 15% H_2 fuel fraction was found to significantly reduce CO emissions at lower power settings.

3.3.3. Summary of Experimental Findings

The results from the experimental studies are summarised in Table 3.5. The HSD (H_2 share definition) is predominantly defined based on power, although mass-based definitions are also used. There is no clear consensus regarding NO_x emissions. On the one hand, the higher adiabatic flame temperature of H_2 promotes thermal NO_x formation. On the other hand, H_2 extends the LBO limit, thereby enabling leaner combustion conditions and thus suppressing thermal NO_x formation. It can therefore be concluded that NO_x emissions are highly dependent on the combustion configuration and operating strategy. CO emissions are significantly reduced, even at small H_2 blending ratios, due to the presence of OH radicals generated during H_2 combustion, which promote the conversion of CO to CO_2. CO_2 emissions are reduced as less carbon is introduced into the fuel mixture. Similar trends can be expected for soot and UHC emissions, although these have not been extensively investigated in the reviewed literature. In all cases, the LBO limit is extended, enabling operation at leaner equivalence ratios. This shift towards leaner operation affects not only flame extinction behaviour but also flame topology in general.

Table 3.5: Emissions and Stability Characteristics of Experimental H_2-Kerosene Blending (× = not mentioned, − = decrease, + = increase)

Reference	Year	Author	HSD	Constant	NOx	CO	CO_2	Soot	UHC	LBO
[48]	1980	Hiroyasu et al.	p	Power, Airflow	-	−	−	x	×	+
[49]	2006	Juste	m	Airflow	×	−	−	×	×	+
[51]	2009	Frenillot et al.	m	Power	−	−	−	×	×	+
[50]	2011	Burguburu et al.	p	Power	+	−	−	×	×	+
[52]	2023	Miniero et al.	p	Power	−	×	−	−	×	+
[53]	2025	Singh et al.	p	Power, Airflow	−	−	−	×	×	+

3.4. Computational Research of Multi-Fuel Systems

The simulations performed in the multi-fuel context are discussed in the present section, focusing on the most relevant studies involving gaseous H_2 and liquid kerosene. While a large number of studies have been conducted on homogeneous gaseous fuel systems involving H_2/CH_4 blending [55], these are not the primary focus here, as the emphasis remains on kerosene–H_2 combustion systems and therefore liquid-gaseous fuels interaction. In 2013, [56] numerically modified an oil-burning gas turbine combustor to operate with syngas and liquid kerosene. The objective was to compare combustion flow fields and emissions between the two fuels using a newly developed dual-fuel nozzle. In the same period, Zheng et al. [57] investigated three different dual-fuel nozzle configurations. Later, in 2020, [58] performed a numerical analysis of n-decane (a kerosene surrogate)/H_2 blends in an academic combustion chamber. This represents the first premixed case among the reviewed studies. Subsequently, [59] conducted a multi-fuel simulation for marine power plants on Floating Production, Storage, and Offloading vessels, simultaneously burning diesel and methane. In 2022, [60] focused on implementing Colourless Distributed Combustion (CDC) for H_2-enriched kerosene in industrial gas turbines. The main objective was to mitigate the high flame temperatures and instabilities associated with hydrogen addition. In 2024, [61] investigated a mini-jet engine as a test case for CDC implementation in aviation gas turbines, aiming to achieve CDC conditions with H_2/kerosene blends. In the same year, [62] shifted the focus to the dynamic switching process between diesel and natural gas in industrial combustors. Driven by energy security and fuel flexibility requirements for offshore platforms, the study showed that a "fast-opening" strategy outperforms alternative fuel supply methods in maintaining flame stability during transitions. Also in 2024, [63] conducted a theoretical two-dimensional numerical study on n-dodecane/H_2 premixed flames. This work was motivated by the limited literature on fundamental stabilization mechanisms, including Lewis number effects, in dual-fuel systems relevant to large-scale aero-engines. A previous study within the HOPE project, conducted by [64, 65], utilized CFD-based scouting to support the design of earlier combustor configurations. The latter work provided a deeper analysis of the selected combustor design, involving more detailed analysis of the kerosene-H_2 interaction. A start has been made towards detailed local flow interaction analysis, making use of the availability of high-fidelity LES data throughout the flow-field to resolve internal flame structures. The work provides descriptive post-processing methods for multi-fuel CFD simulations, highlighting the interaction between local equivalence ratio and the spatial distribution of H_2 and kerosene combustion zones. The analysis shows that, in the considered combustion system:

- Multi-fuel flames exhibit strong spatial segregation, where local mixture composition governs where each fuel burns.
- Flame structure and stabilization are primarily controlled by local mixing processes, shear layers, and recirculation zones rather than the global fuel split alone.
- Heat release is highly localized, with hydrogen and kerosene burning in distinct regions depending on the local equivalence ratio.
- Flame transitions with increasing hydrogen content arise from changes in local flowfield conditions, leading to the merging or separation of reaction zones.

Another recent multi-fuel study is that of [66] concerning an ammonia/H_2 gaseous combustor, however, introducing novel developments to the multi-fuel thickened flame model, particular through the use of an advanced flame sensor. An overview of the reviewed multi-fuel CFD studies is provided in Table 3.6.

Table 3.6: Overview of Multi-Fuel CFD Simulation Parameters

Reference	Year	Fuels (F1/F2)	Phases	Mixing	Application
Pan et al.[56]	2013	Kerosene (surrogate) / Syngas	l / g	non	Gas Turbine
Zheng et al. [57]	2013	Kerosene (surrogate) / Syngas	l / g	non	Gas Turbine
Kozlov et al. [58]	2020	Kerosene (surrogate) / H_2	l / g	p	Simplified
Serbin et al. [59]	2021	Diesel / Methane	l / g	p	Marine GT
Ilbas et al. [60]	2022	Kerosene (surrogate) / H_2	l / g	non	Gas Turbine
Alabas et al. [61]	2024	Kerosene (surrogate) / H_2	l / g	non	Mini Jet
Vance et al.[63]	2024	Kerosene (surrogate) / H_2	g / g	pre	Simplified
Hu et al. [62]	2024	Diesel / Natural Gas	l / g	non	Gas Turbine
Palanti et al.[64, 65]	2024/2025	Kerosene (surrogate) / H_2	l / g	p	Aeroengine
Vargas et al.[66]	2025	Ammonia / H_2	g / g	p	Gas Turbine

Most of the multi-fuel simulation studies reviewed in this work employ RANS models due to their computational efficiency. In addition, a DNS (Direct Numerical Simulation) approach was used by [63], as the study was performed on a simplified academic domain. The first identified LES-based study is [62], where LES was required to capture transient flow characteristics in a liquid–gaseous interaction system, although without hydrogen. A recent LES-based study is [66], which includes hydrogen in combination with gaseous ammonia.

The remainder of this chapter discusses the modeling approaches employed in the reviewed studies. The key elements of (multi-fuel) combustion modeling are addressed individually. The first element is the turbulence closure method. The second element addresses turbulence–combustion interaction modeling. The third subject addresses the reaction mechanisms employed in the multi-fuel simulations. The following subject is the treatment of the pollutants within the simulations. Finally, for simulations involving liquid fuels, the discrete phase models are described. The section concludes with a discussion of the validation approaches used in the reviewed simulations.

3.4.1. Turbulence Model

The early RANS-based studies employed the Realizable k–ε model ([56], [57], [58]). This model is widely regarded as a robust formulation that provides improved numerical stability and higher prediction accuracy compared to the standard k–ε model, particularly for jet flows and mixing-dominated regimes. The Standard k–ε model was also used in [60] and [61], where it served as a reference turbulence closure. The k–ω SST (Shear Stress Transport) model was employed by [64]. This two-equation model is frequently selected due to its improved treatment of turbulent shear stress transport and its generally reliable performance in swirling flow configurations. For LES approaches, different subgrid-scale (SGS) models are required. The WALE (Wall-Adapting Local Eddy-viscosity) model was used by [62, 65] for subgrid-scale closure. WALE is suitable for a wide range of Reynolds numbers at comparable grid resolutions and improves near-wall accuracy compared to classical Smagorinsky-type models. In addition, the LES Sigma model was employed by [66] for ammonia–H_2 flames, due to its reported robustness in swirling flow configurations.

3.4.2. Turbulence Chemistry Interaction

The following section outlines turbulence–chemistry interaction (TCI) modeling, the methods used to close reaction source terms in turbulent reactive flows. Early studies primarily employed statistical PDF-based approaches, such as the Flamelet Generated Manifold (FGM) framework. Both [56] and [57] utilised PDF-based methods due to their computational efficiency for non-premixed combustion. Later, the Eddy Dissipation Concept (EDC) was employed by [59], enabling the including detailed reduced chemical mechanisms directly within turbulent flow simulations. The same approach was also adopted by [64], where EDC was selected due to its robustness in handling simultaneous combustion of multiple fuel streams with varying compositions. EDC is also well-suited for implementation in both RANS and LES frameworks, as it is based on species transport and local mixing time-scale assumptions. For this reason, [62] also adopted the EDC model in the corresponding study. The Thickened Flame Model (TFM) for kerosene–H_2 combustion is investigated in [65], representing a further step toward CFD-based design, optimisation, and analysis in multi-fuel conditions, as it is considered a more advanced

modeling approach as the flame is directly resolved on the grid. Further development of the Multi-Fuel Thickened Flame LES (MF-TFLES) model was conducted by [66]. This framework employs passive scalar transport to dynamically adjust both the flame thickening factor and the flame sensor in regions with strongly mixed multi-fuel conditions, thereby improving flame resolution in blended regimes. For DNS, a Direct Arrhenius (laminar chemistry) approach is used, as reported in [63].

3.4.3. Reaction Mechanism

The reaction mechanism describes the chemical interactions and is therefore of fundamental importance, as it defines the reactions included in the simulation. Early studies did not explicitly report the employed reaction mechanisms ([56], [57]). Detailed chemical mechanisms are computationally expensive; therefore, reduced mechanisms are often introduced, as demonstrated by [58]. An alternative approach is the use of simplified reaction sets, as applied by [62], where five reactions were included for diesel combustion and two for methane. The DNS study of [63] also requires a chemical mechanism, as it must explicitly resolve the underlying reaction pathways. In that work, the selected mechanism was validated against experimental laminar flame speed data. In multi-fuel systems, it is essential that the mechanism accurately represents all fuel components. In this context, [64] identified a suitable mechanism (Z77 mechanism), which is a reduced scheme for kerosene that includes a methane base sub-mechanism and incorporates a detailed H_2 oxidation pathway, enabling accurate modeling of both fuel streams. Another important constraint is the range of operating conditions covered by the reaction mechanism, as validation and applicability are typically dependent on pressure and temperature ranges.

3.4.4. Pollutant Models

The species and major pollutants (CO, CO_2, and unburned hydrocarbons) can be directly obtained from the governing equations when they are included in the gas-phase reaction mechanism, typically by tracking the corresponding transported species and fuel depletion at the outlet. In contrast, NOx is commonly treated in post-processing because it is a trace species that has negligible influence on the flow, temperature, and overall combustion process, while its formation depends on already computed fields such as temperature, oxygen concentration, and residence time. Consequently, NOx is often evaluated in the post-processing using models such as the Zeldovich mechanism (see subsection 2.4.1), as employed in [67, 64, 59, 60, 61], whereas only a limited number of studies directly solve NOx within the governing reaction mechanism, as performed by [66]. Similar post-processing approaches are commonly employed for soot, as it involves the formation of solid particulate matter that is generally not represented within the gas-phase reaction mechanism [68].

3.4.5. Discrete Phase Models

In the early development of discrete phase models (DPM), the primary objective was to ensure that liquid fuel droplets evaporate and reach the relevant regions of the combustor. For example, [56] adopted a Lagrangian discrete phase model in which the liquid fuel is represented as discrete particles. In this framework, the particle motion equation is solved by integrating the forces acting on each individual droplet to predict its trajectory through the continuous air flow field. However, real fuel sprays do not consist of identical droplets, but rather exhibit a distribution of droplet sizes. This size spectrum was incorporated by [59], where droplets ranging from 5 to 75 μm (with an average diameter of 35 μm) were tracked, enabling a more realistic representation of evaporation behaviour across different droplet sizes. To model the statistical distribution of spray sizes, [61] employed the Rosin–Rammler distribution, which defines the probability of occurrence of droplets of a given diameter within the spray. In addition, [64] used Lefebvre's correlation to estimate the Sauter Mean Diameter (SMD), which serves as input to the Rosin–Rammler distribution.

3.4.6. Validation Methods and Overview of Multi-Fuel Simulations

The early studies by [57, 56] validated their numerical models by simulating various operating conditions and comparing the mean outlet temperature with experimental data. While this provides a general level of agreement suitable for preliminary industrial assessment, it does not account for flame structure or internal flow field characteristics. The validation approach used by [58] was based on outlet CO concentration, without spatial verification of the flame topology. Another commonly used approach is the comparison of axial temperature profiles with literature data, as reported by [60], although this does not constitute a direct experimental validation. Similarly, [61] relied on outlet temperature comparisons with literature values, without resolving detailed flame features. The CFD-based design study by [64] noted that no quantitative experimental data was available for the specific

configuration and therefore did not include a formal quantitative validation. In contrast, [65] performed a more advanced validation using RMS velocity profiles and OH* chemiluminescence imaging, enabling comparison of predicted and measured flame structures. Finally, [66] employed the most comprehensive validation strategy among the reviewed studies. This included an initial chemical kinetics assessment, followed by comparison of cold-flow velocity profiles with Laser Doppler Velocimetry (LDV) measurements, and a reactive-flow validation using OH* chemiluminescence and NO-PLIF imaging. This multi-stage approach provided detailed agreement in both flame structure and flow field characteristics.

Table 3.7 summarizes all considered studies together with their employed modeling approaches. Early studies predominantly relied on RANS models coupled with PDF-based chemistry interaction models to manage computational cost. Subsequently, research shifted towards species transport approaches using the Eddy Dissipation Concept (EDC), while still operating within the RANS framework. More recent studies employ LES and SBES methods, which offer improved accuracy by resolving large-scale unsteady flow structures and capturing the inherently non-linear nature of combustion processes. In general, reduced reaction mechanisms are adopted to limit computational cost while maintaining sufficient accuracy in the representation of chemical kinetics. Discrete phase models are applied whenever inhomogeneous gas–liquid interactions are considered, typically formulated within a Lagrangian framework.

Table 3.7: Overview of Multi-Fuel CFD Modeling Approaches and Sub-Models

Reference	CFD-method	Turbulence Model	Turbulence Chemistry Interaction	Reaction Mechanism	Discrete Phase
Pan et al.[56]	RANS (Steady)	Realizable k-ϵ	PDF	Not - specified	DPM (Lagrangian)
Zheng et al.[57]	RANS (Steady)	Realizable k-ϵ	PDF	Not - specified	–
Kozlov et al.[58]	RANS (Axisymmetric)	Realizable k-ϵ	Quasilaminar (QL)	Reduced n-decane (33 sp, 185 rxn)	–
Serbin et al.[59]	RANS (Steady)	RNG k-ϵ	EDC	6-step Diesel/Methane	DPM (Lagrangian)
Ilbas et al.[60]	RANS (Steady)	Standard k-ϵ	EDC	Not - specified	–
Alabas et al.[61]	RANS (Steady)	Standard k-ϵ	Non-premixed	Not - Specified	DPM (Lagrangian)
Vance et al.[63]	DNS-like (Laminar)	– (Laminar)	Direct Arrhenius	Lu-31 n-dodecane/H_2 (31 sp)	–
Hu et al.[62]	LES	WALE Sub-grid	EDC	Skeletal (5 rxn Diesel, 2 rxn CH_4)	DPM (Lagrangian)
Palanti et al.[64]	RANS (Steady)	k-ω SST	EDC-PaSR	Z77 Kerosene (30 sp, 77 rxn)	DPM (Lagrangian)
Palanti et al.[65]	SBES (Hybrid RANS/LES)	k-ω SST / WALE	TFM	Z79 Kerosene (30 sp, 79 rxn)	DPM (Lagrangian)
Vargas et al. [66]	LES	Sigma Sub-grid	MF-TFLES	ARC $NH_3H_2N_2$ (15 sp)	–

4

Research Proposal

The current state of the literature has been reviewed in the previous chapter. This state of knowledge will now be used to identify the research gap from which the research questions are formulated. Thereafter, the objective of the research will be stated.

4.1. Research Gap

The literature review discussed the significant advancements in the field of multi-fuel combustion, with emphasis on kerosene-H_2 fuel blending involving inhomogeneous combustion of gaseous H_2 and liquid kerosene. In general, the understanding of this H_2-kerosene interaction can be improved and expanded.

The physical structure and stability of H_2-kerosene flames have been explored, examining the effects of fuel blending on luminosity, lift-off height, and blow-off. However, research on this topic is limited in scope, with only a small number of dedicated studies available [51, 50, 30, 53, 65] actually concerning the physical flame structure. The mixing of the gaseous H_2 and the kerosene spray and its associated influence on the stability and structure can further be explored. The effect of H_2 blends on the spatial distribution of equivalence ratio, power generation, evaporation, premixing and species within the combustor is touched upon by [65], however, it can be much further explored. Furthermore, a dedicated study on flashback characteristics and prevention in kerosene-hydrogen blended flames is absent. Premixed H_2 flames are prone to flashback, in critical conditions it might be beneficial to provide more power from kerosene spray flames, however, a dedicated study is not present.

The emission characteristics of blended H_2-Kerosene flames have been examined in several studies and significant trends can be found as outlined in Table 3.5. The research showed that CO and CO_2 strongly decrease as carbon is withdrawn from the fuel. Further, OH promotes CO to CO_2 conversion and hence a moderate addition of H_2 results in a significant decrease of CO pollutants [50, 53]. The exact spatial distribution and interaction of this CO-OH phenomena is unknown and might provide tools to further minimize CO emissions. Most notably, the NOx emissions in H_2-kerosene flames showed to be dependent on specific design strategies as H_2 could lead to localized hotspots [50], promoting thermal NOx. The exact hotspot formation locations within the combustor and therefore thermal NOx formation and its influencing parameters could be further explored. Spatial and temporal descriptions of species and pollutants formation for kerosene-H_2 blended spray flames remain scarce. Utilizing local flow-field data to localize species formation spots and eventually leading to pollutant mitigation strategies could be further expanded upon.

Numerically, several RANS simulations have been performed in the kerosene–H_2 context to estimate emissions, and in some cases design changes have even been derived from these results (see Table 3.7). However, validation remains mostly restricted to global quantities such as outlet temperature or overall emissions, rather than detailed flame shapes. Consequently, sophisticated validation against experimentally observed flame structure in inhomogeneous H_2–kerosene combustion has only been carried out in a small number of studies [65, 66]. There

are therefore limited numerical efforts that explicitly describe flame topology itself. Furthermore, although LES has demonstrated strong predictive capability in turbulent combustion [69], its application to multi-fuel reacting flows in the kerosene-H_2 regime remains limited. Overall, the use of CFD for detailed multi-fuel combustion analysis remains underutilized, and validation against experimental flame shape data is still scarce [65, 66]. The thickened flame model (TFM) for multi-fuel combustion has been only sparsely tuned and validated and would benefit from further systematic investigation and development.

The use of LES/SBES-TFM models for multi-fuel reacting flows in the gaseous–spray combustion regime remains limited, despite their promising accuracy. Consequently, the potential of CFD, particularly its data-rich nature and flexibility, is not yet fully exploited in multi-fuel combustion applications. A more detailed analysis of local mixing characteristics and emissions could provide improved insight into H_2–kerosene flame structure, stabilization mechanisms, and pollutant formation pathways. Ultimately, this may enable improved flame stabilization mechanisms and/or more effective pollutant mitigation strategies.

The data flexibility of CFD can further be leveraged to explore additional operating regimes in terms of pressure and temperature. Regarding pressure effects, only a single experimental study [53] has addressed this aspect, while investigations of inlet temperature effects remain scarce. In particular, the individual and combined influence of inlet temperature, pressure, and power on flame characteristics and emissions in kerosene–H_2 blended flames has been partially explored. However, a comprehensive understanding is still lacking, especially under engine-relevant conditions involving elevated power, temperature, and pressure.

Despite significant progress in H_2–kerosene blended combustion research, important gaps remain regarding flame topology, local mixing behaviour, pollutant formation, and numerical modeling. In particular, the local interaction between gaseous H_2 and liquid kerosene sprays, including flame stabilization mechanisms, species evolution, and flame topology, remains insufficiently understood. Furthermore, experimentally validated LES/SBES-TFM studies and investigations under engine-relevant operating conditions are still limited, highlighting the need for further detailed experimental and numerical research.

4.2. Research Question

The interaction between multi-fuel H_2–kerosene flames remains an active field of research. A deeper understanding of this interaction regarding emissions and stability is fundamental to achieving the HOPE objectives. Current research shows a gap, and LES/SBES simulations remain underutilized for describing flame topology and mixing characteristics, despite their demonstrated accuracy. Unlike experimental measurements—which are typically limited in spatial and/or temporal resolution—CFD provides access to detailed information throughout the entire flow field. By leveraging the accuracy of LES/SBES and the data-rich nature of CFD, valuable insights into H_2–kerosene blended combustion can be retrieved. This thesis employs CFD-based LES/SBES simulations to investigate multi-fuel kerosene–H_2 combustion processes. The central research question of this thesis is:

How do different hydrogen–kerosene blend ratios affect the flame topology in the HOPE combustor under atmospheric conditions, and how does the current design perform under intended engine operating conditions?

The main question will be investigated utilizing numerical simulation. The first step in the research is to obtain accurate and representative simulations. In this research, LES/SBES and the TFM will be employed to utilize their accuracy in predicting flame behaviour and combustion characteristics. The model performance will be explored and applied to the full range of blend ratios, incorporating both pure hydrogen and pure kerosene as well as truly blended regimes. Hence, the following question will be answered:

To what extent is the LES/SBES approach, coupled with the TFM model, able to capture the flame shape for various kerosene–hydrogen blend ratios?

While the first part of the research assesses the accuracy of the CFD simulations, the second focuses on the use of these results to describe the flame topology. In this part, the data flexibility and availability of CFD simulations are intended to be used to describe the interaction of the kerosene-H_2 flames. Hence, the following question will be answered:

How can the structural features and flow properties of kerosene-hydrogen blended flames be described and

quantified for various blend ratios?

The ultimate aim of advancing knowledge on fuel blending is the development of practical aerospace systems. Therefore, actual engine operating conditions should be considered. Currently, experimental data is only available at the atmospheric conditions. Therefore, a scouting study will be performed to estimate the current performance of the HOPE-combustor, eventually giving advice for modification and further development of the combustor.

What is the performance of the current combustor under the intended operating conditions, and which modifications are recommended to improve the system?

4.3. Research Objective

The objectives of this thesis are derived from the research questions and are structured as follows. The first objective is to contribute to the development and validation of LES/SBES CFD simulation frameworks, with particular emphasis on the application of the TFM approach for modeling turbulence–combustion interaction in kerosene-H_2.

The second objective is to characterize flame topology and internal flow structures by exploiting the high-fidelity data and flexibility offered by LES/SBES simulations. To this end, novel post-processing variables and diagnostic methods will be developed to effectively identify, quantify, and visualize key features of flame topology of kerosene-H_2 flames.

The third objective is to assess system performance under engine-relevant operating conditions. While experimental facilities are often constrained in terms of achievable temperature, pressure, and power levels in test rigs, CFD enables exploration beyond these limits, allowing systematic investigation of operating conditions relevant to practical engine environments.

5

Modeling Multi-Fuel Combustion

This chapter introduces the modeling methodologies by breaking them down into three distinct areas. The first section details the turbulence modeling. The second section discusses turbulent combustion modeling and explains how multi-fuel handling is integrated. The final section establishes the framework for kerosene spray modeling.

5.1. Turbulence Modeling

The turbulence is solved using the Stress-Blended Eddy Simulation (SBES) model [70]. The method combines URANS and LES to overcome the inherent limitations of both approaches. In LES, turbulent structures are resolved. These structures are also referred to as eddies. This means that the simulation directly computes their time evolution from the governing equations. They are therefore not represented through (statistical) modeling. The smallest eddies that can be resolved depend on the grid resolution; flow structures smaller than this threshold are represented by subgrid-scale models. LES is well suited for free shear layer (a flow region characterized by a strong velocity gradient between adjacent fluid streams in the absence of solid boundaries) regions, because the dominant turbulent structures are relatively large and can therefore be explicitly resolved. The size of the eddies becomes smaller when approaching the wall, hence, even smaller grids are necessary. The grid should be extremely refined in the three spatial directions near the walls to accurately capture the fine eddies in this region; hence, the computational cost becomes in many cases unmanageable. On the other hand, URANS employs models to incorporate the full turbulence scale, making it suitable for near-wall applications as it does not rely on very fine grids to capture small turbulent structures in this region. However, it loses the ability to actually resolve (instead of modeling) the eddies, inherently reducing accuracy. Therefore, SBES utilizes LES in the free shear layer, benefiting from its accuracy in the region, while it adopts URANS near the walls to reduce computational costs. The SBES model switches between URANS and LES based on a shielding function f_{SBES}; the function becomes unity in regions of URANS deployment and zero in the LES zone. The SBES stress tensor is therefore determined as shown by Equation 5.1.

$$\tau_{ij}^{\mathrm{SBES}} = f_{\mathrm{SBES}}\, \tau_{ij}^{\mathrm{URANS}} + (1 - f_{\mathrm{SBES}})\, \tau_{ij}^{\mathrm{LES}} \tag{5.1}$$

There are alternatives to the SBES model, such as Delayed Detached Eddy Simulation (DDES) [71]. In DDES, the modeled/resolved scales use the same turbulence model, reducing the modeled turbulence away from the walls, allowing more turbulent structures to be resolved by the governing equations. However, the SBES simulation has been selected because the subgrid-scale-turbulence and URANS-turbulence are computed by two distinct models. Consequently, this framework enables the selection of distinct turbulence models for the RANS and LES domains, allowing each region to be treated with the most appropriate modeling approach in accordance with its anticipated flow characteristics.

The URANS turbulence model is the k-ω SST (Shear Stress Transport), as it has proven reliable for near wall

regions [72]. For the LES subgrid-scale turbulence modeling, the WALE model is utilized [73]. A feature of the WALE model is that the eddy viscosity naturally goes to zero near walls without requiring damping functions or empirical tuning. This can be advantageous in SBES frameworks, since accurate near-wall decay of the eddy viscosity could help to ensure a smooth RANS–LES transition. Moreover, its computational cost is comparable to that of the commonly used Smagorinsky subgrid-scale-turbulence model.

5.2. Multi-Fuel Combustion Modeling

As discussed in previous chapters, the SBES model is coupled with the Thickened Flame Model. The implementation approach and multi-fuel treatment follow the methodology presented in [65] and are further clarified in this section. First, additional variables required for multi-fuel combustion are introduced. Subsequently, the Thickened Flame Model (TFM) and its adaptation for multi-fuel combustion are described.

5.2.1. Additional Variables for Multi-Fuel Combustion

The SBES-TFM formulation for kerosene–H_2 combustion requires the definition of the local (mass-based) fuel-split parameter or hydrogen-fraction α and the local equivalence ratio ϕ. In contrast to their global counterparts, these quantities are defined throughout the entire flow field and therefore describe the local state of the system rather than only its overall behaviour. The global power-split parameter HPS_g, based on the relative fuel power contribution, is first introduced, followed by the hydrogen-fraction parameter α_g and the global equivalence ratio ϕ_g. The complete set of parameters to be defined is HPS_g, α_g, ϕ_g, α, and ϕ.

To characterize the fuel composition in dual-fuel operation, a parameter based on the ratio of energy carried by each fuel is introduced. Although various definitions are used in literature (see table 3.5), no standardized parameter has been established. The most widely adopted approach relies on the energy carried by each fuel, and accordingly, the global Hydrogen Power Share HPS_g is defined as shown in Equation 5.2:

$$\mathrm{HPS}_g = \frac{\dot{m}_{H_2}\mathrm{LHV}_{H_2}}{\dot{m}_{H_2}\mathrm{LHV}_{H_2} + \dot{m}_{\mathrm{kero}}\mathrm{LHV}_{\mathrm{kero}}} \tag{5.2}$$

Here, LHV is the lower heating value. The parameter is defined such that HPS_g=1.0 and HPS_g=0.0 correspond to pure hydrogen and pure kerosene operation, respectively. Alongside this global parameter, the global hydrogen mass based fraction α_g is defined as represented in Equation 5.3:

$$\alpha_g = \frac{\dot{m}_{H_2}}{\dot{m}_{H_2} + \dot{m}_{\mathrm{kero}}} \tag{5.3}$$

As the LHV of kerosene and hydrogen differ, the corresponding α will be lower for the same power setting (with exception of HPSg=0.0% and HPSg=100.0%), meaning that HPSg=0.5 corresponds to approximately α_g=0.26. To assess whether combustion occurs under rich or lean conditions, the global equivalence ratio ϕ_g is introduced in Equation 5.4:

$$\phi_g = \frac{\mathrm{AFR}st}{\mathrm{AFR}} \tag{5.4}$$

where AFR is the air mass flow to fuel mass flow ratio, and AFR_{st} accounts for the fuel-blend composition as shown in Equation 5.5:

$$\mathrm{AFR}st = \alpha_g \mathrm{AFR}st_{H_2} + (1-\alpha_g)\mathrm{AFR}st_{\mathrm{kero}} \tag{5.5}$$

Having introduced the global quantities, the focus is now shifted to the corresponding local quantities required for the SBES-TFM multi-fuel formulation. The local mass-based hydrogen fraction α is introduced first, followed by the local equivalence ratio ϕ.

Analogous to the Bilger mixture fraction [74], a local hydrogen mass fraction α is defined so that it is not affected by the reactive process but solely by mixing of elements. as the parameter is based on elemental rather than species mixing properties. The current parameters are specifically designed to operate with three distinct streams: air, hydrogen, and kerosene. In cases involving multiple streams, the method proposed by [75] must be considered. The method is used to identify the originating stream of each element.

The local α, as represented by Equation 5.6, is only valid in the unburnt mixture, as chemical reactions alter the

species composition. This formulation is simply the ratio of the mass fraction of hydrogen to the total fuel mass fraction (Y_k refers to the species mass fraction of the k^{th} species).

$$\alpha = \frac{Y_{H_2}}{Y_{H_2} + Y_{kero}} \tag{5.6}$$

The elemental mass fraction (Z_i, elemental mass fraction of the i^{th} chemical element/atom) should be utilized, as it is conserved throughout the flow field in both burnt and unburnt gases. The elemental mass fractions can be reconstructed from the species mass fractions Y_k, obtained from the CFD species transport equations. Subsequently, Y_k can be converted to Z_i by using Equation 5.7:

$$Z_i = \sum_{k=1}^{N_s} \frac{n_{i,k} M_i}{W_k} Y_k, \tag{5.7}$$

The parameter $n_{i,k}$ denotes the number of atoms of element i in species k, M_i is the atomic mass of element i, and W_k is the molecular weight of species k. The quantity α can now be obtained using Z_i. Hydrogen originating from the H_2 fuel may be present either in unburnt H_2 or in its combustion products. The collection of these hydrogen-containing contributions is denoted as Z_{H,H_2} (hydrogen originating from the H_2 fuel or present as H_2 itself). If instead the species mass fractions Y_k were used directly, hydrogen present in combustion products would not be consistently accounted for, since only H_2 itself would be considered. Equation 5.8 is analogous to the formulation given in Equation 5.6, where the mass fraction of H_2 fuel with respect to the total fuel mass (kerosene and hydrogen combined) is defined. In contrast, Equation 5.8 is formulated using the elemental mass fractions, Z_i.

$$\alpha = \frac{Z_{H,H_2}}{Z_H + Z_C} \tag{5.8}$$

It can be noted that the oxidizer (air) does not contain any carbon or hydrogen, while the fuels do not contain any nitrogen or oxygen; hence, the elemental mass fraction of total fuel can simply be determined by $Z_H + Z_C$. Thereafter, the elemental hydrogen fraction originating from hydrogen fuel Z_{H,H_2} should be determined, which is all the hydrogen in the domain except for the hydrogen originating from the $C_{11}H_{22}$, the employed kerosene surrogate; therefore, Equation 5.9 can be constructed:

$$Z_{H,H_2} = Z_H - Z_{H,\text{kero}} \tag{5.9}$$

To determine the hydrogen originating from kerosene, denoted by $Z_{H,\text{kero}}$, the hydrogen-to-carbon ratio of the kerosene surrogate can be utilised. Therefore, a unity Lewis number assumption is introduced such that each carbon atom remains associated with its corresponding number of hydrogen atoms originating from kerosene. This assumption suppresses preferential diffusion effects, ensuring that the hydrogen and carbon originating from the kerosene fuel remain closely coupled within the continuum fields and do not separate due to differential transport. It should be emphasized that this assumption is only employed for the retrieval of $Z_{H,\text{kero}}$ and, consequently, α. The governing equations themselves do not rely on the unity Lewis number assumption. Section 5.2.2 describes how α is used in the TFM.

Since all carbon atoms originate exclusively from kerosene, each carbon atom can be associated with a fixed number of hydrogen atoms determined by the surrogate fuel composition. Under the unity Lewis number assumption, this hydrogen remains linked to its corresponding carbon atom, allowing the hydrogen contribution originating from kerosene to be inferred directly from the carbon content. Consequently, tracking the carbon content provides a means of determining the corresponding hydrogen fraction originating from kerosene.

This relation is expressed in Equation 5.10, where $a_{H,\text{kero}}$ and $a_{C,\text{kero}}$ represent the number of hydrogen and carbon atoms in the kerosene surrogate, respectively, while M denotes the corresponding atomic weights. Together, these terms define a constant hydrogen-to-carbon mass ratio for the kerosene fuel. This ratio, shown within the brackets, is subsequently multiplied by the retrieved carbon-based quantity Z_c from the species transport equations to obtain $Z_{H,\text{kero}}$.

$$Z_{H,\text{kero}} = \left(\frac{a_{H,\text{kero}}}{a_{C,\text{kero}}} \frac{M_H}{M_C}\right) Z_C \tag{5.10}$$

The local α is obtained by combining the contributions from Equations. 5.8, 5.9, and 5.10, leading to the final formulation shown in Eq. 5.11.

$$\alpha = \frac{Z_H - \frac{a_{H,\text{kero}} M_H}{a_{C,\text{kero}} M_C} Z_C}{Z_H + Z_C} \tag{5.11}$$

Building on the definition of the local fuel-split parameter α, the local equivalence ratio ϕ is now introduced for the multi-fuel model. It can be expressed as a function of the local mixture fraction ξ and its stoichiometric value ξ_{st}, as shown in Equation 5.12.

$$\phi = \frac{\xi}{1-\xi} \frac{1-\xi_{st}}{\xi_{st}} \tag{5.12}$$

The local mixture fraction is defined using the formulation proposed by Bilger [74], as given in Equation 5.13.

$$\xi = \frac{\beta - \beta_{ox}}{\beta_{fuel} - \beta_{ox}} \tag{5.13}$$

The calculation of β is performed by Equation 5.14:

$$\beta = 2 \sum_k \frac{a_{C,k} Y_k}{W_k} + \frac{1}{2} \sum_k \frac{a_{H,k} Y_k}{W_k} - \sum_k \frac{a_{O,k} Y_k}{W_k} \tag{5.14}$$

Here $a_{C,k}$, $a_{H,k}$ and $a_{O,k}$ represent the total of carbon, hydrogen and oxygen atoms in the k^{th} species, respectively. Now considering the β_{fuel} for the hydrogen-kerosene blending case. The local mass-based hydrogen share α can here be utilized, providing an accurate fuel split representation.

$$\beta_{fuel} = \left(2 \frac{a_{C,H_2}}{W_{H_2}} + \frac{1}{2} \frac{a_{H,H_2}}{W_{H_2}} \right) \alpha + \left(2 \frac{a_{C,\text{kero}}}{W_{\text{kero}}} + \frac{1}{2} \frac{a_{H,\text{kero}}}{W_{\text{kero}}} \right) (1-\alpha) \tag{5.15}$$

The oxidizer contribution β_{ox} is then formulated as shown in Equation 5.16:

$$\beta_{ox} = -\frac{a_{O,O_2} Y_{O_2}}{W_{O_2}} \tag{5.16}$$

The stoichiometric mixture fraction is the only variable left from Equation 5.12. However, this can be calculated using relation 5.17 with the AFR_{st} retrieved again from Equation 5.5, using the local α instead of the α_g.

$$\xi_{st} = \frac{1}{1 + AFR_{st}} \tag{5.17}$$

The complete set of parameters to be defined comprises HPS_g, α_g, ϕ_g, α, and ϕ. With their respective definitions and formulations established, the discussion of these quantities is now concluded.

5.2.2. Thickened Flame Combustion Modeling for Multi-Fuel

The thickened flame model artificially thickens the flame front to allow the flame to be resolved directly on the LES grid to manage computational cost [76]. The thickening is done while preserving the laminar flame speed. The flame can be thickened by artificially increasing the diffusivity. Based on laminar premixed flame theory, the laminar flame speed S_L and flame thickness δ_l are related by Equation 5.18, where D is the molecular diffusivity and $\bar{\omega}$ is the mean reaction rate.

$$S_L \sim \sqrt{D\bar{\omega}}, \quad \delta_l^0 \sim \frac{D}{S_L} \tag{5.18}$$

To thicken the flame front δ_l, a thickening factor is applied, as represented in Equation 5.19, where $N = 8$ and Δ denotes the local mesh size. The value $N = 8$ is adopted based on reference studies in which this factor was successfully applied [65, 77].

$$F = \frac{N\Delta}{\delta_l} \tag{5.19}$$

The thickening factor is applied to the molecular diffusivity and therefore proportionally increases the flame-front thickness. However, applying this thickening factor also increases the laminar flame speed. Therefore, the reaction rate is corrected by dividing it by the same thickening factor, thereby preserving the original laminar flame speed, as shown in Equation 5.20 where D' denotes the molecular diffusivity of the thickened flame and $\bar{\omega}'$ the reaction rate of the thickened flame.

$$D' \rightarrow FD, \quad \bar{\omega}' \rightarrow \frac{\bar{\omega}}{F} \tag{5.20}$$

Flame thickening not only affects the laminar flame speed but also alters the interaction between the flame and turbulence. A thicker flame front is less sensitive to turbulence; hence, the flame will be less wrinkled. Figure 5.1 illustrates the reduced sensitivity of the thickened flame front to wrinkling. Flamelet "a" is the original non-thickened flame, showing significant disturbances by the turbulent eddies. On the other hand, the thickened flame represented by "b" experiences less deformation due to its broader flame front. The surface area of the flame might therefore decrease, inherently lowering the reaction rate; a correction has to be applied.

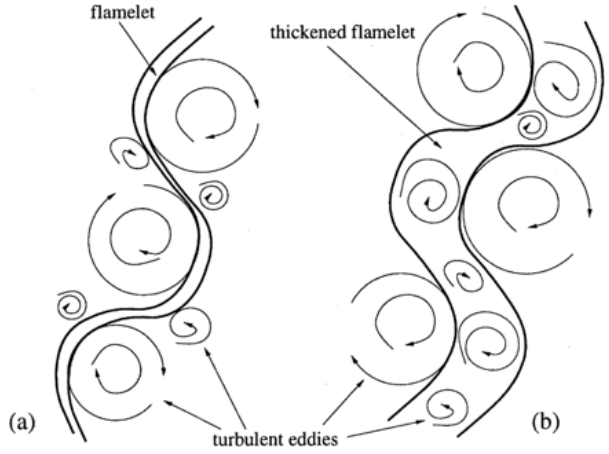

Figure 5.1: Schematic illustration of the reduced flame wrinkling resulting from artificial flame thickening [78]

To account for this reduced sensitivity to turbulence–flame interaction, the efficiency function E is introduced. This function represents the ratio of flame wrinkling between the unthickened and thickened flame, as shown in Equation 5.21, where Ξ denotes the wrinkling factor.

$$E = \frac{\Xi(\delta_l)}{\Xi(\delta_l^{TFM})} \tag{5.21}$$

The formulation of the wrinkling factor Ξ, as proposed by Charlette, is employed [79].

$$\Xi(\delta_l) = 1 + \min\left(\frac{\Delta}{\delta_l}, \Gamma\left(\frac{\Delta}{\delta_l}, \frac{u'_\Delta}{S_L}\right), \mathrm{Re}_\Delta^\beta \frac{u'_\Delta}{S_L}\right) \tag{5.22}$$

where S_L is the laminar flame speed, δ_l is the laminar flame thickness, Re_Δ is the sub-grid scale Reynolds number, β is the thickening factor exponent, u'_Δ is the characteristic turbulent velocity at the filter scale Δ, and Γ is a function accounting for the unresolved strain rate. The thickened-flame source term in the species equations, $\dot{\omega}'_k$, is then modified as shown in Equation 5.23.

$$\dot{\omega}'_k = E\frac{\dot{\omega}_k}{F} \tag{5.23}$$

The thickened-flame approach is applied to the species transport equations, with flame thickening applied to each species equation as well as the energy equation. Equation 5.24 shows the transport equation for the k^{th} species. In the thickened-flame formulation, the reaction rate is evaluated using the Arrhenius expressions defined in the reaction mechanism, as discussed in Section 2.5 and Equation 2.9.

$$\frac{\partial \rho Y_k}{\partial t} + \nabla \cdot (\rho \mathbf{u} Y_k) = \nabla \cdot (\rho D \nabla Y_k) + \dot{\omega}_k \tag{5.24}$$

Now the thickening procedure is applied, resulting in Equation 5.25.

$$\frac{\partial \rho Y_k}{\partial t} + \nabla \cdot (\rho \mathbf{u} Y_k) = \nabla \cdot (\rho D F E \nabla Y_k) + E \frac{\dot{\omega}_k}{F} \tag{5.25}$$

Now consider the multi-fuel H_2-kerosene flames, the S_L and δ_l in Equations 5.19 and 5.22 are not solely functions of the local equivalence ratio. In fully premixed single-fuel flames, these quantities are constant, whereas in partially premixed single-fuel flames they depend on the local equivalence ratio. However, for H_2-kerosene combustion, the non-uniform mixing of the two fuels must also be accounted for. Therefore, S_L and δ_l must be computed as functions of both the local equivalence ratio ϕ and the hydrogen-to-kerosene ratio α. The novel approach of [65] has been adopted to retrieve the δ_l and S_L. A series of one-dimensional freely propagating flame simulations have been performed in CANTERA to generate these quantities over a range of ϕ and α. The range of ϕ is chosen sufficiently wide to ensure that the equivalence ratios corresponding to heat release, and thus flame presence, are fully captured. The parameter α spans the full fuel composition range, from pure kerosene to pure H_2, from unity to zero. This resulted in two look-up tables from which the corresponding values for the quantities could be retrieved using bilinear interpolation. The look-up tables are visualized in Figure 5.2.

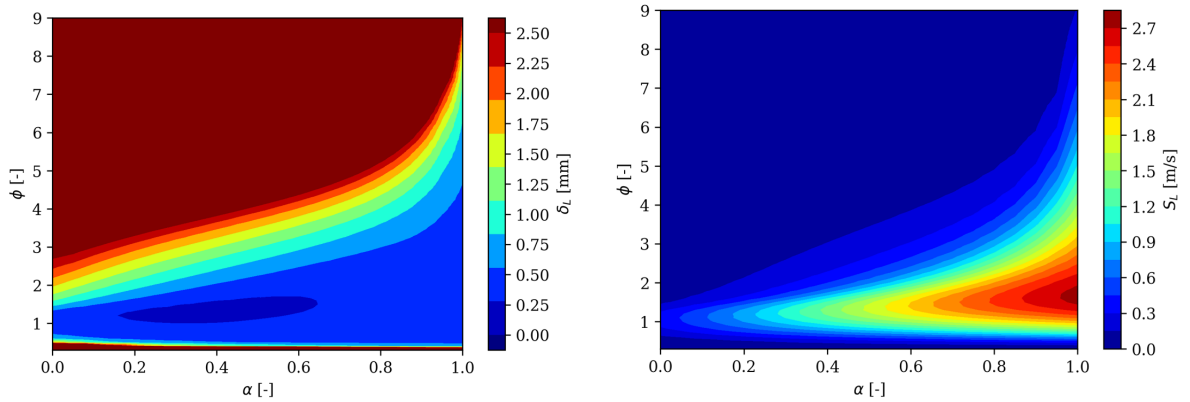

(a) Laminar flame thickness look-up table

(b) Laminar flame speed look-up table

Figure 5.2: Contours of the look-up tables for laminar flame speed and laminar flame thickness as functions of equivalence ratio and hydrogen-to-kerosene ratio for dual-fuel TFM deployment [65]

The freely propagating flame simulations are performed using CANTERA with the Z79 reaction mechanism [29]. Z79 is a reduced kinetic scheme for kerosene combustion comprising 31 species and 79 reactions. It maintains good agreement with detailed mechanisms while keeping computational cost manageable. Notably, Z79 includes a detailed hydrogen oxidation pathway through its base methane combustion sub-mechanism, allowing it to accurately describe hydrogen oxidation even in kerosene-focused formulations.

The next consideration concerns the partially premixed regime. The thickened flame model was initially proposed by [76] for premixed systems. In this formulation, flame thickening is applied inherently only when the gradient of species mass fractions is non-zero in the species transport equations (see Equation 5.25); when $\nabla Y_k = 0$, the diffusion term, including the artificial thickening contribution, vanishes and the flow field remains unaffected. In fully premixed systems, ∇Y_k is non-zero only within the flame front, as no additional mixing layers are present. In partially premixed combustion, however, mixing layers coexist with reaction zones, and the model must be adapted such that thickening is applied exclusively within the flame front. For this purpose, a flame sensor was introduced by [80], leading to the Dynamic Thickened Flame (DTF) model.

The flame sensor acts as an indicator of the reaction zone. Its role in different combustion regimes is illustrated in Figure 5.3a. The sensor is equal to zero in the cold gas region, thereby suppressing artificial diffusion and flame thickening. It approaches unity within the flame zone, enabling the thickened flame formulation. Downstream of the flame, in the burnt gas region, the sensor returns to zero, and thickening is again disabled. The flame sensor is applied to the diffusivity terms and is represented by Equation 5.26. Here the D' is again the molecular diffusion term in the TFM, E the efficiency function, F the thickening factor and S the flame sensor, D_{turb} the turbulent

diffusion term and D_{lam} the laminar diffusion term.

$$D' = D_{\text{lam}} E\,(1 + (F-1)S) + D_{\text{turb}}(1-S) \tag{5.26}$$

The flame sensor proposed by [80] is based on a tanh-function formulation (see Figure 5.3b), and is defined in Equation 5.27, which is adopted in the present work.

$$\mathcal{S} = \tanh\left(\beta \frac{|\Omega|}{|\Omega_0|}\right) \tag{5.27}$$

The definition consists of a Ω, the observed quantity for detection (i.e. heat release rate or reaction rates), Ω_0, the reference value for the flame (in this work, the maximum obtained value of the observed quantity in the domain). The tanh function maps the sensor between zero and unity (see Figure 5.3b). Also, only absolute values of both Ω and Ω_0 are used to bound the horizontal axis to positive values. The sensitivity of the sensor can be adjusted with the β parameter, as also depicted in Figure 5.3. Regarding $\beta = 1$ as a reference, increasing the parameter will make the sensor reach unity earlier, inherently making the sensor more sensitive, as can be observed by the $\beta = 2$ sensor in the figure. The reverse can also be utilized to decrease the sensitivity; this is shown by the $\beta = 0.5$ sensor in the figure. In the present work, a $\beta = 5$ is implemented based on reference work [77, 65].

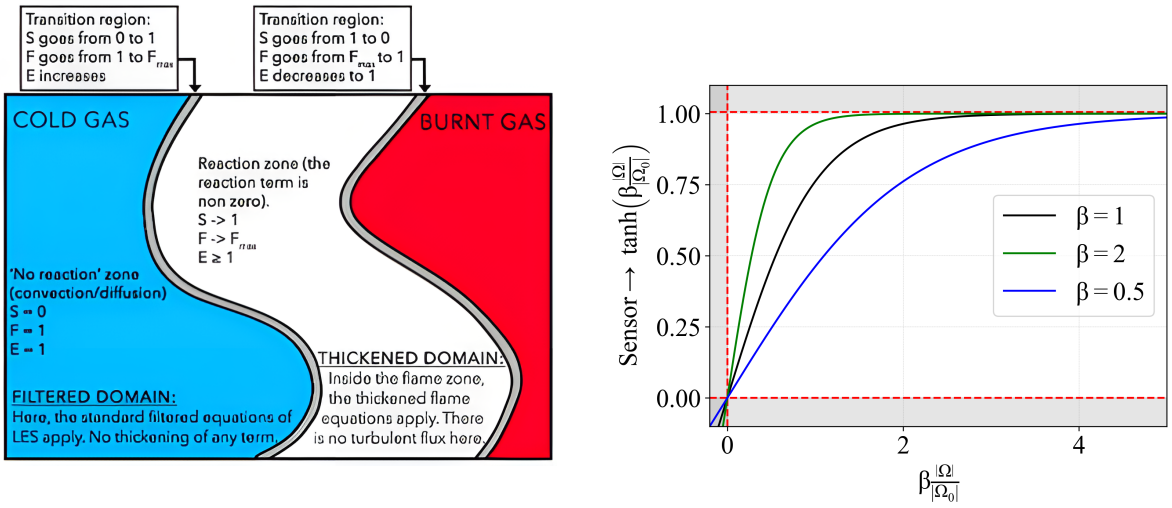

(a) Schematic representation of the DTF model [81]

(b) The flame sensor definition as proposed by [80]

Figure 5.3: DTF regimes and flame sensor implementation

5.3. Modeling of the Spray

The atomizer generates a droplet distribution through which liquid fuel is injected into the combustor. From this point onward, the droplets interact with the surrounding flow field within the simulation domain. The Discrete Phase Model (DPM) is adopted to describe the interaction between the liquid kerosene droplets and the gaseous environment. However, before this interaction can be modeled, the spray boundary conditions must first be defined, as they prescribe the initial conditions of the injected spray and thereby determine the effective atomizer representation used in the simulations. These boundary conditions include several parameters such as the injection characteristics and the initial droplet properties. In particular, the initial droplet size distribution is described using the Rosin–Rammler method [24], also referred to as the Weibull distribution, and is represented by Equation 5.28:

$$1 - Q = \exp\left(-\left(\frac{D}{X}\right)^q\right) \tag{5.28}$$

Here, q is the spread parameter, Q is the cumulative volume fraction of droplets with a diameter smaller than D, and X is a representative diameter. The parameter q governs the width of the distribution and thus the spread of droplet sizes. The representative diameter X is estimated using the Lefebvre correlation [24], through the Sauter

Mean Diameter (SMD) (defined in section 2.3).

$$\text{SMD} = 2.25\,\sigma_L^{0.25}\mu_L^{0.25}m_l^{0.25}\Delta P^{-0.5}\rho_A^{-0.25} \tag{5.29}$$

The parameter σ_L is the surface tension of the liquid (N/m). The dynamic viscosity of the liquid is denoted by μ_L (Pa·s). The mass flow rate of the liquid is given by m_l (kg/s). The pressure difference across the atomizer is represented by ΔP (Pa). Finally, ρ_A is the density of the surrounding gas or air (kg/m^3). X can be retrieved based on the spread parameter and the SMD using Equation 5.30, where Γ denotes the gamma function.

$$\frac{\text{SMD}}{X} = \Gamma\left[\left(1-\frac{1}{q}\right)\right]^{-1} \tag{5.30}$$

This distribution introduced the liquid spherical Lagrangian particles, hence, neglecting initial primary breakup (see section 2.3). Thereafter, the interaction between the droplets and surrounding gas are governed by a Reynolds-number dependent drag coefficient method [82]. The trajectory of a droplet is determined by integrating the force balance acting on the particle within a Lagrangian reference frame. In this formulation, the particle inertia is balanced by the sum of all external forces acting on it. The resulting equation of motion can be expressed as shown in Equation 5.31.

$$m_p\frac{d\vec{u}_p}{dt} = m_p\frac{\vec{u}-\vec{u}_p}{\tau_r} + m_p\vec{g}\,\frac{\rho_p-\rho}{\rho_p} + \vec{F} \tag{5.31}$$

Here, m_p denotes the particle mass, $\vec{u}$ is the fluid-phase velocity, and $\vec{u}_p$ is the particle velocity. Furthermore, ρ and ρ_p represent the fluid and particle densities, respectively, while $\vec{F}$ denotes any additional external force acting on the particle, for example, the Magnus lift force and the virtual mass force. The term $m_p(\vec{u}-\vec{u}_p)/\tau_r$ corresponds to the drag force, where τ_r is the particle relaxation time defined in Equation 5.32. The particle relaxation time is the time required for a particle to adjust its velocity and match the speed of the fluid surrounding it.

$$\tau_r = \frac{\rho_p d_p^2}{18\mu}\frac{24}{C_d\,Re} \tag{5.32}$$

Here, μ denotes the dynamic viscosity of the fluid, d_p is the particle diameter, and Re is the particle Reynolds number based on the slip velocity, defined in equation 5.33. The C_d denotes the droplet drag coefficient, which is a function of the Reynolds number and a shape factor accounting for deviations from sphericity in non-spherical particles.

$$Re = \frac{\rho d_p\left|\vec{u}_p-\vec{u}\right|}{\mu} \tag{5.33}$$

Furthermore, the secondary breakup (see again section 2.3) is modeled by the methods proposed by [83]. This model describes spray atomization as a random breakup process rather than a fixed deterministic rule. It uses a statistical (Fokker–Planck) description to predict how droplet sizes evolve over time, with breakup rates linked to the local Weber number and coupled to the gas flow. Instead of tracking only single "average" droplets, it allows a full distribution of droplet sizes to develop while still remaining computationally efficient by grouping similar droplets into parcels.

The droplet heating and eventually evaporation are considered by models introduced by [84]. A fuel droplet injected into a hot gas initially undergoes a heating phase, during which heat is transferred from the surrounding gas to the droplet mainly through convection (and, in some cases, radiation). In this stage, the droplet temperature increases while its mass and diameter remain approximately constant. Once the surface temperature reaches conditions where phase change becomes significant, evaporation starts and the droplet begins to lose mass. From this point onward, the droplet continuously shrinks as liquid fuel is converted into vapour and transported into the gas phase. The overall process is therefore characterised by a coupled evolution of droplet heating and evaporation until complete evaporation.

6

Design, Measurement Equipment and Numerical Setup

First, the design of the HOPE combustor is described, followed by a discussion of the installed measurement devices. The numerical domain and mesh are presented next, prior to detailing the simulation setup. The primary SBES setup is introduced first, followed by the RANS simulations, which are used to improve the high-fidelity SBES simulation and to explore performance at engine operating conditions. Lastly, an overview of the simulations, including their corresponding assumptions and limitations, is provided.

6.1. The HOPE-Combustor

The subject of the research is the HOPE-combustor, consisting of a chamber which is a 275 mm long quartz cylinder with an inner diameter of 104 mm, connected to an outlet metal section of the same diameter, giving a total length of 414 mm. At the chamber exit, a 3 mm thick plate with a 40 mm orifice is mounted. This element helps suppress thermoacoustic instabilities by adding acoustic damping. Figure 6.1 shows the CAD of the system, the combustor is supported by four rods and rests on a rectangular plate. The inlet types have a dedicated ring (which contain the plenums), together forming the concentric rings shown in the figure. A swirl stabilized concept has been adopted; hence, swirling is introduced on the largest ring. The second ring is dedicated to the hydrogen injection. The third ring provides the axial air which is used to control the swirling intensity, providing a mechanism for flashback prevention which is of fundamental importance in premixed H_2 flames. The central pipe provides the kerosene injection. There are four inlets along the circumference of the system for each type (swirl air, hydrogen, axial), except for kerosene as it is centrally injected.

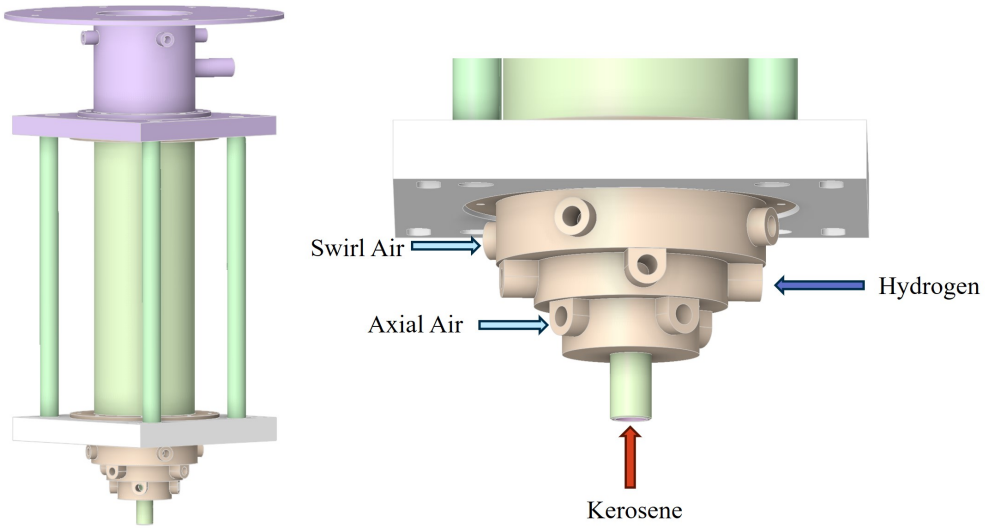

Figure 6.1: The external view of the HOPE combustor, illustrating the inlet configuration, including the swirling and axial air inlets as well as the hydrogen and kerosene fuel injection ports.

The injector interior is shown in Figure 6.2. The quartz surfaces represent the inner chamber walls, and the injection points are highlighted. It can be observed that swirl air, hydrogen, and axial air are routed through dedicated channels toward the swirler, whereas kerosene is supplied via the SIMPLEX atomizer (see Section 2.3). More specifically, kerosene is injected via a 60° solid-cone pressure-swirl atomizer (Fluidics Instruments FI-0.15-60SF (FI015), rated at 9.5 g/min at P = 10 bar-g). The swirler geometry is illustrated in the right-hand figure. Swirling air passes through the vanes, which impart angular momentum to the flow. In contrast, axial air is introduced through straight ports placed near the atomizer, providing an axial mass flow to the chamber. Hydrogen is also injected in an axial configuration. Only one injection point is annotated, although multiple identical locations are distributed along the circumference. The kerosene bypasses the swirler entirely as it is injected through the atomizer.

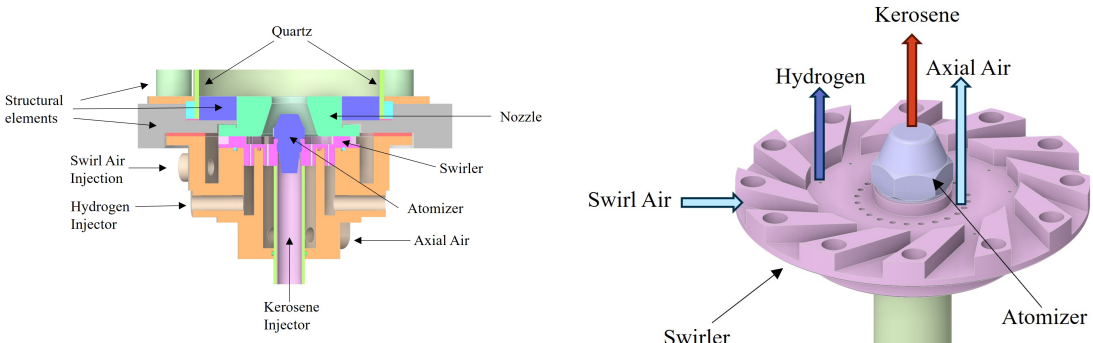

(a) Cross-sectional view of the injection system

(b) Perspective view on the swirler

Figure 6.2: The interior view on the HOPE-combustor denoting the main parts of the system.

The combustor is designed to operate in a partially premixed regime with respect to hydrogen. Hydrogen and air mix downstream of the swirler in the nozzle section, such that fuel and oxidizer form a dominantly premixed mixture before combustion. In contrast, kerosene is injected as a spray and does not necessarily mix with the oxidizer before entering the combustor. However, mixing may still occur within the chamber prior to flame stabilization. Premixed operation is employed to benefit from reduced NOx emissions compared to diffusion-dominated combustion. However, premixed combustion is inherently susceptible to flashback, which imposes constraints on the design. To mitigate this risk, the mixing tube length is limited, ensuring only partial premixing is achieved. Furthermore, an important feature of the design is the axial air inlet (AAI) fraction, as defined in

Equation 6.1.

$$\text{AAI} = \frac{\dot{m}_{\text{axial air}}}{\dot{m}_{\text{total air}}} = \frac{\dot{m}_{\text{axial air}}}{\dot{m}_{\text{axial air}} + \dot{m}_{\text{swirl air}}} \tag{6.1}$$

Increasing the axial air flow, corresponding to a higher axial air inlet (AAI) fraction due to air bypassing the swirler, induces additional axial momentum within the combustor, which in turn provides push-back on the flame. This pushback reduces the likelihood of upstream flame propagation and therefore acts as a flashback mitigation mechanism.

6.2. Measurement Equipment

This design has been manufactured and tested in the TU-Delft Sustainable Propulsion Lab. The diagnostics consist of DSLR-based flame imaging and OH*/CH* chemiluminescence measurements. Flame visualization is performed with an Olympus OM-1 Mark II camera, while OH*/CH* signals are recorded using a LaVision CMOS camera (imager M-lite 5M) equipped with an IROx intensifier and a 308 nm bandpass filter. For each operating condition, 1000 single-shot images are collected at 50 Hz, ensemble-averaged, and processed via an inverse Abel transform to reconstruct the flame structure.

6.3. Numerical Domain and Mesh

The numerical domain is constructed by retrieving only the fluid domain of the CAD from figure 6.1 and 6.2. Figure 6.3 shows the full numerical domain. The outlet is located at the top of the orifice as represented by the light red circle. The two blue circles denote air inlets, the circle with the smallest diameter corresponds to the AAI and the other shows the swirl air. The hydrogen inlet is represented by the green circle in between the air inlets. For kerosene, a discrete phase injection is placed on the top of the atomizer resulting in a spray as visualized in yellow. Non-highlighted faces are considered as walls. The mesh can be observed in the close-up part of the figure and is composed of polyhedral elements in the core of the domain and 10 prism layers in the near-wall region to model the boundary layer. Progressive refinements down to 400 μm are applied in the hydrogen and kerosene flame front regions. This refinement is based on the anticipated locations of the shear layers, where the flame is expected to stabilize according to preliminary simulations and reference work [65, 77, 30]. Also, an extra refinement near the atomizer exit has been applied to accurately capture fluid-gaseous interaction in this region. Eventually, the domain contains approximately 7.7 million cells. In case HPS_g=0.0%, the hydrogen inlet and its plenum are omitted from the simulation, slightly reducing the number of cells and preventing the potential numerical errors originating from this compartment.

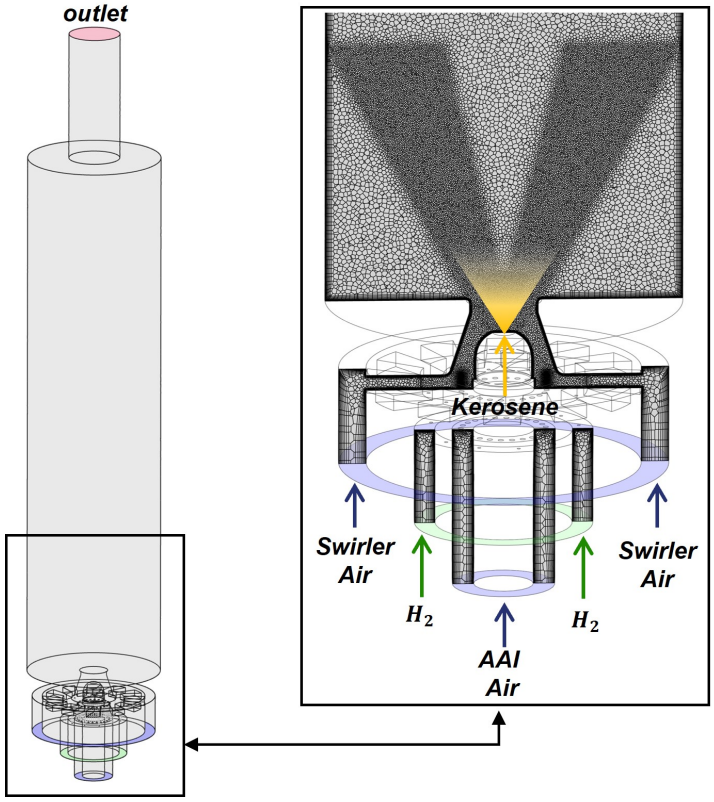

Figure 6.3: SBES - numerical domain and mesh

The HOPE-combustor has a symmetrical domain; however, periodic boundary conditions should generally be avoided in SBES of reacting flows because they artificially constrain the inherently three-dimensional and asymmetric nature of turbulent combustion. By forcing the flow and flame structures to mirror across a plane, turbulence flame interactions will be simplified losing significant accuracy of the SBES for which it was adopted [69, 85]. Therefore, the potential reduction in computational cost cannot be exploited, as the domain cannot be partitioned into six equivalent segments owing to asymmetric resolved turbulent structures in the instantaneous flow field.

The computational cost of SBES is substantial, inherently limiting the research capability. Therefore, RANS is adopted for computational efficiency. The turbulent structures are not resolved by the governing equations, as they are entirely represented by the turbulence model, and unsteady effects are neglected, thereby improving com-

putational efficiency. Furthermore, this also allows RANS to adopt the periodic boundary conditions, resulting in an even more efficient method. Therefore, regarding computational cost, RANS is more efficient than SBES and is preferred when computational efficiency is most critical. The RANS domain differs from the SBES domain as it is only one sixth due to the periodicity, as can be observed by 6.4. Two periodic faces can be distinguished and span over the radial and axial axes, with a 60° angle between the faces. The remaining faces are treated as walls.

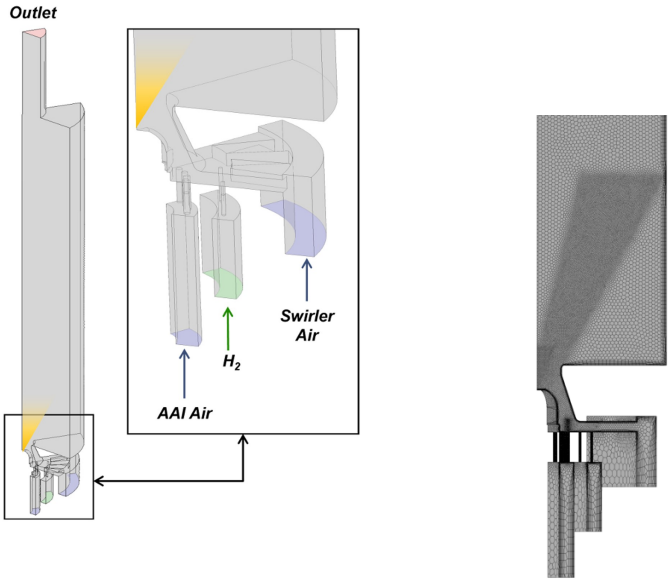

Figure 6.4: RANS - numerical domain and mesh

6.4. Simulation setup of the SBES

The atmospheric test setup is simulated with high-fidelity SBES for HPS_g=0.0%, HPS_g=30.0%, HPS_g=60.0% and HPS_g=100.0%, covering approximately the full range of dual fuel power-split configurations. In Table 6.1, the power across the simulations is kept at a constant 10kW. The pressure is specified on the outlet, ensuring atmospheric pressure conditions. Mass flow rates are specified for all inlets (swirler air, hydrogen, AAI and kerosene). The total air mass flow rate does not change across the various HPS_g cases. The inflow air temperature (swirling and AAI) as well as the hydrogen inflow temperature are fixed and are set to the same value (293.15K), while a slight elevation of the inflow temperature has been applied for kerosene (300K), as the inlet kerosene is slightly elevated, as the atomizer is located upstream of the air inlets, experiencing a small portion of pre-heating. The walls are initially treated as adiabatic, under the assumption that heat transfer through the walls does not significantly affect the flame shape. The no-slip condition is imposed on all the walls, allowing for boundary layer development. Also, the walls are considered smooth. Regarding the spray, a solid-cone (SC) atomiser is placed for all the cases. The cone-angle initialization will be 60 degrees regardless of the mass flow through the atomizer, assuming that the atomizer performs under rated conditions. The spread parameter ”q” (see Equation 5.28) is also kept constant at 3.0. For all cases, the Z79 reaction mechanism is employed as it is a reduced mechanism for jet-A1 containing a hydrogen pathway through its methane combustion sub-mechanism. The material properties are derived from the thermochemical and transport data contained within this mechanism and its associated transport database, providing the parameters required to characterize the gas mixture behaviour across the relevant range of temperatures and pressures.

Hydrogen Power Share [%]	0.0%	30.0%	60.0%	100.0%
Constants				
Thermal power [kW]	10.0	10.0	10.0	10.0
Outlet Pressure [bar]	1.0	1.0	1.0	1.0
$\dot{m}_{air}$ [g/s]	6.68	6.68	6.68	6.68
Inlet Turbulence Intensity [%]	5	5	5	5
AAI [-]	0.2	0.2	0.2	0.2
Air temperature [K]	293.15	293.15	293.15	293.15
H_2 temperature [K]	–	293.15	293.15	293.15
Kerosene temperature [K]	300	300	300	–
Wall temperature	ad	ad	ad	ad
Wall shear	no-slip	no-slip	no-slip	no-slip
Wall roughness	smooth	smooth	smooth	smooth
Spray Cone	solid	solid	solid	–
Spray velocity magnitude [m/s]	20	20	20	–
Spray cone angle [deg]	60	60	60	–
Spray outer radius [mm]	0.58	0.58	0.58	–
Spray q [-]	3.0	3.0	3.0	–
Reaction Mechanism	Z79	Z79	Z79	Z79
Variable Parameters				
Equivalence ratio ϕ [-]	0.522	0.494	0.467	0.430
Kerosene mass flow rate [g/s]	0.232	0.162	0.093	–
H_2 mass flow rate [g/s]	–	0.0251	0.0501	0.0835
Spray SMD [μm]	13.6	18.44	29.4	–

Table 6.1: Operating conditions for different hydrogen power shares for simulating the experimental setup at atmospheric conditions for SBES

Considering the variable parameters, the ratio of fuel mass flows determines the HPS_g (equation 5.2) and is set to match the HPS_g cases. The global equivalence ratio decreases monotonically with increasing HPS_g. As the hydrogen share increases, less total fuel mass is required to maintain the same power due to the LHV difference between kerosene and H_2, resulting in a leaner global mixture. All cases therefore operate under lean conditions throughout the full HPS_g range. Regarding the spray, the reduced pressure across the atomizer results in an increase of the SMD (see equation 2.2), and the retrieved values are shown in the table for the various cases. The retrieved agreement with the experiments will be discussed in section 7.1, this will be followed by a topology description of the flame in section 7.2.

6.5. Setup for the RANS-Simulations

This section presents the numerical setup of the additional RANS-based simulations used to complement the high-fidelity SBES analysis. In particular, it covers the spray sensitivity study, the implementation of conjugate heat transfer (CHT) derived thermal boundary conditions, and the extension towards engine operating conditions.

The spray structure plays a significant role in conventional combustion processes [28], and therefore an accurate representation in the SBES simulations is expected to be essential. However, the exact spray boundary conditions are not known, necessitating a sensitivity analysis to identify the most influential parameters. Due to the large number of required simulations, a RANS–FGM (Flamelet Generated Manifold) approach is adopted for computational efficiency, albeit at the cost of reduced predictive ability compared to SBES. The setup of the spray sensitivity study is presented in Section 6.5.1, while the corresponding results are discussed in Section 7.3.2.

The high-fidelity SBES simulation was performed assuming adiabatic walls; however, this may be an overly simplified assumption and could introduce errors. To this end, a Conjugate Heat Transfer (CHT) simulation is employed, which solves for both the fluid and the conduction in the solids, thereby bypassing the need for assumed wall temperature boundary conditions. Nevertheless, such a computation requires significant computational effort within SBES, and RANS is therefore adopted for this purpose. The resulting wall temperature distributions are subsequently retrieved from the RANS-CHT simulation and imposed on the SBES as a boundary condition. The simulation setup is described in Section 6.5.2, while the corresponding results are presented in Section 7.3.1.

The previous setups aimed at simulating the laboratory test setup currently placed in the TU Delft Sustainable Propulsion Lab. Eventually, as technology readiness levels evolve, the system must be able to operate under actual engine conditions. Adopting SBES for simulating these conditions is computationally expensive; therefore, a RANS approach is employed. The setup of this simulation will be further explained in Section 6.5.3, while the corresponding results are presented in Section 7.4.

6.5.1. Simulation Setup: Spray Boundary Conditions Sensitivity

The spray sensitivity analysis is performed exclusively for the HPS_g=0.0% case, as the pure kerosene configuration eliminates the additional complexity associated with multi-fuel interactions. The same geometric setup and operating conditions as used in the SBES simulations are adopted, as reported in Table 6.1, with the added consideration of periodicity in the RANS domain. The spray boundary conditions of interest are then systematically imposed in the simulations to evaluate their influence on the solution. Accordingly, the cases listed in Table 6.2 are defined and simulated. A Flamelet-Generated Manifold (FGM) approach is employed to account

Table 6.2: Overview of spray boundary condition sensitivity cases.

Case	Value	Description
BASE	Reference	Baseline solid-cone SBES spray configuration
A1	–	Non-uniform injector mass-flow distribution
A2	–	Spatial staggering of droplet injection
B1	–	Hollow-cone spray model
B2	0.5	Hollow-Cone with Positive swirl fraction
B3	-0.5	Hollow-Cone with Negative swirl fraction
C1	30 ms^{-1}	Increased droplet injection velocity
C2	10 ms^{-1}	Reduced droplet injection velocity
D1	$q = 2$	Lower spray spread exponent
D2	$q = 4$	Higher spray spread exponent
E1	10.5 μm	Reduced SMD, associated with ΔP=+25% across the atomizer
E2	18.2 μm	Increased SMD, associated with ΔP=-25% across the atomizer

for turbulence–chemistry interactions in the RANS simulations. The FGM is based on flamelets that provide temperature and species mass fractions as functions of the progress variable, the mixture fraction, their respective variances and enthalpy. Steady laminar opposed-flow diffusion flamelets are used at atmospheric pressure and temperature.

6.5.2. Simulation Setup: Conjugate Heat Transfer

The CHT simulations are applied to the HPS_g=0.0% and HPS_g=100.0% cases to improve the single-fuel agreement prior to proceeding to the dual-fuel configurations. The objective of this analysis is to retrieve the temperature on the backplate of the combustion chamber and the temperature distribution on the quartz. Similar to the treatment of spray boundary conditions, a Flamelet Generated Manifold (FGM) approach is employed to account for turbulence–chemistry interaction (TCI), using Steady laminar opposed-flow diffusion flamelets.

Although the conjugate heat transfer (CHT) framework eliminates the need for thermal boundary conditions directly imposed at fluid–solid interfaces, the thermal treatment of the newly introduced solid–solid interfaces requires careful consideration, as thermal contact resistance (TCR) arises between contacting solid surfaces. Three possible types of solid-to-solid conditions are represented in Figure 6.5. In the disconnected case, where two surfaces are not in contact, no heat flux is exchanged between the solids and the interface is therefore treated as adiabatic or having an infinite TCR. At the other end, when heat is assumed to flow freely through the materials, no TCR is considered and the materials are treated as a single continuous solid.

Then there is the case of actual imperfect contact, containing a nonzero, non-infinite thermal contact resistance. The actual value of the TCR varies with interface temperature, surface roughness, and contact pressure and is investigated by [86] for practical engineering systems and conditions for contact between stainless steel surfaces, which is relevant to the case at hand. The Thermal Contact Conductance (TCC) was actually examined by [86], which is the inverse of the TCR. The experiments showed that a variety of possible values depending on the above mentioned factors, however, the lowest and the highest TCC for these practical systems reported in [86] were $1000 Wm^{-2}K^{-1}$ and $15000 Wm^{-2}K^{-1}$ respectively.

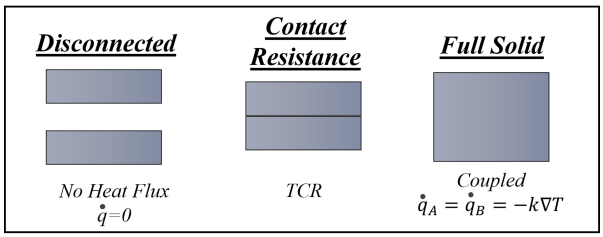

Figure 6.5: Solid-to-solid boundary conditions in the CHT-simulation

The CHT boundary conditions are represented in Figure 6.6, with the numerical mesh now including the solid blocks. The thermal contact resistance (TCR) is applied at the horizontal solid-solid interfaces (red). The resistance is incorporated by artificially adding wall thickness using Equation 6.5.2, where the thermal conductivity k= $16.27, Wm^{-1}K^{-1}$ corresponds to the material property of stainless steel.

$$t_{wall} = \frac{k}{TCC} \tag{6.2}$$

The vertical solid-solid interfaces (green) contain negligible contact pressure and are therefore treated as disconnected parts ($\dot{q}$=0). The solid–solid interface involving the quartz component (green) is also treated as a disconnected interface, as a thermal sealing layer is present between the contacting surfaces. The interface connected with the ambient surroundings (blue) is handled using convection utilizing equation 6.3.

$$\dot{q} = h(T_s - T_\infty) \tag{6.3}$$

The heat transfer coefficient (h) is set to an appropriate value for natural convection, h= $5, Wm^{-2}K^{-1}$. The T_∞ represents the ambient temperature, assumed to be 293.15 K. Further, the walls with a solid–fluid interface are not highlighted in Figure 6.5, as the temperature is computed by solving the energy equation and conduction within the solid, removing the need for thermal wall boundary conditions. The surfaces of the atomizer, plenums, ducts, swirler and orifice are assumed to have a limited effect on the results and are treated as adiabatic.

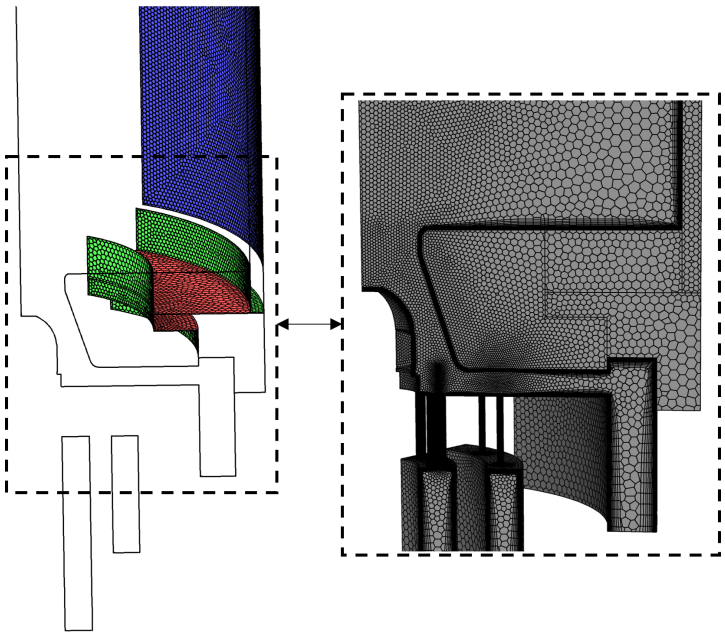

Figure 6.6: CHT wall boundary conditions and mesh

6.5.3. Simulation Setup: Engine Operating Conditions

The laboratory setup, currently, is only capable of investigating the system under reduced power settings and ambient temperature and pressure conditions. Therefore, to explore the system's performance in actual operating conditions, the flexibility of CFD simulations is utilized. This exploration will be performed under the most critical operating condition that the engine might have to endure: take-off at HPS_g=100.0%. The engine is required to provide (near) maximum thrust during take-off, eventually leading to the highest unburnt air temperature level out of the compressor. Engine cycle simulations have determined compressor outflow conditions, and the relevant parameters are listed in Table 6.3 for this H_2 take-off condition. The conditions are preliminary, as the development of the engine is still an active process. Furthermore, cooling flows are not incorporated.

Table 6.3: Preliminary compressor outlet conditions at HPS_g = 100% during take-off for the complete engine

Parameter	Symbol	Value
Compressor outlet pressure (static)	p_3	5,391,392 Pa or 53.20 atm
Compressor outlet air temperature	T_3	980.5 K
$\dot{m}_{air}$ (combustor inlet)	$\dot{w}_3$	31.4 kg/s
H_2 temperature	T_{fuel}	288 K
$\dot{m}_{H_2}$	$\dot{w}_{\text{fuel}}$	0.3558 kg/s

The Reynolds number increases drastically from simulating the test setup to the limiting engine operating conditions. The computational complexity scales with Reynolds number. This up-scaling is much steeper in LES compared to RANS [87]. Furthermore, since T_3 is significantly higher than $T_{ambient}$, the temperature of the unburned gases increases, leading to a considerable increase in the laminar flame speed S_L. The flame front will therefore become thinner, requiring a significantly higher thickening factor to have sufficient computational cells within the flame front. Therefore, the SBES-TFM will not be used, and RANS-FGM is adopted, accepting the associated compromises in accuracy.

The eventual targeted engine of the HOPE program is of an annular type, consisting of a finite number of swirlers. The exact number of swirlers is yet undetermined; however, based on the geometry and the reference engine (CFM International LEAP-1A), the number of swirlers was estimated (N_{swirl} = 18). Only a single swirler has to be

simulated. The swirler mass flow rates $\dot{m}_{H_2}$ and $\dot{m}_{air}$ are obtained by dividing the corresponding engine mass flows by the number of swirlers.

The power per swirler can be determined from $\dot{m}_{H_2}$ by multiplying it by LHV_{H_2}. Since both $\dot{m}_{H_2}$ and $\dot{m}_{air}$ are known, the equivalence ratio can be determined. The temperature and pressure correspond to the values reported in Table 6.3. The retrieved swirler parameters are listed in Table 6.4. The elevated temperature and pressure

Table 6.4: Swirler operating conditions for pure H_2 take-off

Power [MW]	$\dot{m}_{air}$ [kg/s]	$\dot{m}_{H_2}$ [kg/s]	T_{air} [K]	T_{H_2} [K]	Pressure [atm]	ϕ
2.367	1.74	0.0198	980.5	288	53.20	0.390

require a reconsideration of the reaction mechanism, as a mechanism suitable for H_2 combustion at unburnt conditions of 980.5 K and 53.2 atm must be identified. Two studies have been identified that compare reaction mechanisms under elevated temperature and pressure for H_2. The first to consider is [88], which aimed to improve hydrogen mechanisms over the following conditions: temperature 800 K to 2500 K, pressure 0.5 bar to 50 bar, and equivalence ratios (ϕ) from 0.3 to 5.0. A comparison within this range was performed among existing reaction mechanisms to identify the best-performing one, which was then used as a starting point for further development. The validated range almost covers the targeted simulation conditions. A thorough comparison was performed, and the reaction mechanisms were evaluated against experimental data for the corresponding conditions. The mechanisms were tested against ignition delay time (IDT), concentration profiles, laminar burning velocity measurements, and overall performance across the full dataset. The most important parameter was considered to be the flame speed, as the objective is to apply the mechanisms to steady RANS pure H_2 combustion. It was concluded that the mechanism developed by Keromnes et al. [89] performed best in terms of flame speed, and the overall performance was also optimal; therefore, it was selected as a base for further development.

The second study is [90]. A similar comparison of hydrogen mechanisms was performed using the same metrics as [88]. Laminar flame speeds were validated for pressures from 0.3 atm to 25 atm. Most laminar flame speed measurements were performed at room temperature (291–298 K), with some data points at 365 K and 393 K, which is limited; however, elevated pressure and temperature conditions were also evaluated. Interestingly, the reaction mechanism developed by Keromnes et al. was again found to perform the best. To further investigate, laminar flame speeds are computed using several mechanisms under the targeted temperature and pressure conditions. The mechanisms developed by Burke et al. [91], Hong et al. [92], San Diego [93], and Keromnes were included in both [88, 90], while the Li mechanism [94] is only included in [88]. The C3MECH mechanism [95] was not included in the previous comparisons; however, it includes validated S_L data for temperatures up to 600 K and pressures up to 10 atm. Similarly, the mechanism constructed by Boivin [96] reports validation over a broad range of temperatures and pressures. The Z79 mechanism is used for the atmospheric SBES simulations and is therefore also included.

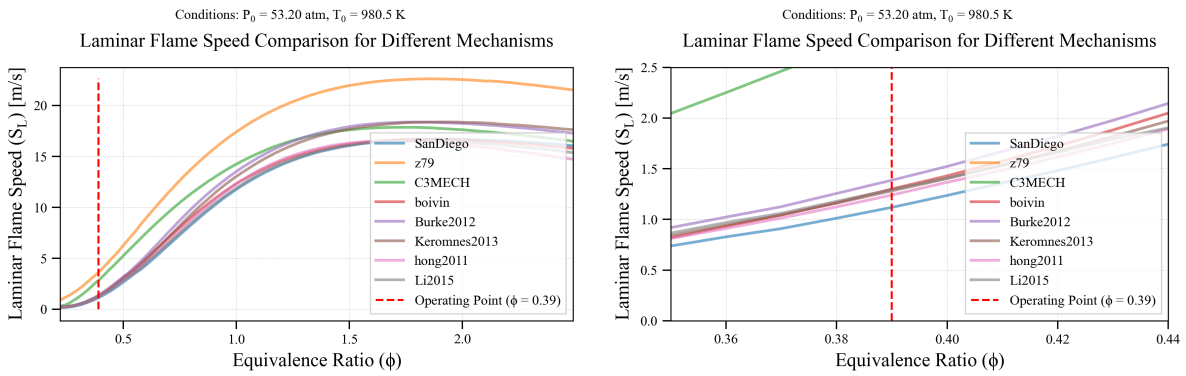

(a) Laminar flame speeds

(b) Laminar flame speed around operating point

Figure 6.7: Laminar flame speeds of hydrogen flames determined with various reaction mechanisms

In Figure 6.7a, the S_L values are reported for various equivalence ratios and mechanisms, obtained from Cantera 1D freely propagating flame simulations. It can be observed that the Z79 mechanism deviates, as it is not specif-

ically a hydrogen mechanism. In the topology analysis, it was concluded that most of the power is generated near the global equivalence ratio; this is not expected to be different under engine operating conditions. The S_L around the operating point, determined earlier (see Table 6.4), is therefore most critical, and Figure 6.7b shows a clearer view around this point. The C3MECH mechanism deviates and will therefore not be further considered. Zooming in further, it becomes apparent that the San Diego and Burke et al. mechanisms also deviate, underpredicting and overpredicting S_L, respectively. Furthermore, San Diego and Burke et al. are ranked lower in the comparison studies than Li et al., Hong et al., and Keromnes et al., while Boivin also predicts similar S_L values. The differences between the Li et al., Keromnes et al., and the Boivin mechanisms are negligible around the operating point, while Hong et al. shows a minor deviation. The Keromnes et al. mechanism has been chosen as it shows agreement among the highest-ranking reaction mechanisms for hydrogen combustion, and it is regarded as the most optimal by both [88, 90]. From the chemical kinetic mechanism of Keromnes et al., one-dimensional counterflow premixed flame solutions are generated and subsequently tabulated to construct a FGM. This manifold is then employed as turbulent combustion modeling framework to provide thermochemical state for the CFD simulations.

6.6. Overview of Simulations, Assumptions, and Limitations

The present section provides an overview of the simulations with their assumptions and limitations. Two tables are included: Table 6.5, which consists of two columns. The first column defines a tag that groups the associated assumptions and limitations listed in the second column. These tags are subsequently used in Table 6.6. This second table presents a simulation matrix providing an overview of the simulations and their corresponding assumptions/limitations, thereby offering a clear overview of the modeling framework.

The ”General” tag considers assumptions that are applicable across all simulations and cannot be attributed to a specific model or methodology. The ”Z79 mechanism” and ”Keromnes mechanism” tags contain assumptions related to the chemical kinetics, thermodynamic properties, and transport properties used to represent the reacting mixtures. The assumptions and limitations associated with the combustion and turbulence modeling approaches are grouped under the corresponding ”FGM-RANS” and ”SBES-TFM” tags. A distinction is made between the ”Spray modeling” and ”Spray BCs” tags, the former refers to assumptions associated with the physical sub-models used to represent spray behavior in the flow, whereas the latter concerns the boundary-condition specifications used to define the spray inlet conditions. Finally, the ”CHT” tag contains assumptions associated with the conjugate heat transfer simulations, for which the treatment of surfaces differs from that employed in the other simulations and additional (solid) domains are considered.

Table 6.5: Consolidated modeling assumptions and limitations across all sub-models

Tag	**Assumption / Limitation**
General	The inlet turbulence intensity of all input streams is considered to be 5%.
General	Wall surface roughness is not considered in the model and is therefore treated as hydraulically smooth.
General	The solution is assumed to be independent of the mesh, with no significant numerical errors arising from mesh resolution. The mesh quality is therefore considered sufficient, with further assessment provided in Appendix A.
Z79 mechanism	The reduced Z79 mechanism is assumed sufficient to reproduce the dominant combustion behaviour of hydrogen–kerosene mixtures.
Z79 mechanism	Thermochemical and transport properties derived from the Z79 mechanism are assumed to provide an accurate representation of the reacting flow physics within the range of operating conditions considered.
Z79 mechanism	Liquid kerosene is represented by a single surrogate species ($C_{11}H_{22}$), which is assumed to capture the dominant thermochemical behaviour of Jet-A fuel. [20]

Tag	Assumption / Limitation
Keromnes mechanism	The Keromnes hydrogen oxidation mechanism is assumed to accurately reproduce hydrogen combustion chemistry under engine-relevant conditions (P = 53.2 atm, T = 980.5 K).
Keromnes mechanism	Thermochemical and transport properties derived from the Keromnes mechanism are assumed to provide a sufficiently accurate representation of hydrogen oxidation kinetics across the relevant operating range.
SBES-TFM	The limitations associated with the k–ω SST turbulence model are confined to the near-wall regions of the computational domain. [72]
SBES-TFM	The limitations associated with the WALE subgrid-scale model are confined to regions away from the wall, where LES treatment is applied. [72]
SBES-TFM	The physical flame is artificially thickened to ensure that it is numerically resolved on the computational mesh.
SBES-TFM	Efficiency function assumed to compensate for unresolved flame wrinkling caused by thickening. [79]
SBES-TFM	Charlette flame wrinkling model used to estimate unresolved flame surface area. [79]
SBES-TFM	Thickened flame representation assumed not to modify global flame structure when corrected by the efficiency function and flame speed. [79]
SBES-TFM	The hydrogen fraction (α) is retrieved under the assumption of a unity Lewis number; however, the governing equations do not rely on this assumption.
SBES-TFM	A representative S_L and δ_l can be obtained from freely propagating premixed flame simulations in CANTERA for 3D turbulent, partially premixed kerosene–hydrogen blended flames using the Z79 mechanism.
RANS-FGM	The limitations associated with the k–ω SST turbulence model are applicable. [72]
RANS-FGM	Turbulent reactive structures are assumed to remain locally flamelet-like, such that the thermo-chemical state can be represented by laminar flame structures. [97]
RANS-FGM	The manifold is generated from 1D laminar flamelets: counterflow diffusion flames for HPS = 0.0% and premixed flames for HPS = 100.0%.
RANS-FGM	Flamelets are computed at a user-specified constant pressure (e.g., ambient or representative engine operating pressure); therefore, pressure-induced variations in species composition and temperature are not accounted for within the flamelet solutions.
RANS-FGM	The thermo-chemical state is parameterized using reduced scalar variables: mixture fraction Z and reaction progress variable c, along with their statistical variances (e.g. Z''^2).
RANS-FGM	For HPS=0.0%, the progress variable is defined based on pure CO_2, whereas for HPS = 100.0%, a definition based on pure H_2O is used.
RANS-FGM	Turbulence–chemistry interactions are modeled using a presumed PDF (Probability Density Function) approach in Z–c space, with mean properties obtained via integration over the flamelet manifold.

Tag	Assumption / Limitation
RANS-FGM	For HPS=0.0%, an appropriate scalar dissipation value is selected under ambient conditions.
Spray modeling	Liquid fuel represented using a Lagrangian discrete phase model. [82]
Spray modeling	Primary break-up is not resolved directly and is represented through prescribed injector parameters.
Spray modeling	Rosin-Rammler distribution is used to represent droplet size statistics.
Spray modeling	Sauter Mean Diameter is retrieved through the Lefebvre correlation [24].
Spray modeling	The droplet dynamics is accurately captured using the method proposed by [82].
Spray modeling	Secondary Break-up is consistent with the modeling approach of [83].
Spray modeling	Classical droplet heat-transfer correlations are assumed to be valid [84].
Spray modeling	The classical droplet evaporation model is assumed to be valid [84].
Spray modeling	The spray is assumed to operate at rated mass flow, producing a 60° cone angle directly downstream of the atomizer
Spray modeling	Internal atomizer flow is not resolved.
Spray BCs	Injector type spray is represented using a solid-cone injector model (baseline case).
Spray BCs	Spray spread parameter is fixed at $q = 3$.
Spray BCs	Droplet injection velocity is 20 ms^{-1}.
Spray BCs	The spray is assumed not to contain any swirl.
CHT	Material properties Stainless-steel thermal conductivity assumed constant at 16.27 $\mathrm{W\,m^{-1}\,K^{-1}}$.
CHT	Thermal contact conductance was estimated using literature-based correlations, accounting for the predicted contact pressure, surface roughness, and material temperature [86].
CHT	Horizontal solid-solid interfaces are assumed to be thermally connected through prescribed TCR values.
CHT	Vertical interfaces are assumed to be thermally disconnected ($\dot{q} = 0$).
CHT	Quartz sections are assumed to be thermally disconnected due to the sealing layer ($\dot{q} = 0$).
CHT	Natural convection imposed on external surfaces.
CHT	Constant heat-transfer coefficient of 5 $\mathrm{W\,m^{-2}\,K^{-1}}$ assumed for natural convection of external cooling.
CHT	Ambient temperature fixed at 293.15 K.
CHT	Atomizer, plenums, ducts, swirler and orifice are assumed adiabatic surfaces.
CHT	Radiative heat transfer is neglected.
Adiabatic walls	All walls are treated as adiabatic ($\dot{q} = 0$).

Table 6.6 provides an overview of the simulations with their associated assumptions and limitations based on the previously defined tags. As discussed previously, the assumptions grouped under the ”General” tag apply to

all simulations. The ”Z79 mechanism” is employed for all the cases except the ”Engine Operating Conditions” case, for which the ”Keromnes mechanism” is used instead due to its dedicated representation of H_2 combustion chemistry. The assumptions and limitations associated with the ”SBES-TFM” tag apply exclusively to the High-Fidelity SBES Simulation, which is considered the reference case. In contrast, the remaining simulations employ the ”FGM-RANS” approach and are therefore subjected to its associated assumptions and reduced accuracy. The assumptions associated with the ”Spray modeling” apply to all simulations involving spray injection. Conversely, the dedicated Spray Boundary Condition simulations are designed to assess the sensitivity of the results to the prescribed spray boundary conditions. As a result, the assumptions grouped under the ”Spray BCs” tag are not applicable to these simulations. Finally, the assumptions and limitations grouped under the ”CHT” tag apply only to the Conjugate Heat Transfer simulations. Consequently, the adiabatic wall assumption used in the other simulation cases is no longer applicable, as heat transfer through the solid domains is explicitly resolved.

Table 6.6: Applicability of modeling assumptions to the simulation cases

Tag	**High-Fidelity SBES**	**Spray Sensitivity**	**Conjugate Heat Transfer**	**Engine Conditions**
General	✓	✓	✓	✓
Z79 mechanism	✓	✓	✓	–
Keromnes mechanism	–	–	–	✓
SBES-TFM	✓	–	–	–
RANS-FGM	–	✓	✓	✓
Spray model	✓	✓	✓	–
Spray BCs	✓	–	✓	–
CHT	–	–	✓	–
Adiabatic walls	✓	✓	–	✓

Two additional SBES simulations are performed that are not included in the overview. Their objective is to investigate specific model sensitivities. The first examines the influence of imposing non-adiabatic wall boundary conditions within the SBES framework, as further detailed in subsection 7.3.1. The second evaluates the impact of an alternative spray initialization strategy within the SBES setup, which is further discussed in subsection 7.3.2.

7

Simulation Results

This chapter presents the results of the simulations detailed in the previous section. First, the high-fidelity SBES simulation is examined, and its agreement with the experimental data is assessed. This assessment is followed by a flame topology analysis to further understand the characteristics of the H_2-kerosene blended flames. The discussion then explores improvements to the high-fidelity SBES model using RANS simulations. Finally, the chapter extends the discussion to engine operating conditions, providing guidance for the future development of the HOPE combustor.

7.1. Comparison Against Experiments at Atmospheric Pressure

The high-fidelity SBES agreement with the experiments is evaluated in terms of flame shape, providing a comparison of the overall flame structure. Subsequently, the agreement is assessed for the spray, with a focus on the spray angle.

7.1.1. Flame Agreement with Experiments

The results of the high-fidelity SBES simulations are discussed in this section, comparing the heat release rate (HRR) from CFD with the experimental OH* chemiluminescence for selected HPS_g values. Comparison of the OH* and HRR for CFD-EXP agreement is well established in literature. [98]. However, in multi-fuel conditions, some additional considerations must be taken into account. The response of the heat release rate and HPS at stoichiometric conditions has been simulated using freely propagating flames in CANTERA [77]. The OH* sub-mechanism [99] was merged into the CRECK reaction mechanism for n-dodecane [100], which was preferred over the Z79 because it already contained all the precursor species needed for OH* formation. This enabled plotting of the OH* response, as this pathway is not originally included in the Z79 mechanism. The responses are shown in Figure 7.1. It becomes evident that, although the peak heat release rate (HRR) of hydrogen is approximately three times higher than that of kerosene, the OH* mass fraction does not follow the same trend and is nearly an order of magnitude lower in the hydrogen case. The OH* signal is therefore more responsive to kerosene than to hydrogen. This will create a mismatch between experiments and CFD, because experiments will mostly show the parts of the flame fueled by kerosene, whereas hydrogen parts will produce less OH*, leading to an underrepresentation of hydrogen in the signal. Furthermore, the OH* signal of hydrogen exhibits a spatial lag with respect to its HRR, appearing slightly downstream of the corresponding heat release zone.

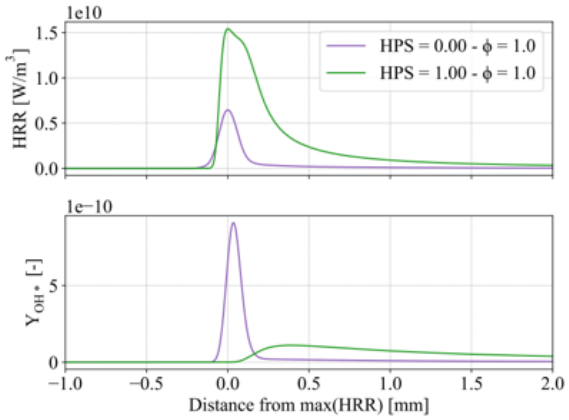

Figure 7.1: The OH* response to the heat release rate location for both kerosene and hydrogen [77]

The average normalized OH* experimental data and the averaged normalized HRR retrieved from the simulation are exhibited side by side for the selected HPS_g settings in Figure 7.2. The experimental OH* signal is obtained through an Abel inversion to reveal the inner structure of the flame, allowing the comparison against contours of the CFD-data. The experimental data are retrieved from [54].

Considering the HPS_g=0.0% and HPS_g=30.0% cases, the experimental result reports similar characteristics, a spray stabilized flame, anchoring in the inner and outer shear layer. The atomization in this region is effective; however, the estimated SMD increases from 13.6μm to 18.44 μm between the two HPS_g cases. Therefore, the spray quality of the HPS_g=30.0% deteriorates; hence, the droplets take longer to evaporate, causing the increase in LoH (Lift-Off Height). Although the addition of H_2 has the potential to intensify the combustion process, the observed increase in LoH indicates that the deterioration in spray characteristics is the dominant effect. Furthermore, the influence of H_2 on the flame structure is negligible, as the overall flame shape remains largely unchanged. The lean hydrogen mixture is not able to sustain combustion independently, and the flammability limits are therefore not yet exceeded for hydrogen alone. As a result, combustion occurs predominantly within the existing kerosene-dominated flame regions.

Considering the simulation results of HPS_g=0.0%, a similar flame structure is found with the flame anchoring in the inner and outer shear layer, inline with the experiments. However, in the simulation, the flame extends downwards to the central part of the burner (around x = 0.0 mm), and HRR is present in the center, which is not found in the experiments. The discrepancy in the central flame between the CFD and experiments may be attributed to discrepancies in the simulated spray boundary conditions or fuel heating and evaporation characteristics. Alternatively, it may arise from limitations of the Abel inversion near the centerline, which can lead to an underrepresentation of the inner flame. In CFD simulations, the flame also extends slightly further toward the quartz surface compared to the experiments.

For the HPS_g=30.0% case, an additional structure is observed, as it can be seen that, besides the original CFD flame structure of HPS_g=0.0%, a second flame region is formed, appearing at the edges of the mixing tube outlet (located at x = 10 mm and x = -10 mm at y = 0 mm). This second region might be caused by the premature prediction of independent hydrogen oxidation not occurring in the experiments. However, even without considering this upstream region, the HRR along the central axis is anchoring too far upstream for the LoH to match between the experiments and the simulation, as this central flame is still present.

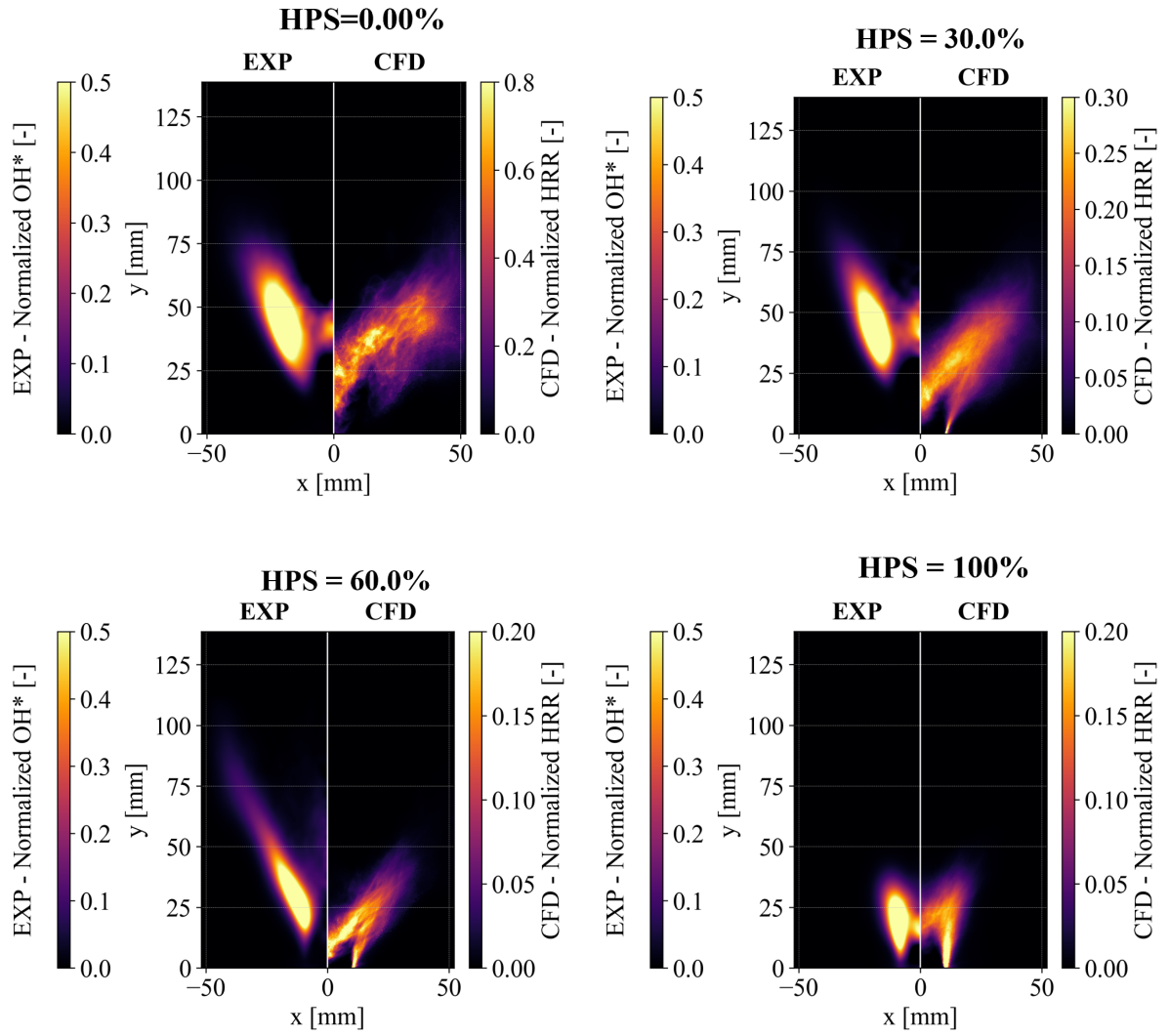

Figure 7.2: Agreement for different HPS_g levels (0%, 30%, 60%, and 100%), comparing the averaged CFD-HRR with the averaged EXP-OH*

The experimental result of the HPS_g=60.0% shows a shift towards a slightly more elongated V-shape, while the LoH is significantly decreased. The elongation of the flame lobes might be due to the deterioration of the spray, since larger droplets enter the domain, requiring a longer residence time to evaporate, thereby elongating the flame. Simultaneously, the addition of H_2 increases the reactivity, resulting in an upstream stabilization of the flame; a tendency to reach the edge of the mixing tube can be observed. Considering the simulation results, HPS_g=60.0% provides the same structure as HPS_g=30.0%, however, the attached flame shortens as a result of the increased reactivity due to H_2 addition. The HRR near the edges of the mixing tube can again be observed and is also intensified.

Referring to the experimental result at $HPS_g = 100\%$, the flame shortens into a lean-premixed M-shaped structure, anchored at the edges of the mixing tube exit. The inner region of the M-flame is sustained by the inner shear layer, which stabilizes part of the H_2 flame along the axis. A small discontinuity is observed in this inner flame region, which may be attributed to artifacts introduced by the Abel inversion. The CFD results show satisfactory agreement in this case, as the experiments confirm that hydrogen combusts directly upon leaving the mixing tube exit, consistent with the CFD predictions.

A quantitative comparison between experimental data and simulations is performed by evaluating the Lift-off

Height (LoH) and the Flame Height (FH). In the simulations, the heat release rate (HRR) is utilized to determine both quantities. Flame regions are identified by applying a threshold based on a percentage of the maximum heat release rate, HRR_{max}. Regions exceeding the selected threshold are classified as part of the flame. The LoH is then defined as the most upstream axial location identified as part of the flame, while the FH is defined as the axial extent of the flame, determined as the distance between the most downstream and most upstream flame locations. The choice of threshold remains somewhat arbitrary, as no universally accepted definition is available in the literature. In the present work, thresholds corresponding to 15% and 99% of HRR_{max} are considered. The experimental LoH and FH values are retrieved from [54]. In the experiments, both quantities are determined from OH*/CH* fields obtained through Abel-inverted intensity distributions using the 5% iso-intensity contour threshold of the normalized Abel fields.

Considering the LoH, the trend with increasing HPS_g cannot be captured, as the predicted LoH collapses to just below the mixing tube exit for all $HPS_g > 0.0\%$, for both the 15% and 99% thresholds, as well as for all other tested threshold values. This is attributed to hydrogen oxidation being predicted too far upstream, generating the upstream heat release zone discussed in Figure 7.2. As a result, significant heat release is present near the swirler exit across all threshold levels, including the 99% contour. Consequently, the analysis presented by [54], in which the initial deterioration of the droplet spray increases the LoH, cannot be reproduced. In the experimental analysis of [54], the CH* and OH* responses diverge around HPS_g=60.0%, where the CH* response initially increases again around HPS_g=50%, while the OH* response decreases monotonically, reflecting the competing influence of deteriorating atomization and hydrogen-induced reactivity in this region. Nevertheless, the CFD is unable to capture this interaction, as premature flame anchoring is predicted.

Now, considering the FH, for HPS_g>0.0%, the LoH is approximately zero; hence, the variation in FH is entirely governed by the extent of the flame tip. Two distinct branches emerge depending on the chosen HRR threshold. For the high-threshold branch represented by the 99% contour, the FH collapses to near 0 mm for HPS_g> 0.0%, which is again attributed to the intense upstream HRR region present for $HPS_g > 0.0\%$. In the low-threshold branch represented by the 15%-line, the kerosene flame is also included in the identified flame region, and no such collapse is observed. In this case, the FH decreases monotonically with increasing HPS_g, as hydrogen addition reduces the overall flame length.

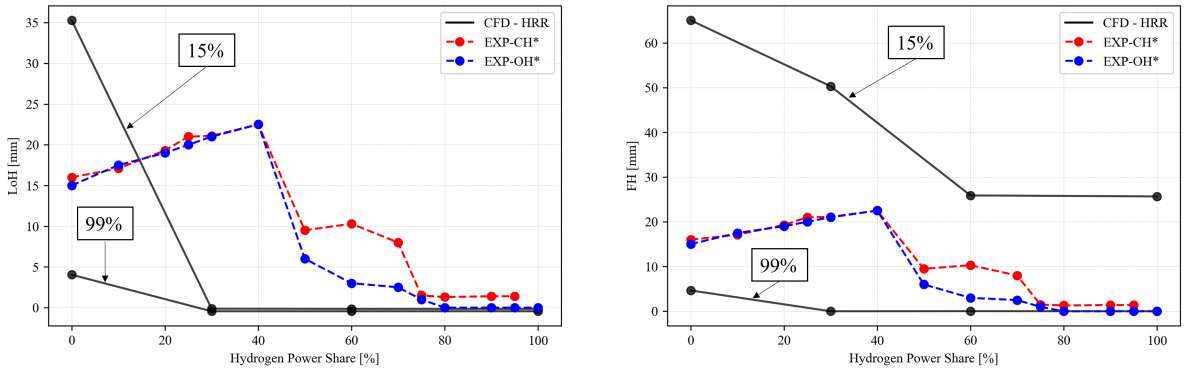

(a) Variation on the LoH for the full range of hydrogen-kerosene blends

(b) Variation on the FH for the full range of hydrogen-kerosene blends

Figure 7.3: Comparison of simulated and experimental lift-off height (LoH) and flame height (FH). In the CFD results, LoH and FH are defined using the HRR/HRR_{max} iso-intensity contours at 15% and 99.0%, respectively, while the experimental values are based on the 5% iso-intensity contour of the normalized Abel-inverted OH* and CH* fields reported in [54]

For the low-threshold branch (HRR/$HRR_{max} \leq 14\%$), the analysis of the LoH and FH again shows that a major discrepancy between the experiments and the CFD originates from upstream hydrogen oxidation. This is further illustrated in Figure 7.4, which shows the region with $HRR > 1\times10^7$, Wm^{-3} for the $HPS_g = 30\%$ case, which was selected as the multi-fuel case with the lowest hydrogen content. The first sub-figure presents a perspective view, revealing two distinct flame structures: a broad, lifted V-shaped ring flame, and a second, significantly shorter structure anchored at the swirler outlet corners and extending around its circumference. A clearer view of this upstream structure is obtained by zooming into the region indicated in the middle sub-figure, as shown in the rightmost sub-figure.

It can be observed that the upstream flame structure appears considerably more intense than the lifted V-shaped

flame. This is attributed to the nature of hydrogen combustion: hydrogen burns directly at the mixing tube exit, where its high laminar flame speed and adiabatic flame temperature lead to a spatially compact but highly intense reaction zone, resulting in significantly higher HRR compared to kerosene. This upstream oxidation is not observed in the experiments and is therefore identified as the most significant discrepancy between the experimental observations and the simulations.

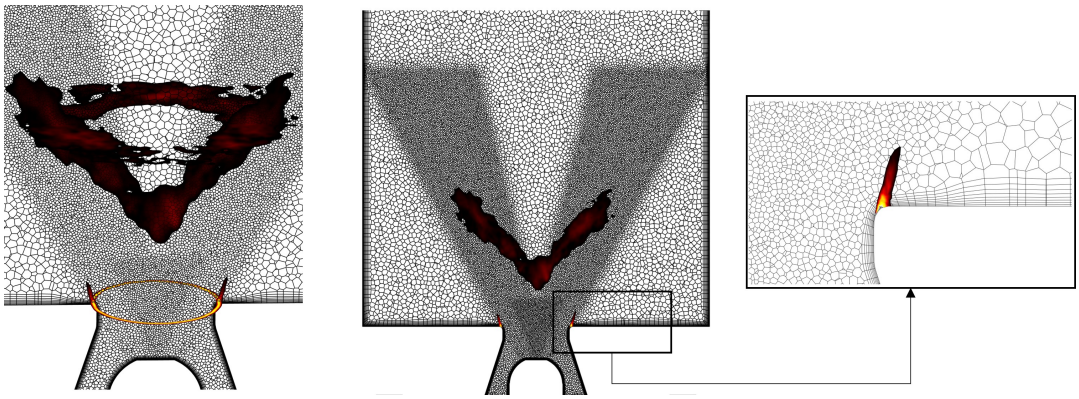

Figure 7.4: Identified high HRR-zones at HPS_g=30.0%, showing HRR > 1e+07 Wm^{-3} consisting of two structures, a V-shaped lifted kerosene flame and an attached short hydrogen flame

7.1.2. Comparison of the Spray Cone Angle

The cone spray angle cannot be determined from the CFD results in the same manner as in the experiments, as different data sources are available. Furthermore, the experimental cone angle depends on the chosen signal-to-noise ratio (SNR) and axial position [54], making a direct comparison unattainable. Therefore, a normalization is used, the variation of the cone angle with HPS_g is compared for CFD and experiment. In the CFD, the cone angle is determined from the spray volume fraction iso-lines at 10^{-4}, 10^{-6}, and 10^{-8}. Tangent lines are drawn to each isoline, and the angle between these tangent lines represents the corresponding cone angle. A lower isoline value results in a larger cone angle, as it captures the outer periphery of the spray.

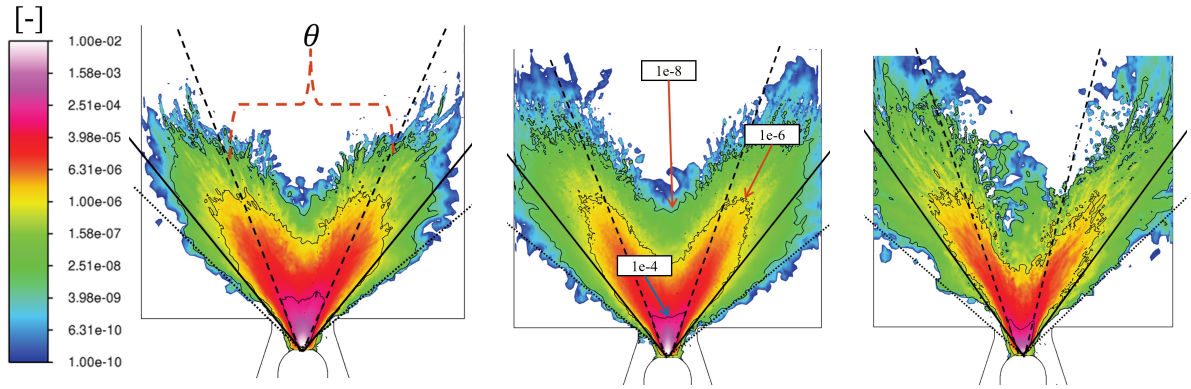

(a) HPS_g=0.0% **(b)** HPS_g=30.0% **(c)** HPS_g=60.0%

Figure 7.5: Liquid volume fraction field [-] retrieved from simulations, along with the method used to determine the spray angle based on iso-lines at 10^{-4}, 10^{-6}, and 10^{-8}, annotated in the HPS_g=30.0% contour

Before discussing the results, it must be noted that the internal geometry of the atomizer and the primary breakup process are not resolved in the simulations. Furthermore, it is assumed that the atomizer operates under rated conditions for all cases, independent of the mass flow rate through the injector.

In Figure 7.5, the resulting spray angles obtained from the three iso-lines are presented, together with their variation as a function of HPS_g. The experimentally measured spray angle is also included for comparison. The experimentally observed cone angle falls between the 10^{-4} and 10^{-6} iso-lines, suggesting that a 10^{-5} iso-line

would correspond most closely to the experimental data. Both the 10^{-4} and 10^{-6} based angles show a decreasing cone angle with increasing HPS_g, while the 10^{-8} iso-line is too low to capture the trend.

For HPS_g < 30%, satisfactory agreement is found between CFD and experiments. Nevertheless, the peak observed around HPS_g= 20.0% cannot be captured, as this operating point is not included in the CFD dataset; moreover, it may represent an outlier in the experimental results. For 30% < HPS < 40%, general conclusions are difficult to draw, as only the HPS_g= 30% and HPS_g=60% cases are available in the CFD results. For HPS_g>40%, the experimentally observed increase in cone angle is not reproduced.

The initial reduction in cone angle can be explained by the reduced pressure drop across the atomizer. In the experiments, an increase in cone angle is observed from approximately HPS_g=40.0%, which is associated with upstream flame propagation stabilizing near the mixing tube outlet [54]. The resulting thermal expansion induced by this upstream flame location likely enhances radial spray dispersion by exerting an outward momentum on the droplets. In the CFD results, however, the flame is already anchored at the mixing tube exit for HPS_g=30.0%. This anchoring may limit radial spray development, as the predominantly axially oriented flame introduces a momentum component that counteracts radial spreading.

In CFD simulations, the initial reduction in cone angle is attributed to an increase in droplet diameter, since the initial cone angle is prescribed under the assumption that the atomizer operates at its rated mass flow rate, $\dot{m}_{rated}$. In the experiments, however, the early-stage decrease in cone angle may result from operating the atomizer at a non-rated $\dot{m}$, as well as from interactions of larger droplets. The subsequent experimentally observed increase in cone angle cannot be reproduced numerically, as in the simulations the flame is already anchored at the mixing tube exit, limiting further evolution of the spray structure.

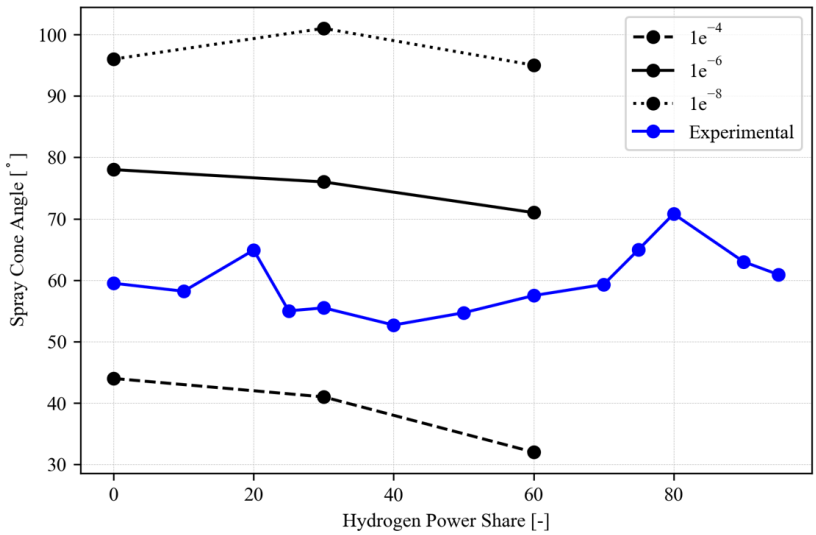

Figure 7.6: Absolute spray characteristics predicted from simulations, compared with experimental values across the full range of HPS_g cases

7.2. Flame Topology Analysis

The flame topology analysis starts with a discussion of the flame sensor, as adjustments had to be implemented for the successful deployment of the TFM. Thereafter, the flow-field contours are discussed. Subsequently, a quantitative analysis is performed utilizing the flexibility of the CFD data.

7.2.1. Improvement of the Flame Sensor

The desired properties of the flame sensors has been formulated by [101]. It must correctly encompass the source terms of the reaction zone. It must correctly encompass the density/temperature gradients on the cold side, preventing numerical issues. In the post-flame region, it should rapidly vanish to avoid thickening.

The initial simulations indicated that the flame sensor required modification, as the default sensor available in

ANSYS Fluent—based on the sum of all reaction rates—failed to correctly detect the flame front, as shown in Figure 7.7. The heat release rate (left) provides an approximate indication of the flame location; for reference, an iso-contour of the heat release rate (HRR=1e+7 Wm^3) is included in the middle and right plots. The middle contour shows the flame sensor (S) varying between zero and unity, while the right contour represents the effective thickening (F_{eff}) of the region.

From this comparison, it becomes evident that the flame is not properly captured by the current sensor definition. Only small isolated regions are identified as flame zones, resulting in insufficient flame thickening. Consequently, alternative flame sensor formulations were investigated.

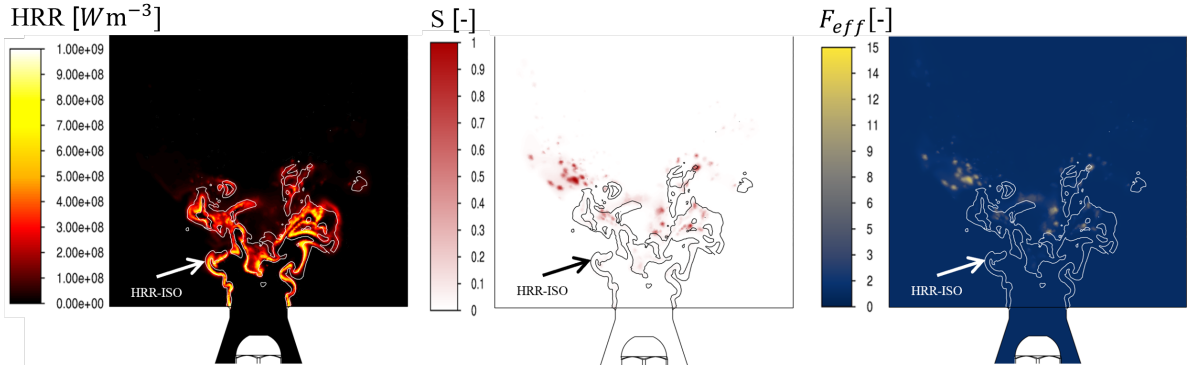

Figure 7.7: Flame sensor with Ω defined based on all reaction rates in the reaction mechanism for atmospheric conditions and HPS_g=60.0%. From left to right: the heat release rate (HRR), the flame sensor (S), and the resulting thickening factor (F_{eff}). The HRR-ISO value is 1×10^7, W, m^{-3}.

However, the definition of Ω (the flame sensor variable in Equation 5.27) can be based on different quantities. In ANSYS FLUENT, the flame sensor Ω can only be defined in a straightforward manner using the reaction rates of reactions included in the chemical mechanism (here the Z79 reaction mechanism, which will be used throughout this work). The flame sensor must perform consistently for pure kerosene, dual-fuel operation, and pure H_2. In the latter case, no carbon is present and therefore any reactions involving carbon cannot be used. As a result, only 19 of the 79 reactions in the Z79 mechanism remain applicable. These reactions were tested in CANTERA using freely propagating flames for HPS_g=0.0%, HPS_g=60.0%, and HPS_g=100.0%. This procedure reduced the selection to only a few candidate reactions. The corresponding sensor definitions were then implemented in the HPS_g=60.0% case to evaluate their performance in the CFD simulations. Ultimately, it was found that the reaction $OH + HO_2 \rightarrow O_2 + H_2O$ provided the most robust performance within this set of definitions (with $\beta = 5$). Figure 7.8 shows the flame sensor characteristics obtained when Ω is based on this reaction, corresponding to the same case as in Figure 7.7.

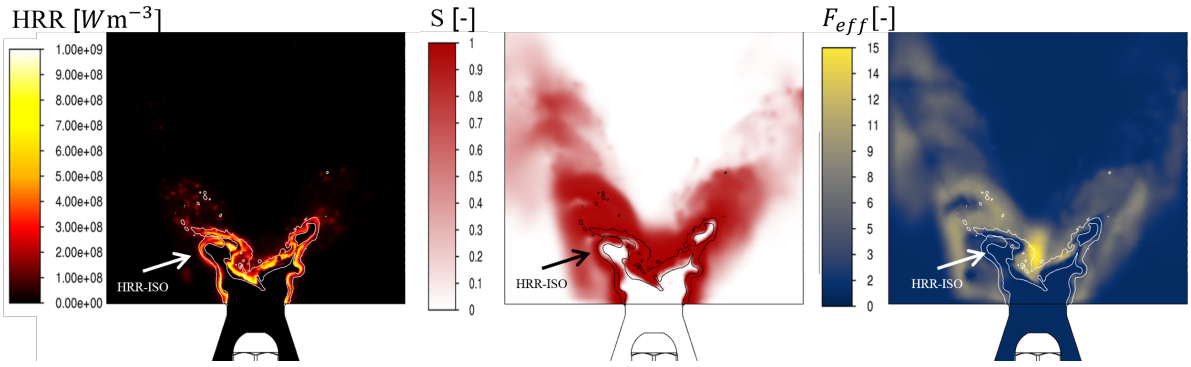

Figure 7.8: Flame sensor with Ω defined based on $OH + HO_2 \rightarrow O_2 + H_2$ for atmospheric conditions and HPS = 60.0%. From left to right: the heat release rate (HRR), the flame sensor (S), and the resulting thickening factor (F_{eff}). The HRR-ISO value is 1×10^7, W, m^{-3}.

The current definition based on the reaction $OH + HO_2 \rightarrow O_2 + H_2O$ appears to correctly capture the reaction zone, while no numerical difficulties are observed on the cold-flow side. However, significant thickening may

still be applied outside the actual flame region. Several alternative flame sensor definitions have been proposed in the literature [101, 102, 103], including advanced techniques that allow for self-adaptive thickening [104]. An interesting approach for multi-fuel applications is the method proposed by [66], in which the oxidizer source term is used to define Ω. This may provide a robust option for multi-fuel operation. In addition, Ω_0 is dynamically varied based on the local mixture conditions.

7.2.2. Flame Contours and Visualization

In Figure 7.9, the instantaneous contours of HRR are presented. The flame front of HPS$_g$=0.0% appears widespread, as the relatively wide droplet distribution causes a broad flame front. The evaporation process is spread due to the wide spray distributing the droplets over the whole region. The same broad distribution of the flame front can be found for the HPS$_g$=30.0%, however, in this case, the flame also propagates through the outer shear layer and attaches on the mixing tube edge. Although, for this specific instantaneous flame, the upstream attached flame appears relatively weak, as it is much more visible when examining the time-averaged field (see Figure 7.2). For HPS$_g$=60.0% the H_2 addition intensifies the combustion process shortening the flame, strengthening the attachment to the mixing tube outlet edge. In the pure H_2 case, combustion is further intensified; the reaction zone no longer spreads radially but instead propagates directly downstream from the mixing tube edges. This HRR region eventually interacts with the inner shear layer, causing the heat release rate to propagate towards the central axis of the combustor (x=0mm).

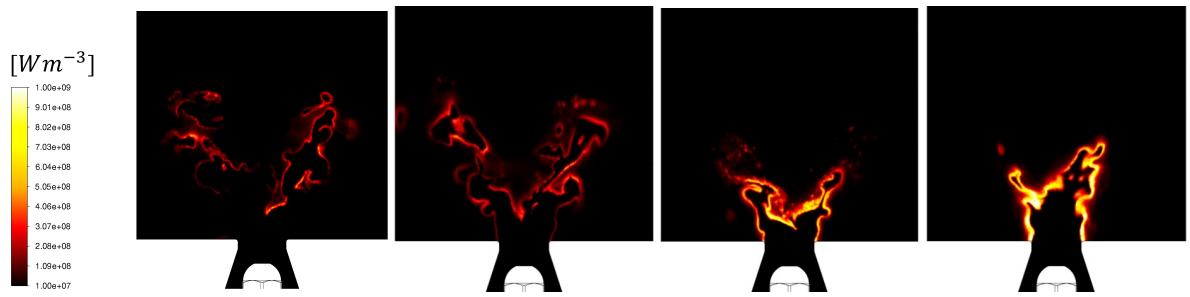

(a) HPS$_g$=0.0% **(b)** HPS$_g$=30.0% **(c)** HPS$_g$=60.0% **(d)** HPS$_g$=100.0%

Figure 7.9: Instantaneous Heat Release Rate for the selected HPS$_g$-cases

In Figure 7.10, the time-averaged mass fraction of $C_{11}H_{22}$ (the kerosene surrogate) is shown. As expected, the mass fraction decreases with increasing HPS$_g$, vanishing entirely for the pure H_2 case. The shape observed in the HRR contour at HPS$_g$=0.0% is also present in the $C_{11}H_{22}$ field and is a direct consequence of the evaporation and mixing/consumption characteristics. Transitioning to HPS$_g$=30.0%, the overall lobe length remains comparable to that of HPS$_g$=0.0%, suggesting that the increased reactivity of H_2 and the deteriorated spray largely balance each other, resulting in a negligible net effect on the evaporation process and the consumption of the kerosene surrogate. At HPS$_g$=60.0%, the $C_{11}H_{22}$ distribution shifts slightly downstream due to the further deterioration of the spray quality. However, the increased presence of H_2 intensifies the combustion process. This substantially enhances evaporation and likely promotes mixing of $C_{11}H_{22}$, resulting in faster fuel consumption and a shortening of the overall flame lobe length. Finally, at HPS$_g$=100.0%, the $C_{11}H_{22}$ mass fraction vanishes entirely, consistent with the absence of kerosene in the pure hydrogen case. It can further be observed that $C_{11}H_{22}$ is absent in the high-HRR zones located near the mixing tube corners in the dual-fuel cases, providing additional evidence of exclusive H_2 oxidation in this region.

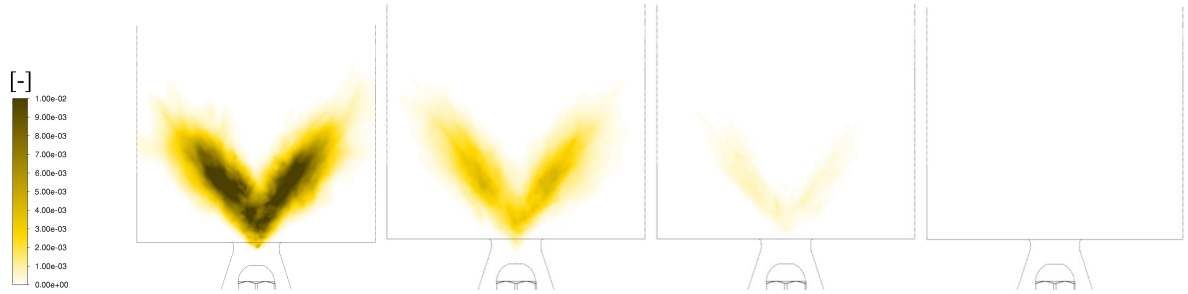

(a) HPS$_g$=0.0% **(b)** HPS$_g$=30.0% **(c)** HPS$_g$=60.0% **(d)** HPS$_g$=100.0%

Figure 7.10: Time-averaged mass fraction for the selected HPS$_g$-cases

The time-averaged axial velocity profiles for the selected cases are shown in Figure 7.11. The contours remain similar for all the HPS$_g$ cases with the exception for the pure H_2 case, where a noticeable increase in axial velocity is observed. This increase can be attributed to two effects. The first is that the overall mass flow increases due to the added H_2 mass flow. The second is that the axially oriented H_2 flames near the mixing tube exit push the flow in the axial direction. The increased axial velocity with HPS$_g$ forms part of the inherent flashback prevention mechanism.

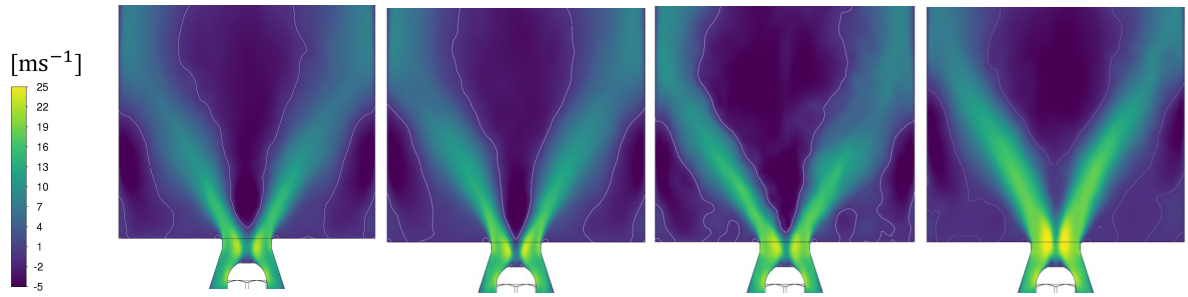

(a) HPS$_g$=0.0% **(b)** HPS$_g$=30.0% **(c)** HPS$_g$=60.0% **(d)** HPS$_g$=100.0%

Figure 7.11: Time-averaged axial velocity for the selected HPS$_g$-cases

The time-averaged temperature contours are reported in Figure 7.12. The V-shaped lobe structure is again observed. The distributions for HPS$_g$=0.0% and HPS$_g$=30.0% show similar contours, although the HPS$_g$=30.0% case is slightly shortened and narrowed. This trend continues toward HPS$_g$=60.0%. Finally, at HPS$_g$=100.0%, the lobes disappear entirely, consistent with the removal of the spray characteristics.

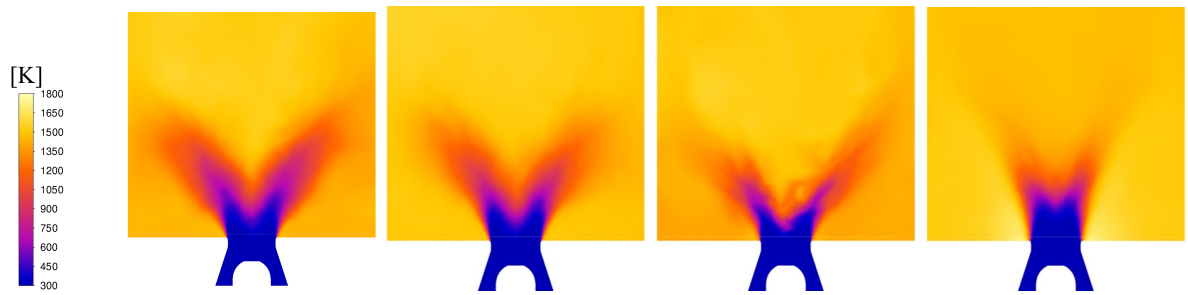

(a) HPS$_g$=0.0% **(b)** HPS$_g$=30.0% **(c)** HPS$_g$=60.0% **(d)** HPS$_g$=100.0%

Figure 7.12: Time-averaged temperature for the selected HPS$_g$-cases

To further understand the structure of the multi-fuel flame, several scalar fields are examined. For partially premixed H_2–kerosene flames, the local mixture composition and combustion mode are not uniform throughout the flow field, hence a more detailed analysis is performed. The first scalar to discuss is the progress variable c, which characterizes the local state of the reaction, ranging from zero in the unburnt mixture to unity in the fully

burnt products. It therefore provides insight into where combustion has occurred and how far the reaction has progressed. Several definitions of the progress variable exist, and their suitability depends on the flame characteristics and type [105]. Since H_2O is a common combustion product of both H_2 and kerosene, the progress variable is defined based on its production. In Figure 7.13, the mass fractions of H_2O (denoted as Y_{H_2O}) are shown for the selected cases. Approximately the same structures are identified in the Y_{H_2O} as in the HRR. Furthermore, Y_{H_2O} increases with increasing HPS_g. Although H_2O is a product of both fuels, it is more dominant in H_2 combustion, hence the post-flame Y_{H_2O} increases with HPS_g.

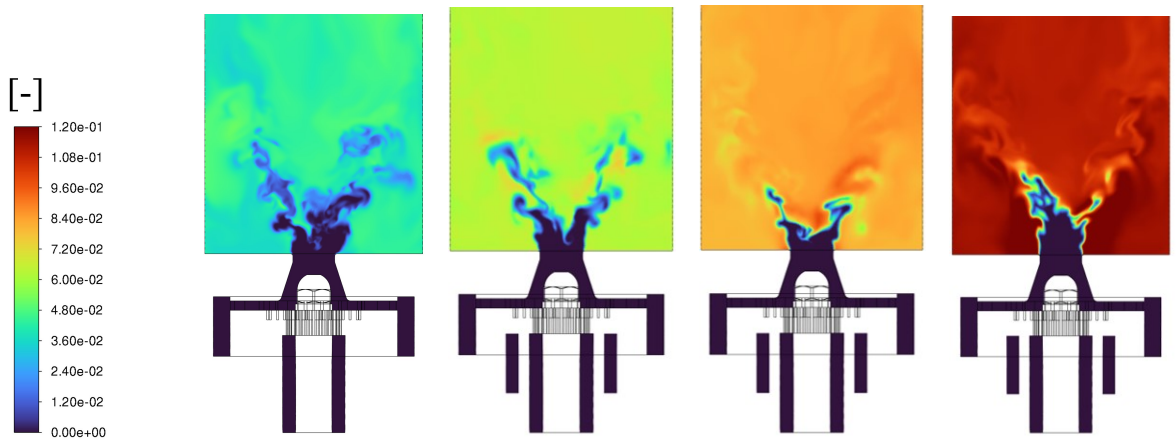

(a) HPS_g=0.0% **(b)** HPS_g=30.0% **(c)** HPS_g=60.0% **(d)** HPS_g=100.0%

Figure 7.13: The instantaneous mass-fraction of H_2O for the selected HPS_g-cases

The mass fraction of CO_2 or Y_{CO_2} is the other product of complete kerosene combustion and should therefore also be considered for the progress variable to capture kerosene specific trends. In Figure 7.14 it can be observed that the CO_2 exhibits a reverse trend of the H_2O as it becomes more dominant with decreasing HPS_g, eventually vanishing in the pure H_2 case.

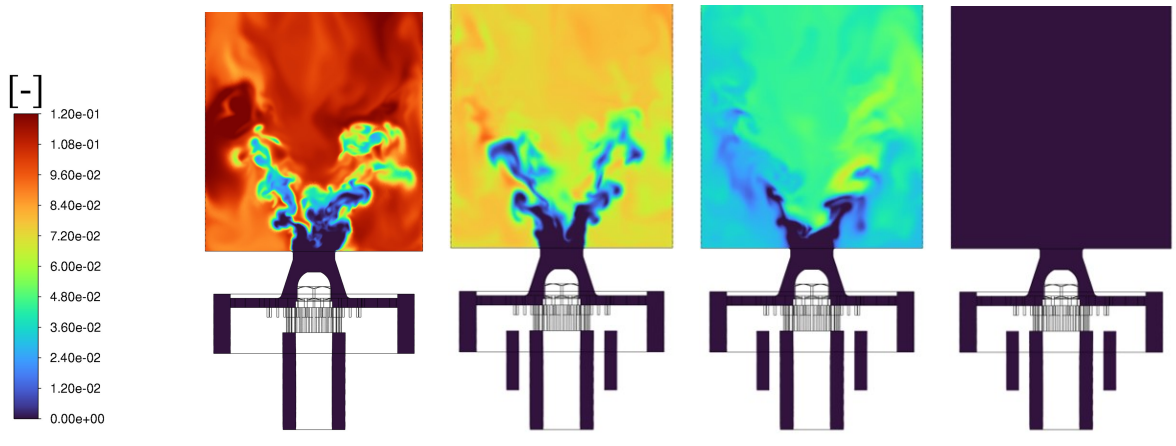

(a) HPS_g=0.0% **(b)** HPS_g=30.0% **(c)** HPS_g=60.0% **(d)** HPS_g=100.0%

Figure 7.14: The instantaneous mass-fraction of CO_2 for the selected HPS_g-cases

Note that the same scale has been used for both the Y_{H_2O} and Y_{CO_2}, revealing that they are of the same order of magnitude. Also, in the unburnt gas both CO_2 and H_2O are absent. The progress variable is hence defined as the ratio of the linear combination of Y_{CO_2} and Y_{H_2O} to their complete combustion state. The definition is suitable for dual kerosene–H_2 flames as the contribution of H_2O and CO_2 adjusts naturally to the HPS_g-case (completely H_2O-based for HPS_g=100.0% and more dominantly CO_2 for kerosene). The definition of the progress variable

is reported in Equation 7.1.

$$c = \frac{Y_{CO_2} + Y_{H_2O}}{Y_{H_2O,\text{complete}} + Y_{CO_2,\text{complete}}} \tag{7.1}$$

The mixture composition in multi-fuel partially premixed flames is continuously changing, in contrast to a premixed flame, for which a progress variable is native. Therefore, the complete combustion state should be determined from the local mixture properties, meaning that, for each cell in the domain, a dedicated value at complete combustion is computed. In this complete combustion state, all carbon atoms are converted to CO_2, and the same applies to H_2 being converted to H_2O. Retrieving Y_H and Y_C from the species transport equations allows determination of the complete combustion state using Equation 7.2.

$$\begin{aligned} Y_{H_2O} &= \frac{W_{H_2O}}{2\,W_H}\,Y_H \\ Y_{CO_2} &= \frac{W_{CO_2}}{W_C}\,Y_C \end{aligned} \tag{7.2}$$

Note that the assumption has been imposed that every H_2 and carbon atom completes its oxidation process, which is a valid assumption for the intended lean combustion regime of the design. The contours of the equilibrium states of Y_{H_2O} and Y_{CO_2} are reported in Figure 7.15 and 7.16, respectively. The denominator in the progress variable definition (Equation 7.1) scales naturally with the HPS_g setting as well. It can be observed that $Y_{H_2O_{complete}}$ is non-zero in the plenums due to the presence of unburnt H_2. The $Y_{H_2O_{complete}}$ decreases at the point of H_2 mixing with the swirling air. The $Y_{H_2O_{complete}}$ remains approximately constant through the mixing tube, increasing further due to $C_{11}H_{22}$ addition from the spray. In the HPS_g=0.0% case, $Y_{H_2O_{complete}}$ is only due to the spray and hence $Y_{H_2O_{complete}} = 0$ in the mixing tube. Although, for the HPS_g=100.0% case a further increase of $Y_{H_2O_{complete}}$ can be observed as H_2O accumulates in the IRZ and ORZ.

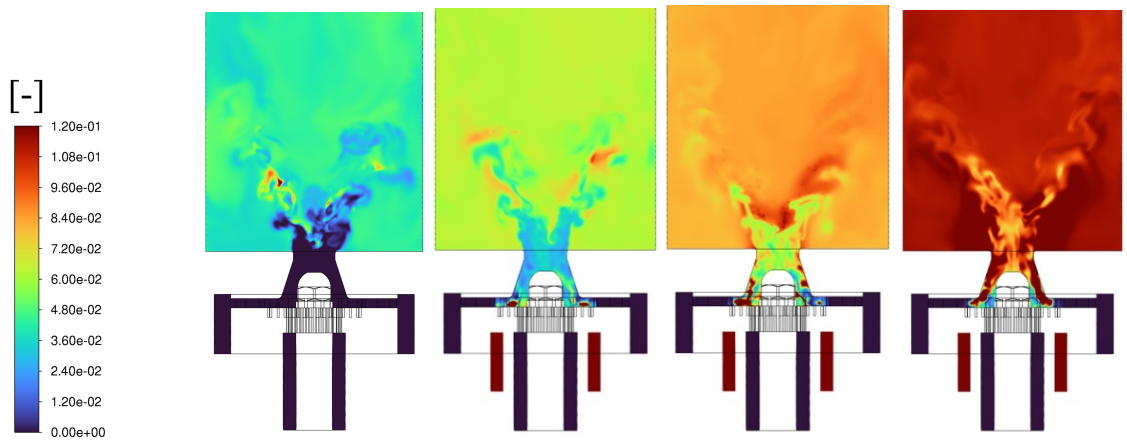

(a) HPS_g=0.0% **(b)** HPS_g=30.0% **(c)** HPS_g=60.0% **(d)** HPS_g=100.0%

Figure 7.15: The instantaneous equilibrium mass-fraction of H_2O for the selected HPS_g-cases

The $Y_{CO_2,\text{eq}}$ shows no contribution within the mixing tube, as carbon atoms are released directly in the chamber via the spray. For HPS_g=100.0%, the $Y_{CO_2,\text{eq}}$ vanishes entirely, consistent with the absence of carbon in the pure H_2 case. Local hotspots are observed due to carbon mixing and accumulation at the top of the flame, after which the mixture becomes more thoroughly mixed, converging towards a more homogeneous distribution. This pattern is also visible in the Y_{H_2O} field.

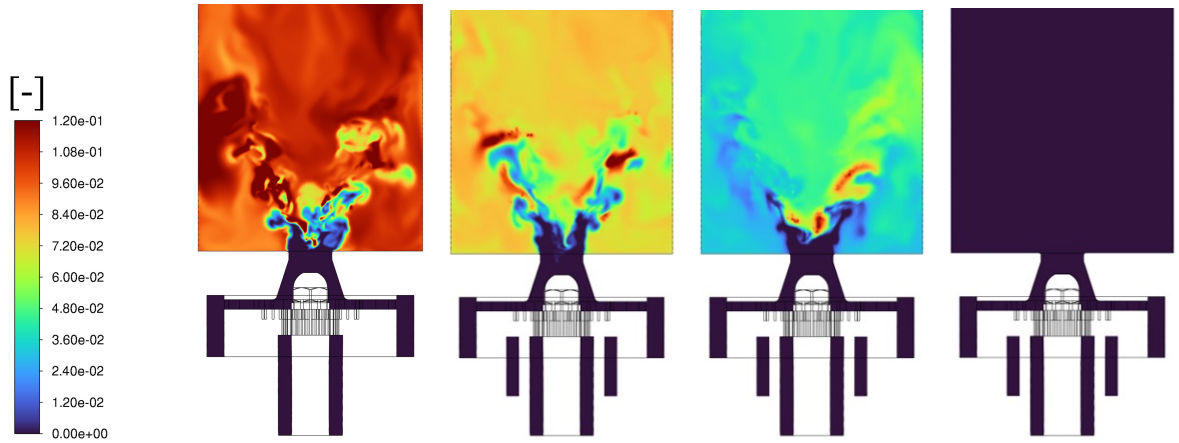

(a) HPS$_g$=0.0% **(b)** HPS$_g$=30.0% **(c)** HPS$_g$=60.0% **(d)** HPS$_g$=100.0%

Figure 7.16: The instantaneous equilibrium mass-fraction of CO_2 for the selected HPS$_g$-cases

The resulting progress variable can be observed in Figure 7.17 and ranges between zero and unity. The flame shapes and structures reported in Figure 7.9 can be identified; however, in terms of the progression of combustion products instead of HRR.

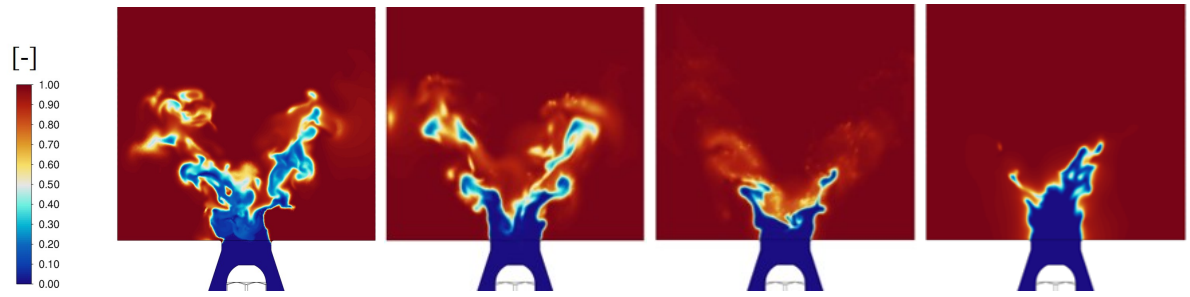

(a) HPS$_g$=0.0% **(b)** HPS$_g$=30.0% **(c)** HPS$_g$=60.0% **(d)** HPS$_g$=100.0%

Figure 7.17: The progress variable on the instantaneous flame for the selected HPS$_g$-cases

The progress variable will be used to isolate the region of interest in the burner, allowing the subsequent scalar fields to be shown within the relevant domain ($0.01 \leq c \leq 0.99$).

Proceeding to the next scalar field, the local HPS, reveals the exact characteristics of the dual-fuel mixing. The global HPS$_g$ has been defined in Equation 5.2 based on the overall mass flows. A similar definition is constructed for the local version based on α, as given in Equation 7.3. Since α is valid throughout the entire domain and is only a consequence of elemental mixing, the local HPS is likewise unaffected by the combustion process itself.

$$\mathrm{HPS} = \frac{\alpha\,\mathrm{LHV}_{H_2}}{\alpha\,\mathrm{LHV}_{H_2} + (1-\alpha)\,\mathrm{LHV}_{\mathrm{kero}}} \tag{7.3}$$

The HPS fields are reported in Figure 7.18, showing both the evolution of the scalar within the ($0.01 \leq c \leq 0.99$) region and the variation across the selected HPS$_g$ cases. For HPS$_g$=0.0% and HPS$_g$=100.0%, the pure kerosene and pure H_2 cases, respectively, a trivial solution is retrieved, as each case burns its respective fuel exclusively, as expected. The multi-fuel cases are more complex, showing that H_2 combustion occurs downstream before kerosene does. The evaporation process is enhanced by the H_2 combustion releasing the $C_{11}H_{22}$, promoting the downstream kerosene combustion. Small pockets of H_2 combustion are also found in the downstream kerosene-dominated region, along with a modest contribution of truly simultaneous combustion, indicated in white. Approximately the same pattern can be observed when transitioning towards the HPS$_g$=60.0% case, where H_2 promotes downstream kerosene oxidation. The share of H_2 is, as expected, more dominant; however, H_2 combustion extends towards the burnt side of the flame front. Another difference with the HPS$_g$=30.0% case is that the contour

appears more whitish, indicating more thoroughly simultaneous H_2 and kerosene combustion.

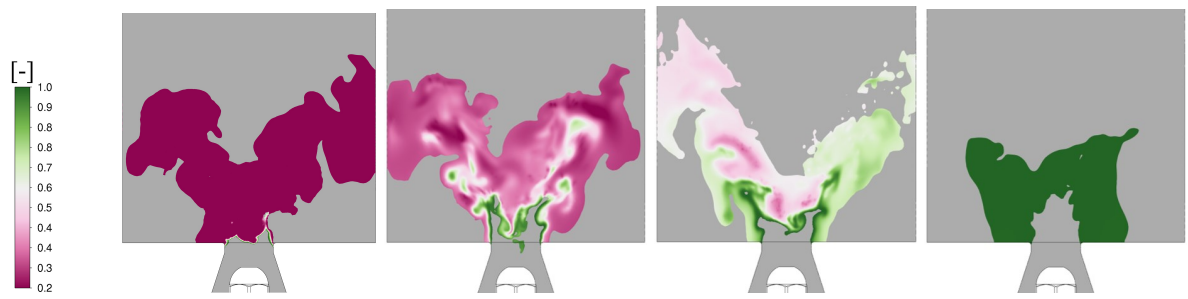

(a) HPS$_g$=0.0% **(b)** HPS$_g$=30.0% **(c)** HPS$_g$=60.0% **(d)** HPS$_g$=100.0%

Figure 7.18: Instantaneous local HPS for the selected HPS$_g$ cases, clipped to the reaction zone ($0.01 \leq c \leq 0.99$)

The next scalar field is the local equivalence ratio ϕ, indicating whether combustion occurs under lean, stoichiometric, or rich conditions throughout the entire domain and is already defined using Equation 5.12. In Figure 7.19, the contours of the equivalence ratio for the selected cases are reported. In all the cases containing the kerosene spray (excluding HPS$_g$=100.0%), a clear pattern is retrieved. In HPS$_g$=0.0%, no $C_{11}H_{22}$ (and no H_2) is initially present; hence, the most upstream region contains no fuel, corresponding to an equivalence ratio of zero. The spray flame will first burn richer; thereafter, mixing due to turbulence occurs, resulting in leaner combustion. In the dual-fuel cases, it is identified that H_2 burns upstream of the kerosene; hence, it can be observed that H_2 burns lean as intended by the design (minimizing NOx emissions). The upstream H_2 oxidation then promotes the evaporation process and the downstream richer kerosene burn. In the HPS$_g$=100.0% case, the spray is not present and the pattern of upstream lean and downstream richer combustion is not observed. Instead, the atomizer edges become richer fuel regions, whereas the central more upstream region of the flame exhibits more lean combustion. A hypothesis therefore is that the increased axial velocity oxidizes and mixes the H_2 in the center, while the H_2 accumulates in the lower-velocity regions behind the edge of the mixing tube outlet.

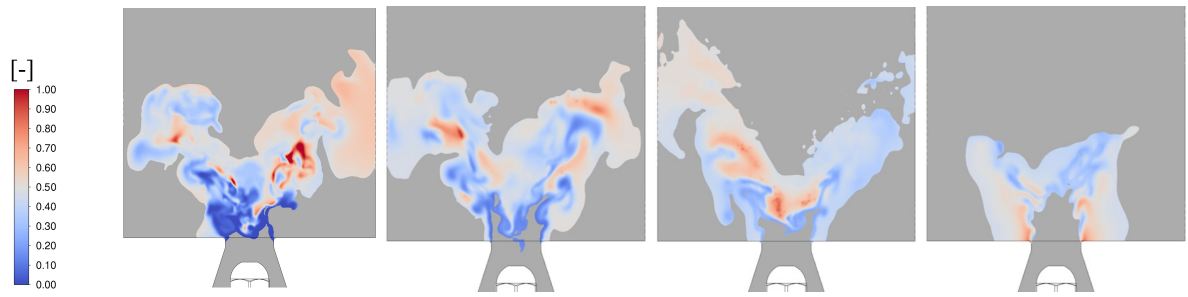

(a) HPS$_g$=0.0% **(b)** HPS$_g$=30.0% **(c)** HPS$_g$=60.0% **(d)** HPS$_g$=100.0%

Figure 7.19: Instantaneous local equivalence ratio for selected HPS$_g$ cases clipped to the reaction zone ($0.01 \leq c \leq 0.99$).

The next scalar-field is the Flame Index (FI) or Takeno number (Ta), introduced by Yamashita, Shimada and Takeno in 1996 as a method to distinguish the premixed and non-premixed (diffusion) flame regimes within a combustion field [106]. As discussed, for premixed systems, the oxidizer and fuel propagate alongside each-other while in diffusion flames the propagation occurs in opposing direction. This property can be utilized to differentiate the combustion regimes. The propagation direction can be retrieved by taking the gradient of the mass fractions (direct solution of the CFD-code). Thereafter, to define their orientation with respect to each-other, the dot product will be applied resulting in the first definition (equation 7.4).

$$G_{FO} = \nabla Y_F \cdot \nabla Y_O \tag{7.4}$$

The dot product is positive when the gradients propagate in the same direction indicating a premixed regime, while a negative dot product indicates opposing directions of fuel and oxidizer making the flame regime diffusive. The magnitude indicates how strongly the reactants are being ”pushed” into one another by the local flow field.

In further studies it became the standard to normalize the number against its magnitude as it is purely used to describe the flame regimes. This method yields a clear mapping, where 1 corresponds to premixed flames and −1 to diffusive flames [107, 108, 109, 110, 111, 112].

$$FI = \frac{\nabla Y_F \cdot \nabla Y_O}{|\nabla Y_F|\,|\nabla Y_O|} \tag{7.5}$$

Another normalization method is also widely adopted. The definition represented in equation 7.5 provides a continuous number. However, in some studies a discrete value is preferred mapping negative values to -1 (diffusive flames) and positive to 1 (premixed flames) discarding the complex partially-premixing regions. Discretizations can be achieved by dotting the denominator as done in numerous studies [111, 110, 112], the latter differentiated the regimes based on a probability density function and the flame index. In [109], it is noted that the continuous definition might be the best option when describing the (complex) mixing characteristics and inner structure of a flame and how it transitions through the combustion domain (as touched upon by [108], using the continuous definition). The continuous flame index is even utilised in partially-premixed combustion LES models [107, 109]. The FI functioned as a bridge between premixed and diffusion combustion solvers, retrieving mass fractions or the heat release rate. Considering the HOPE-combustor, its regime is not only partially-premixed, but also it is dual-fuel, imposing direct difficulties in handling the gradients of the fuel mass fractions. Figure 7.20 shows the non-conflicting and conflicting situations when considering the flame index in dual fuel mode. When the H_2 and kerosene gradients are aligned, no conflict in the flame index definition occurs. However, gradient alignment does not always occur, and conflicting situations must therefore be considered.

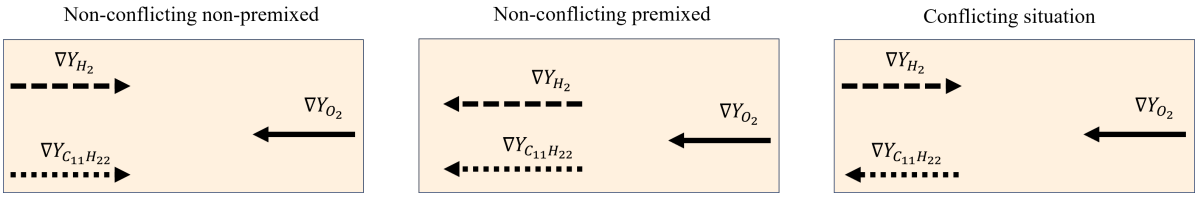

Figure 7.20: The appearing conflicts when using the flame index in dual-fuel cases

The first intuition is to simply add the gradients of H_2 and $C_{11}H_{22}$, which is defined as the mass approach, considered by the left column of figure 7.21. The arrows represent the magnitude of the gradients. It becomes clear that the situation on the top can be marked as "Non-premixed by mass" as the resultant vector opposes the oxidizer gradient, since $\nabla Y_{C_{11}H_{22}}$ outweighs the ∇Y_{H_2}. In reverse, the same can be considered for the premixed case as represented in bottom figure of the same column. However, flame classification based solely on the mass fraction does not account for the relative contribution of each fuel to the total heat release. Therefore, a power-weighted definition seems more appropriate, as the thermal power originating from each combustion mode is ultimately the most critical quantity from a flame perspective. The mass fractions can be converted to power, considering the LHV of the two fuels. In the second column of figure 7.21 is the corresponding situation of the left column displayed, where the arrows are scaled with the LHV. Consider the top row, the significantly higher LHV of H_2 compared to kerosene, causes the resultant fuel gradient vector to reverse direction upon LHV scaling, switching the classification from non-premixed by mass to premixed by power. The bottom row shows the reverse situation, where a premixed classification by mass becomes non-premixed by power due to the same LHV scaling effect.

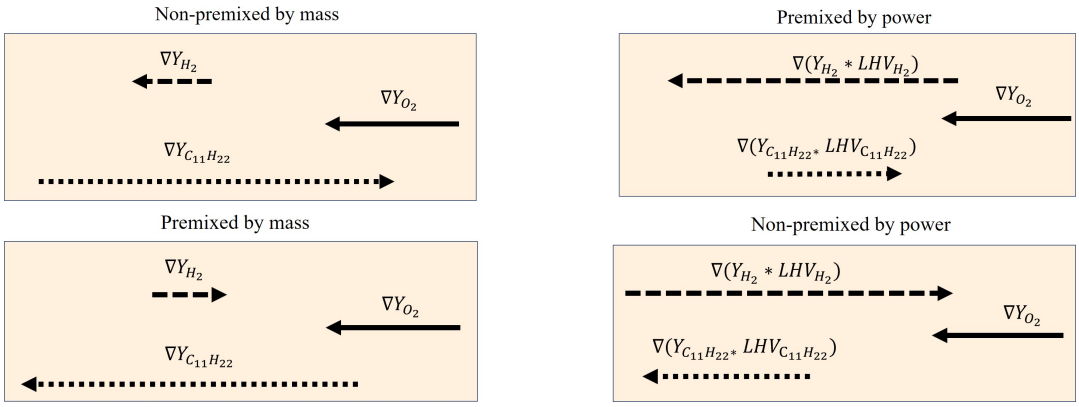

Figure 7.21: Dual-fuel flame index: interpretation and definitions considerations

The flame index definitions are given in Equation 7.6.

$$\begin{aligned} \mathrm{FI}_{C_{11}H_{22}} &= \frac{\nabla Y_{C_{11}H_{22}} \cdot \nabla Y_{O_2}}{|\nabla Y_{C_{11}H_{22}}||\nabla Y_{O_2}|} \\ \mathrm{FI}_{H_2} &= \frac{\nabla Y_{H_2} \cdot \nabla Y_{O_2}}{|\nabla Y_{H_2}||\nabla Y_{O_2}|} \\ \mathrm{FI}_{mf} &= \frac{\nabla(LHV_{\mathrm{kero}} \cdot Y_{C_{11}H_{22}} + LHV_{H_2} \cdot Y_{H_2}) \cdot \nabla Y_{O_x}}{|\nabla(LHV_{\mathrm{kero}} \cdot Y_{C_{11}H_{22}} + LHV_{H_2} \cdot Y_{H_2})||\nabla Y_{O_x}|} \end{aligned} \tag{7.6}$$

Although, when considering the actual mixing characteristics, the multi-fuel definition should be used; however, the single-fuel definitions isolate the mixing characteristics of the corresponding fuel. The $\mathrm{FI}_{C11H_{22}}$ shows that kerosene first becomes available in a non-premixed form, with premixing occurring further downstream. In the HPS_g=30.0% case, downstream H_2 combustion mixes the non-premixed kerosene in this downstream region with the upstream gases, resulting in a more distributed field. This effect is enhanced with increasing H_2, as the HPS_g=60.0% case shows an even more distributed field. For the pure H_2 case, no kerosene is present and the flame index therefore yields a trivial solution.

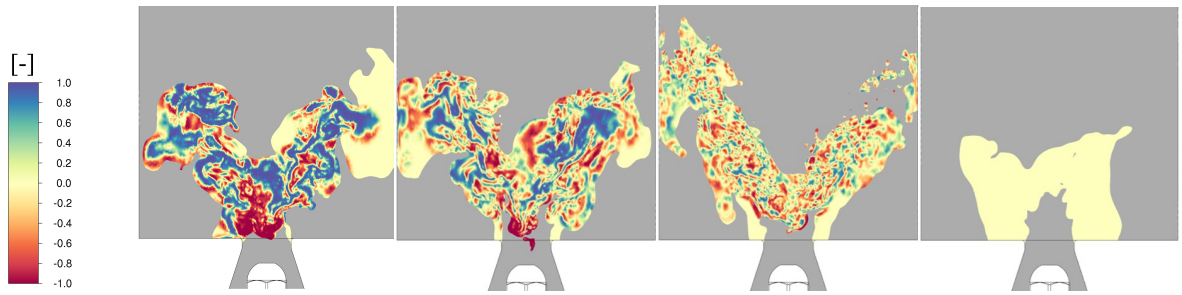

(a) HPS_g=0.0% **(b)** HPS_g=30.0% **(c)** HPS_g=60.0% **(d)** HPS_g=100.0%

Figure 7.22: The instantaneous $\mathrm{FI}_{C_{11}H_{22}}$ for the selected HPS_g-cases

The FI_{H_2} shows a field for the HPS_g=0.0% as H_2 is a radical in kerosene combustion; the actual effect of the H_2 radical is negligible for the behaviour of the flame and should not be considered. Moving to the cases with actual H_2-fuel contribution, the same pattern can be observed for the various cases. The H_2 first appears as a premixed mixture leaving the mixing tube; then a transition point is reached, where a non-premixed regime is observed. However, when consulting again the HPS contours (see figure 7.18), it appears that H_2 is mostly burnt in the upstream region of the flame front, hence, in a premixed configuration.

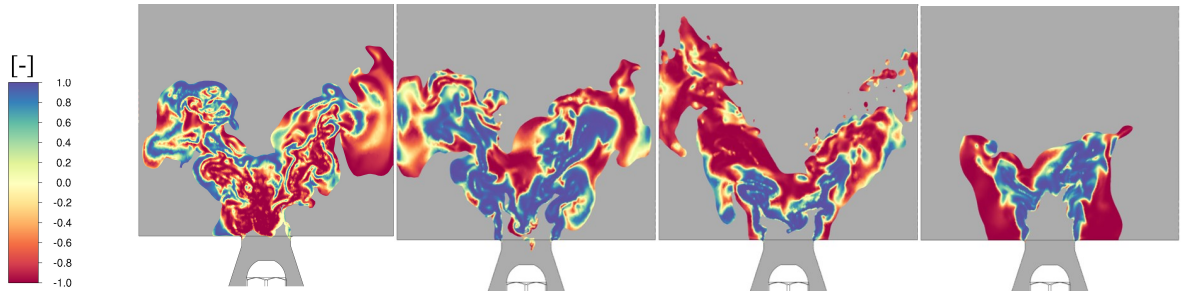

(a) HPS$_g$=0.0% **(b)** HPS$_g$=30.0% **(c)** HPS$_g$=60.0% **(d)** HPS$_g$=100.0%

Figure 7.23: The instantaneous FI$_{H_2}$ for the selected HPS$_g$-cases

The actual dual-fuel mixing behaviour is represented in Figure 7.24. It can be observed that for HPS$_g$=0.0%, the contour converges to the FI$_{C_{11}H_{22}}$ definition, showing the insignificance of the H_2. The pure H_2 case converges to the HPS$_g$=100.0% of the FI$_{H_2}$ definition. The dual-fuel cases are as expected a mix of the FI$_{C_{11}H_{22}}$ and FI$_{H_2}$. The clear structure of the H_2 first premixed and subsequently non-premixed is observed, however, the field becomes more disturbed by the spray flame mixing characteristics.

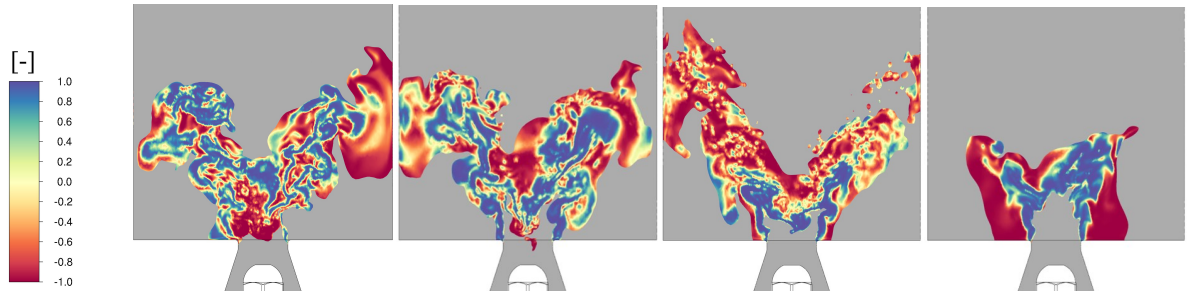

(a) HPS$_g$=0.0% **(b)** HPS$_g$=30.0% **(c)** HPS$_g$=60.0% **(d)** HPS$_g$=100.0%

Figure 7.24: The instantaneous FI$_{mf}$ for the selected HPS$_g$-cases

7.2.3. Flame Quantitative Analysis

To further investigate and characterize the flame, and to better understand the interaction between kerosene and hydrogen as well as their mixing and combustion behaviour, three methods are employed: flame maps, scatter plots, and line analysis.

The flame maps represent the interaction between the scalar fields HPS, equivalence ratio, progress variable, and flame index within the flame region defined by the progress variable range ($0.01 \leq c \leq 0.99$), and therefore correspond directly to the previously discussed contours. The maps are weighted by the local power, inherently revealing a more accurate picture than the contours alone, as the exact peaks of power generation within the flame front can be distinguished more clearly.

Consider the interaction between the equivalence ratio and the HPS reported in Figure 7.25. For HPS$_g$=30.0%, the map shows a concentration of power around the global equivalence ratio ϕ_g=0.494, with the power approximately normally distributed around this value. Similarly, the power distribution is approximately normally distributed around the global HPS value. Furthermore, the associated power distribution shows an inverse relationship between equivalence ratio and HPS. Regions with high HPS are associated with lower equivalence ratios, whereas regions with lower HPS correspond to power generation by higher equivalence ratios, indicating that H_2 enables leaner combustion conditions. Increasing the hydrogen content to HPS$_g$=60.0% shows a similar response on the power distribution, the equivalence ratio and the HPS, retaining the inverse relationship between the two quantities. However, in this case, two peak regions of power generation can be distinguished in the map. The first corresponds to a very lean H_2 flame, significantly leaner than the global equivalence ratio ϕ_g=0.467. This may be attributed to more dominant upstream H_2 oxidation. The second peak burns slightly richer than ϕ_g. Some of the H_2 is already consumed upstream under lean conditions, thereby increasing ϕ in the downstream combustion

zone. The range over which power is actually generated is therefore much broader, in terms of both local HPS and ϕ, in the HPS$_g$=60.0% case compared to the HPS$_g$=30.0% case.

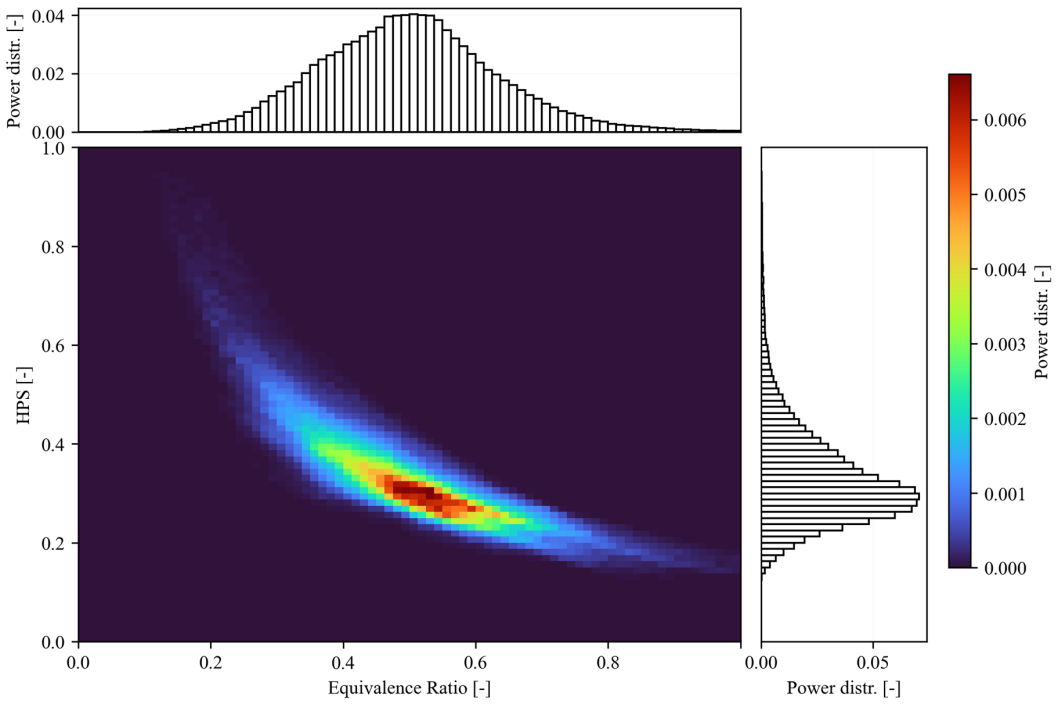

(a) HPS$_g$ = 30.0%

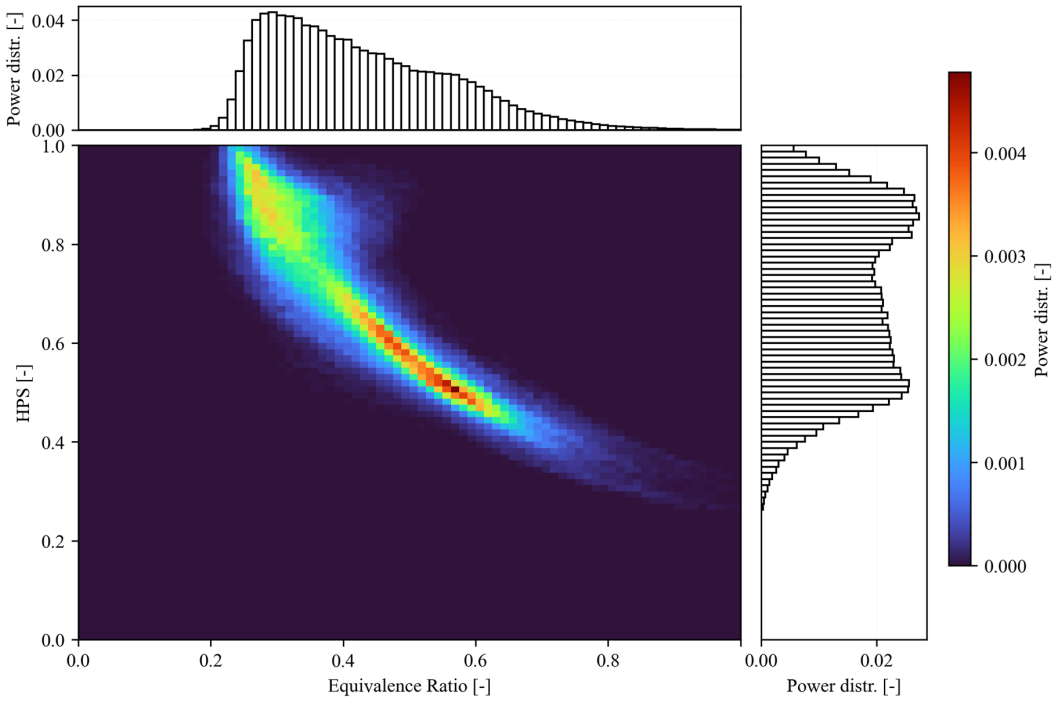

(b) HPS$_g$ = 60.0%

Figure 7.25: Map of the interaction between the local equivalence ratio ϕ and the HPS of the instantaneous flames where $0.01 \leq c \leq 0.99$

Figure 7.26 shows the interaction between the HPS and the progress variable. Notably, the instantaneous HPS_g=30.0% field shows an almost negligible contribution of hydrogen-dominated combustion; however, it is present. Although the time-averaged field reveals a more dominant upstream attached hydrogen-dominated region (see Figures 7.2 and 7.4), the instantaneous field shows only weak attachment compared to the time-averaged contour (see Figure 7.9). Since this upstream hydrogen-dominated region (near the edge of the mixing tube outlet) is weakened in the instantaneous field, the flame map shows an almost negligible contribution of hydrogen-dominated combustion. The reason for this apparent discrepancy between the instantaneous and time-averaged contour fields is that, in the instantaneous field, the HRR is confined to a very thin region at a fixed location, making the upstream attached flame appear relatively weak. In the time-averaged field, however, the averaging process combines many instantaneous flame realizations over time. Consequently, a much broader spatial region contributes to the averaged HRR signal, as multiple neighbouring regions experience intermittent heat release throughout the averaging period. This causes the upstream flame structure to appear brighter and more dominant in the time-averaged contours than in the instantaneous fields. Nevertheless, it must be considered that although the local HRR in this upstream region may be considerable, the associated volume is very small, and hence the net power contribution of this upstream region remains limited. Nevertheless, the main power generation appears to be initiated by kerosene combustion, although some H_2 combustion is occurring further upstream. The local HPS remains considerably low throughout the high-power-generating zone. In contrast, HPS_g=60.0% clearly shows that combustion is initiated by a hydrogen flame, corresponding to the upstream region near the mixing tube outlet edge. As expected, most of the power is generated near the end of the flame front, where the flame is more developed.

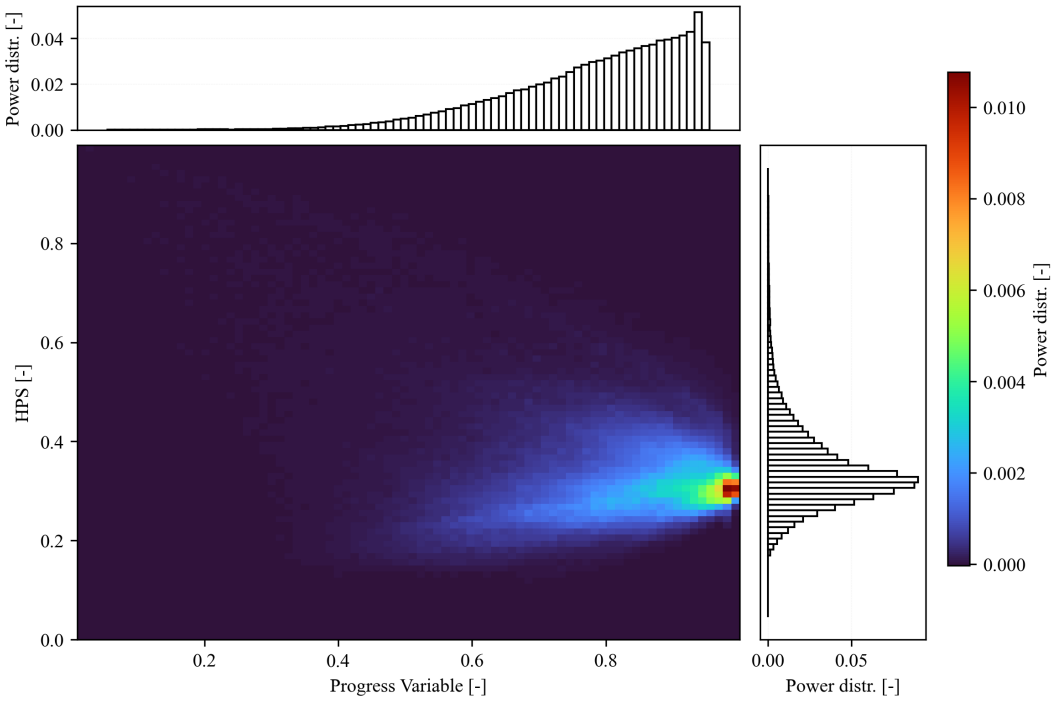

(a) HPS_g = 30.0%

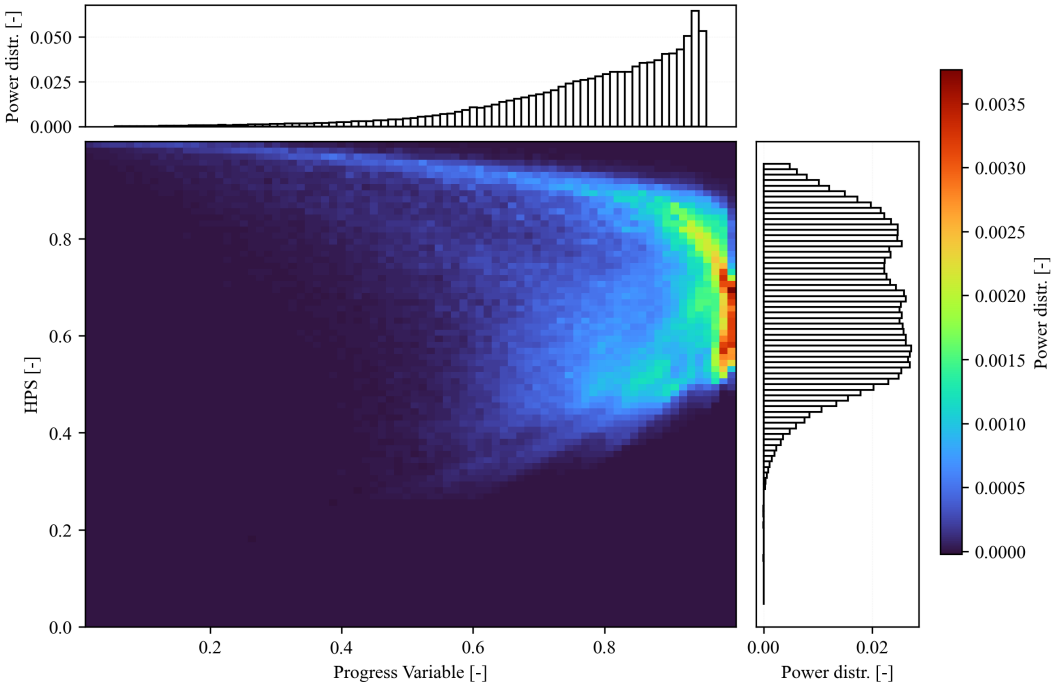

(b) HPS_g = 60.0%

Figure 7.26: Map of the interaction between the progress variable (c) and the HPS of the instantaneous flame where $0.01 \leq c \leq 0.99$

The following interaction to discuss is between the HPS and the flame index. For HPS_g=30.0%, two main regions are distinguished, corresponding to premixed and non-premixed power generation. The premixed contribution is considerably larger than the non-premixed one, although a substantial partially premixed regime is also present. The local HPS of the partially premixed and non-premixed regions centers around the global HPS_g=30.0%, while lower local HPS values are found in the purely premixed region, as hydrogen is able to burn under even leaner

conditions than kerosene. The same pattern is observed for HPS_g=60.0%, however, the global shift towards a higher hydrogen content results in a more dominant premixed contribution, consistent with hydrogen premixing earlier within the mixing tube.

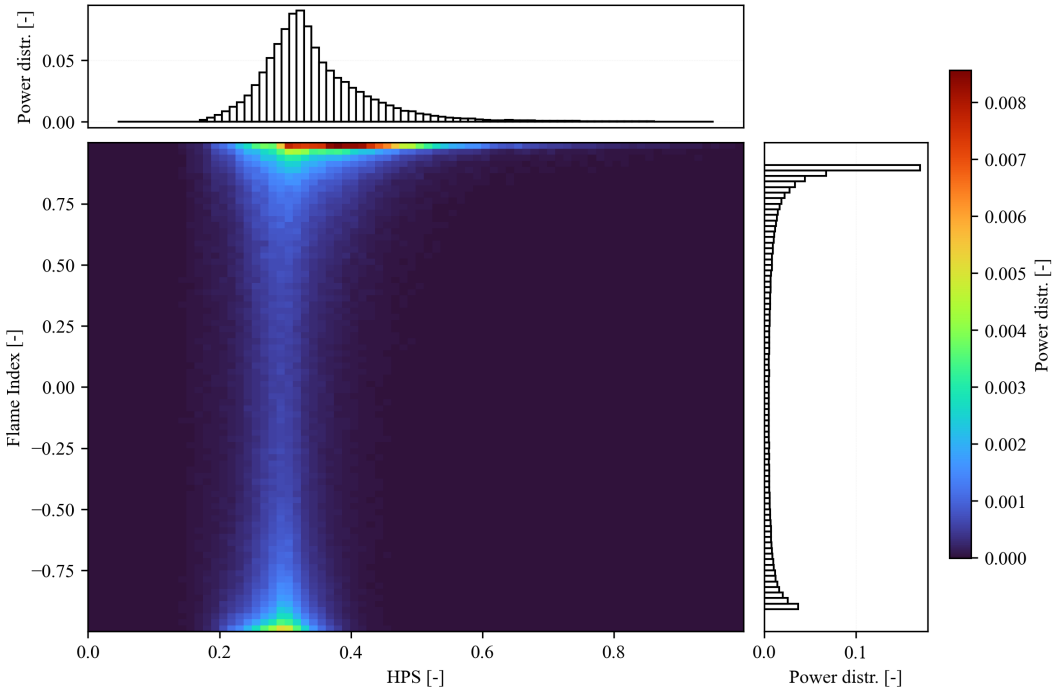

(a) HPS_g = 30.0%

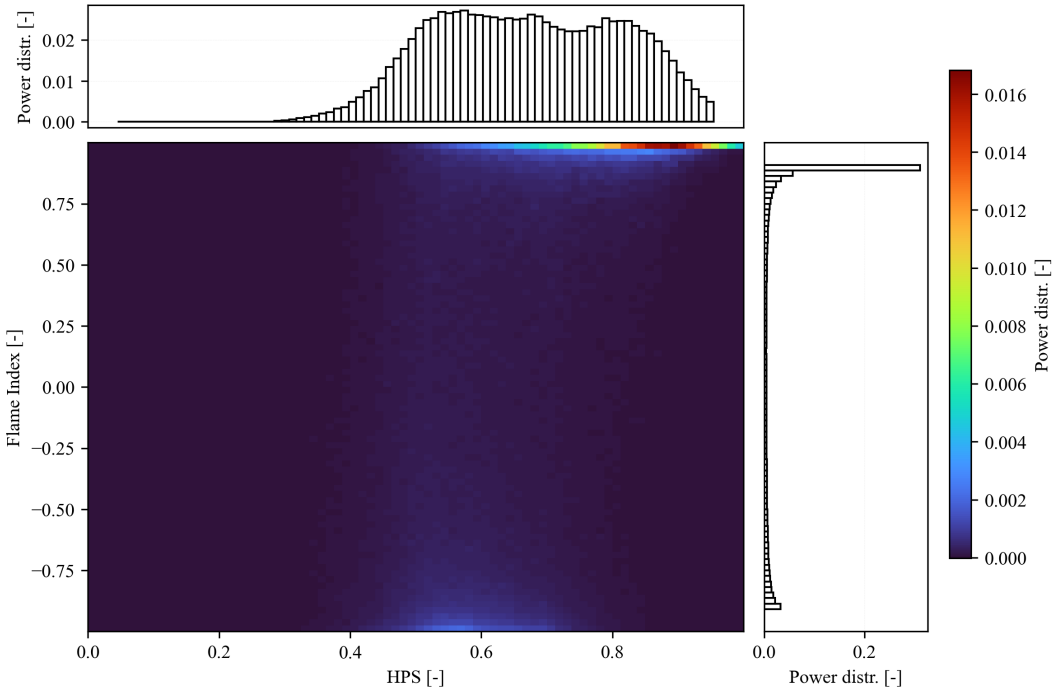

(b) HPS_g = 60.0%

Figure 7.27: Map of the interaction between the HPS and the flame index of the instantaneous flame where $0.01 \leq c \leq 0.99$

In Figure 7.28, the interaction between the HPS, equivalence ratio, and flame index is illustrated. This is achieved through a scatter plot with the equivalence ratio on the x-axis and the HPS on the y-axis. The data points are colored according to the flame index, indicating the corresponding flame regime. The considered region is again defined by ($0.01 \leq c \leq 0.99$). In the HPS = 30.0% case, the inverse relation between HPS and equivalence ratio is again observed. The H_2 burns in a premixed mode. As the H_2 content decreases and the equivalence ratio increases, more non-premixed marked points are observed. The HPS = 60.0% case shows a similar trend, with H_2 burning in a lean premixed mode; as the equivalence ratio increases, the HPS decreases. In the HPS_g=60.0% case, more premixed hydrogen is found at higher equivalence ratios, while non-premixed regions are observed at higher HPS values.

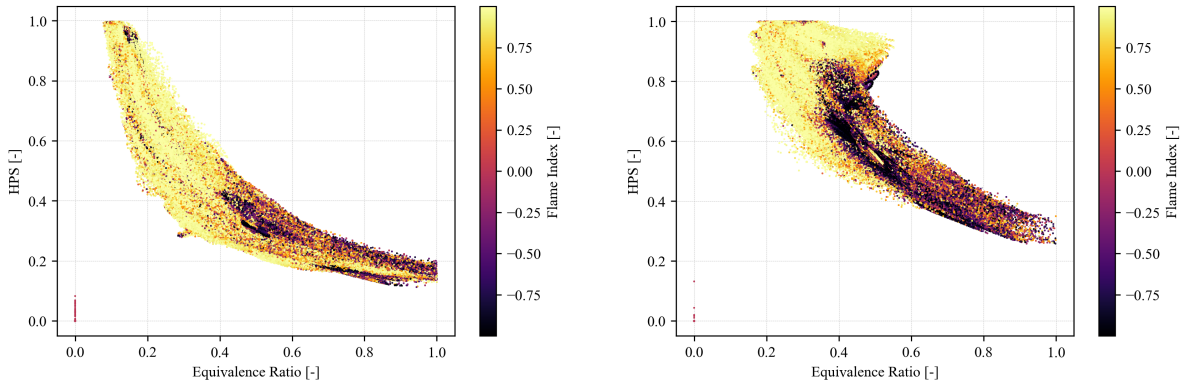

(a) HPS_g=30.0% **(b)** HPS_g=60.0%

Figure 7.28: Interaction between the equivalence ratio, HPS, and flame index within region marked by $0.01 \leq c \leq 0.99$

In Figure 7.29, the relation between temperature, HPS, and equivalence ratio is shown for HPS_g=30.0%. At temperatures starting around 300K, only H_2 is present as fuel, kerosene has not yet evaporated and is only present as liquid, hence $C_{11}H_{22}$ is not available. The temperature initially increases due to H_2 oxidation. This temperature rise promotes droplet heating and consequently spray evaporation, releasing $C_{11}H_{22}$ vapour, thereby reducing the local HPS. Therefore, upstream H_2 combustion promotes spray evaporation and thus downstream kerosene oxidation. The transition between high and low HPS is gradual and smooth. The same interaction is observed for HPS_g=60.0%. However, the curve is much steeper at low equivalence ratios and temperatures, as more H_2 oxidises upstream without significant carbon content. Pure kerosene is only observed slightly on the lean side of the stoichiometric condition and in the hottest regions.

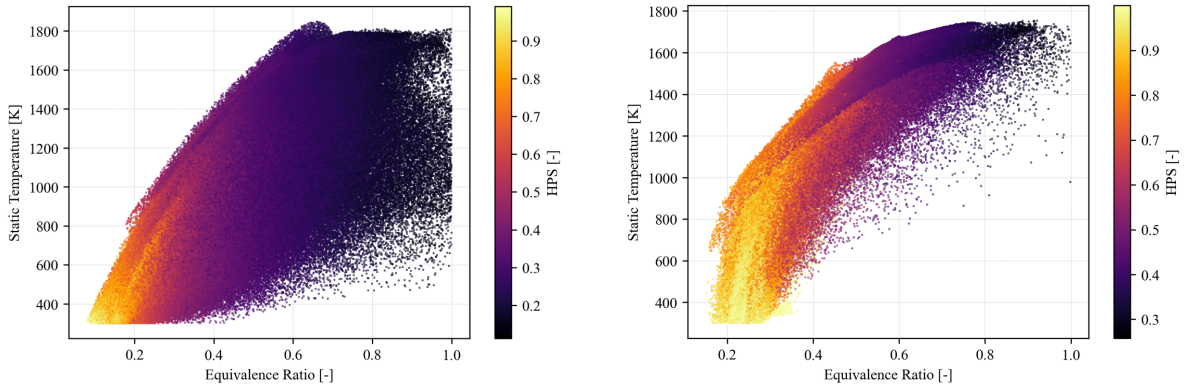

(a) HPS_g=30.0% **(b)** HPS_g=60.0%

Figure 7.29: Interaction between equivalence ratio, temperature and HPS within the region marked by $0.01 \leq c \leq 0.99$

As already established, most non-premixed characteristics are found downstream and hence later in the combustion process. However, for the HPS_g=30.0% case, some initial non-premixed flames are present, as can be

observed in Figure 7.30a, where dark spots can be found in the region of low progress variable, indicating non-premixing in this region. Advancing along the progress variable, it becomes apparent that a partially premixed regime is established. Near the end of the combustion, a more non-premixed-dominated regime can be found; this regime starts earlier for lower HPS values, around $c = 0.5$ and HPS = 0.15. For the HPS_g=60.0% case, negligible non-premixed points are found at the start; only near the end non-premixed points are present, hence the combustion is initiated by premixed flames. Similarly to the HPS_g=30.0% case at $c > 0.5$, the lower the HPS, the earlier in the progression non-premixed points can be found.

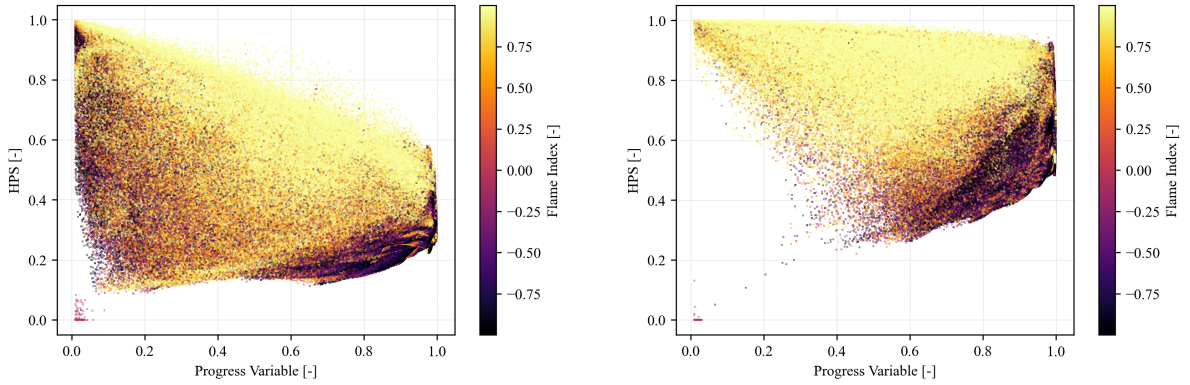

(a) HPS_g=30.0% **(b)** HPS_g=60.0%

Figure 7.30: Interaction between the progress variable, HPS, and flame index within the region marked by $0.01 \leq c \leq 0.99$

In Figure 7.31, the evolution of the species along the central axial line is shown, which is indicated by the green dashed line in the contour. The contour on the top right only shows the HPS_g=60.0% case, however, this is only for illustration purposes as the exact same line analysis is performed on the other selected HPS_g cases. The line is drawn in a 3D space, and variations arise due to evaporation, combustion, and mixing occurring in the full three-dimensional flow field. The top left figure shows the temperature; the considered axial positions in the constructed plots are set such that the temperature rise is captured, grasping the evolution of the species over the flame front. The HPS_g=100.0% reaches a slightly lowered final temperature and combustion starts slightly more downstream. Hydrogen starts burning from the swirler exit edges and propagates straight, with a minor HRR in the center, while kerosene, in the current simulation, contains a central flame increasing the temperature on the central line. The HPS_g=60.0% shows to be the most unsteady through all the plots, which is attributed to slightly insufficient averaging.

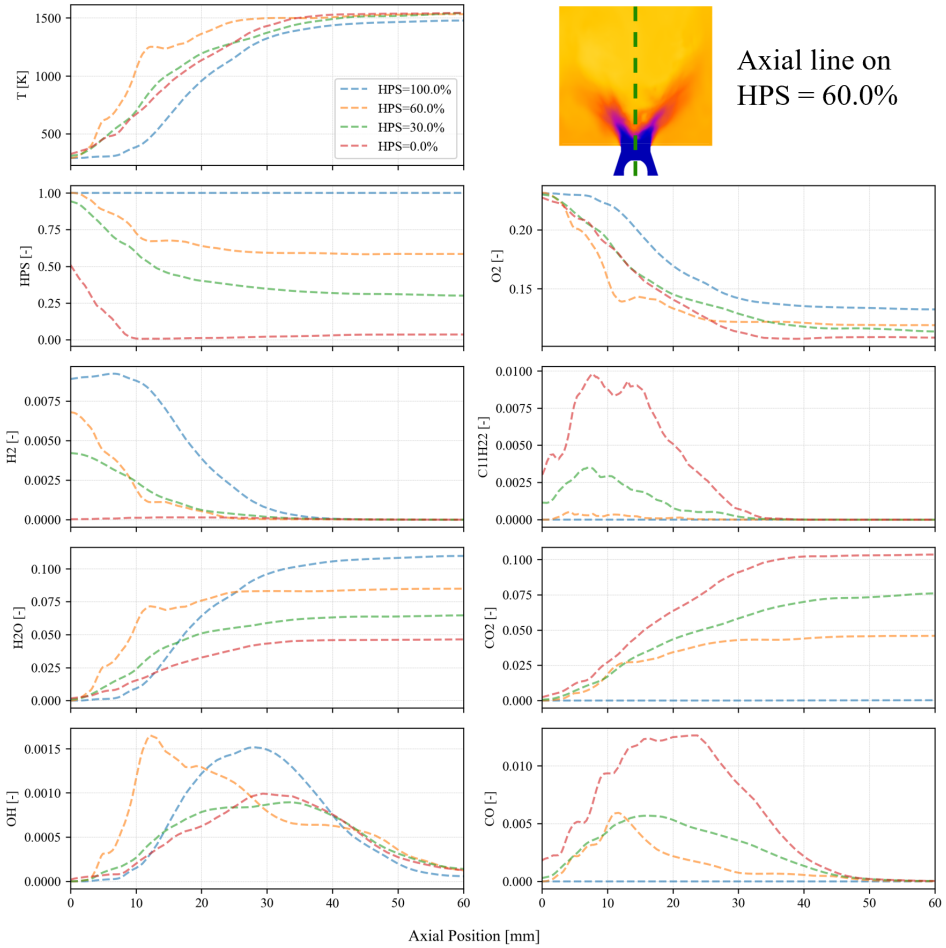

Figure 7.31: Time-averaged species evolution over the central, axial flame front; the species graphs show mass fractions

The second plot on the left considers the HPS along the axis. Since H_2 is already contained in the mixture, the HPS is larger upstream and then starts to decrease once evaporation starts, leading to the release of $C_{11}H_{22}$. When evaporation and mixing with $C_{11}H_{22}$ occur, the HPS converges to its global value. In the second plot on the right, the O_2 evolution shows an inverse relationship with temperature. It can be observed that lean conditions are occurring, as O_2 remains at a nonzero value. The next row shows the two fuels: H_2 is readily available and directly starts combusting. $C_{11}H_{22}$ requires some evaporation distance. Both H_2 and $C_{11}H_{22}$ are fully consumed, again indicating lean conditions. The formation of products is shown in the following row. As discussed earlier, a higher hydrogen content leads to higher H_2O production and lower CO_2 production. The same trend is observed in these plots. HPS_g=100.0% shows the highest H_2O production and no CO_2, while HPS_g=0.0% produces the highest CO_2 levels and the lowest H_2O levels. A similar conclusion can be drawn from the final row, showing the CO and OH species. For all HPS, the final value of CO approaches zero, indicating complete combustion. The OH values do not decrease to zero, and the HPS_g=100.0% case has the lowest concentration of OH after the flame front. This can be attributed to the slightly higher temperature of the kerosene flames, which causes slightly more H_2O dissociation.

Overall, the results demonstrate a consistent trend of lean combustion across all HPS_g cases, with complete fuel consumption and a clear transition in product distribution from CO_2-dominated products under kerosene-rich conditions to H_2O-dominated products as the hydrogen fraction increases. CO is oxidized to CO_2 along the axis, indicating complete oxidation of the carbon-containing fuel.

Furthermore, in both the HPS_g = 30.0% and HPS_g = 60.0% configurations, the flame structure is characterized by an upstream lean hydrogen flame. As kerosene evaporates and mixes downstream, the local equivalence ratio increases, leading to a richer combustion zone dominated by kerosene oxidation. Consequently, the upstream hydrogen flame promotes downstream stabilization of the spray flame, which exhibits a mixed combustion mode

with both premixed and non-premixed characteristics.

A clear shift in flame behaviour is observed when increasing HPS_g from 30.0% to 60.0%. In the higher hydrogen case, upstream hydrogen oxidation becomes significantly more dominant, resulting in an overall leaner and more strongly premixed combustion regime. This enhanced hydrogen contribution strengthens the premixed flame structure while reducing the relative influence of the downstream spray-controlled kerosene combustion region.

7.3. Improvements of the Simulation Framework

The agreement and topology analysis revealed discrepancies between the experiments and the SBES simulations. The LoH is predicted too low for the HPS_g=0.0% case, and with hydrogen addition, an attached flame is predicted prematurely due to the intense upstream HRR region near the edge of the mixing tube outlet. Nevertheless, even disregarding this upstream region, the HRR along the central axis is anchored too far upstream for the predicted LoH to match the experimental data. The root cause of these discrepancies may be attributed to a variety of factors, including errors induced by the reaction mechanism, turbulence, evaporation, radiation, CAD-experimental setup alignment, and model limitations. Among these, the adiabatic wall boundary condition is considered a major assumption, as it may cause wall temperatures to be significantly higher than in reality. Furthermore, the spray boundary conditions remain uncertain, likely affecting the spray structure. The thermal wall boundary conditions and spray boundary conditions are therefore further explored in this section.

7.3.1. Non-Adiabatic Boundary Conditions

The RANS-CHT simulation is performed for both HPS_g=0.0% and HPS_g=100.0% and the setup is clarified in Section 6.5.2. Since the HPS_g=100.0% case already shows satisfactory agreement in the SBES results, only the HPS_g=0.0% case is considered further in the SBES simulations and will therefore be discussed in this section. However, the RANS-CHT results for HPS_g=100.0% showed that, within the practical TCC range [1000,$Wm^{-2}K^{-1}$, 15000,$Wm^{-2}K^{-1}$] retrieved from [86], no significant changes in flame shape or the corresponding wall temperature distribution are observed. Therefore, for the RANS-CHT simulation of HPS = 0.0%, only TCC= 1000,$Wm^{-2}K^{-1}$ is considered, as this value is estimated to be the most feasible based on the expected contact pressure, interface temperature, and surface roughness. The results for HPS_g=100.0% are further reported in Appendix D.

The temperature profile along the quartz cylinder (from the backplate extending axially towards the orifice), retrieved from the RANS-CHT simulation, is overall colder than the adiabatic-SBES prediction, except in the axial range of approximately 25–75mm where the two are comparable. The elevated temperature at an axial position of 0mm corresponds to the outermost radial position of the backplate, and the initially higher adiabatic-SBES temperature is therefore most likely attributed to the elevated backplate temperature. The downstream decrease in temperature in the RANS-CHT simulation is attributed to heat exchange with the ambient surroundings, whereas in the adiabatic SBES case, no heat exchange is permitted and the thermal energy is therefore retained within the domain. A smoothened version of the RANS-CHT temperature distribution is proposed as the new SBES boundary condition. The smoothening provides a cleaner integration from a numerical perspective, and moreover, the small deviations present in the original profile cannot be physical, as the simulation is not capable of resolving this level of detail.

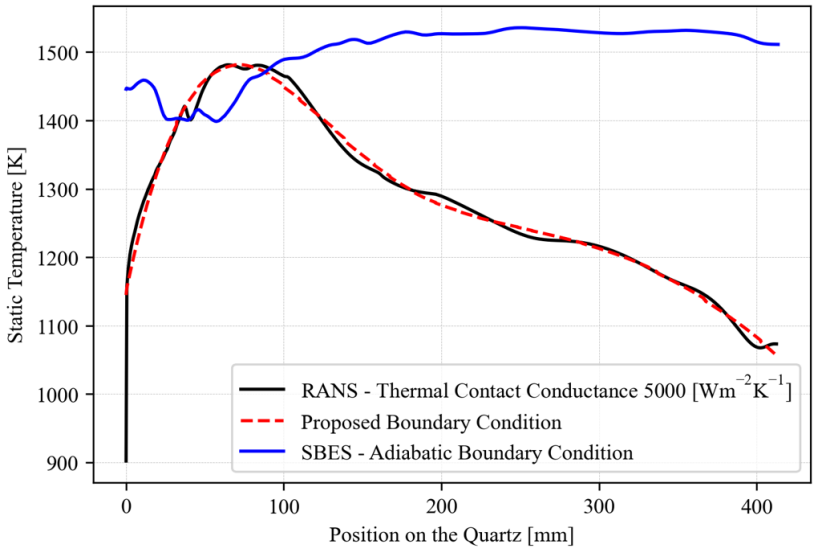

Figure 7.32: Resulting thermal boundary conditions for the quartz at HPS_g=0.0%

The retrieved backplate temperature profile and the corresponding temperature contour from the CHT-simulation can be observed in Figure 7.33. Two regions are highlighted using circles. At the dashed circle, radial/backplate position of 10mm, a small jump in temperature is observed. This jump is caused by the rounded edge geometry. The temperature is extracted along a straight line located on the backplate; however, due to the edge rounding, the actual solid surface deviates from this line and locally bends away. As a result, the sampling point enters the fluid region instead of remaining on the solid wall. Consequently, the extracted temperature is no longer strictly representative of the backplate surface. Since the objective is to obtain the solid backplate temperature, this small peak can be disregarded. Considering the solid circle, the radial/backplate position of 30mm shows a steep increase, which is due to the TCR between the two solid blocks. It is observed that this temperature jump does not occur in the adiabatic SBES case, where the backplate is represented as a single adiabatic surface. The most significant result from this CHT-analysis is that the temperature profile on the backplate retrieved from the CHT-simulation is more than halved compared to the adiabatic-SBES results, which is a significant difference. The lowered backplate temperature increases the LoH, as a longer pre-heating distance is required. However, the CHT model allows heat conduction through the solid blocks, potentially pre-heating the flow in the nozzle ducts, swirler, and plenum, thereby reducing the required preheating distance. This LoH reduction will not be present when applying thermal boundary conditions to the backplate and quartz only in the SBES-simulation. This effect is, however, regarded as negligible, and further notes on this point can be found in Appendix D.2.

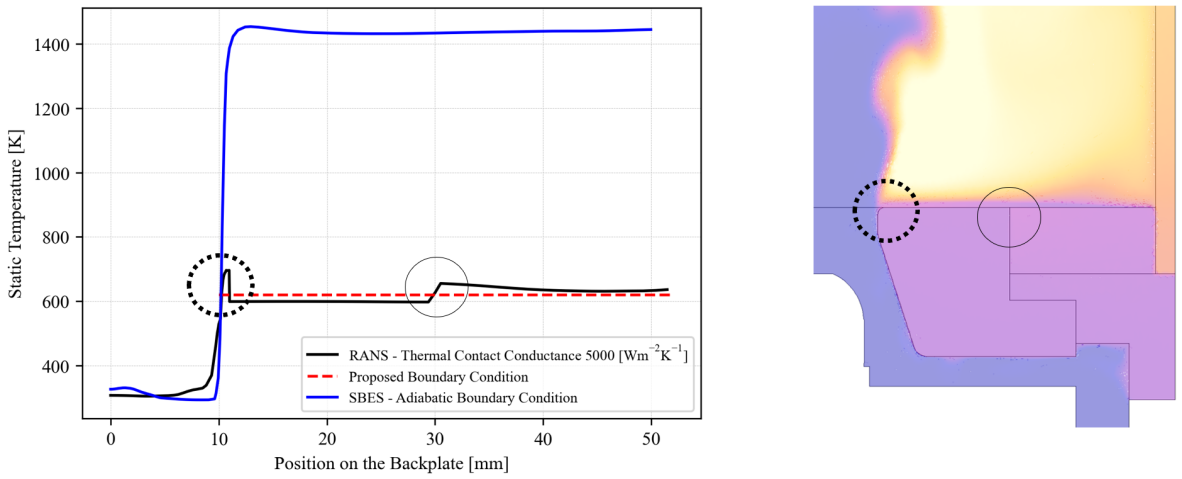

Figure 7.33: Resulting thermal boundary conditions of the backplate at HPS_g=0.0%

The SBES simulation with thermal boundary conditions retrieved from the RANS-CHT is reported in Figure 7.34 for HPS_g=0.0%, alongside the adiabatic SBES results for comparison. The LoH increases slightly, attributed to a longer pre-heating distance resulting from the cooler backplate. The flame also extends further radially, reaching the quartz cylinder, likely due to the slightly elevated quartz temperature in the flame region. Most significantly, the central part of the flame is weakened, which is more consistent with the experimental observations. This central flame region extends downward, contributing to a reduction in LoH, and its complete elimination would bring the predicted and experimental LoH into closer agreement. The weakening of the central flame is attributed to the lowered backplate temperature, decreasing the reactivity in the region.

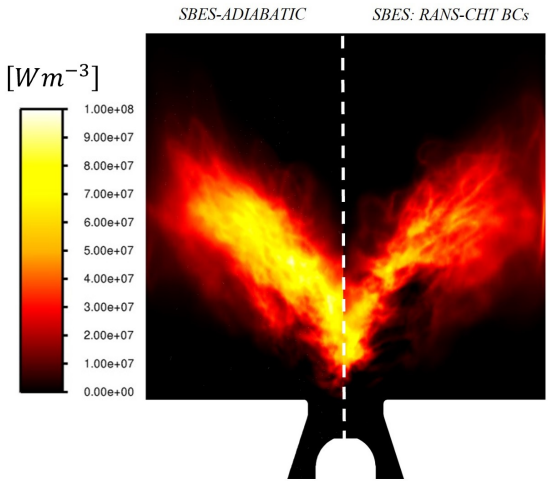

Figure 7.34: The resulting heat release contour for HPS_g=0.0% with imposed set wall temperatures on the backplate and quartz, which are retrieved from the RANS-CHT simulation

Although no RANS-CHT boundary condition analysis has been conducted for the dual-fuel cases, an interesting observation can be drawn. The primary discrepancy between the experimental data and the SBES for the dual-fuel cases was the premature flame attachment at the mixing-tube outlet edge. This upstream HRR region is predominantly attributed to H2 oxidation, as kerosene still requires evaporation and hence no $C_{11}H_{22}$ is present in this region. In the adiabatic SBES (although for HPS_g=0.0%), the backplate temperature was found to well exceed the autoignition temperature of H_2 (approximately 850,K), and given the extremely broad flammability limits of H_2 (4–75,vol% in ambient conditions), independent hydrogen combustion in this region is expected. In the RANS-CHT simulation, however, the backplate temperature is considerably reduced to approximately 600,K, dropping well below the autoignition temperature of H_2 (regarding HPS=0.0% and also for HPS_g=100.0% in Appendix D. Having this colder temperature would suppress independent H_2 combustion in the upstream region, eliminating the upstream combustion and allowing the kerosene–hydrogen interaction observed experimentally to be better captured in the CFD.

7.3.2. Spray Boundary Conditions

The structure of the spray has a significant influence considering conventional combustion [28] and hence it is likely of utmost importance to have an accurate representation in the (SBES) simulation. The exact spray boundary conditions remain unknown, and therefore a sensitivity analysis has first been performed to check which parameters have the largest influence and which do not. The sensitivity analysis involves many simulations and hence RANS-FGM had to be adopted for computational efficiency, compromising simulation accuracy. The setup of these RANS simulations for exploring this spray influence is discussed in Section 6.5.1.

The LoH has been used as a convenient quantitative measure for tracking the influence of the spray boundary conditions on the flame. In SBES, the HRR intensity contours were utilized to define the LoH. In RANS-FGM, the HRR is solved as a post-processing step and hence a more native variable for RANS-FGM might be appropriate. The reaction mechanism Z79 contains the OH concentration and this quantity can be a suitable definition for LoH as used by [113, 114]. Nevertheless, the product formation rate also presents itself as a viable LoH definition, as it directly marks the onset of reaction and is native to the RANS-FGM combustion model. The regions marked as containing the flame for OH (blue) and PFR (yellow), visualized for various intensity contours, are reported in

Figure 7.35. Both the OH and the PFR definitions might be suitable; however, a 2% OH also marks the post-flame region as within the flame front and might therefore not be the most optimal choice. The PFR-based definition with a threshold of 14% is selected as an appropriate value based on visual inspection of the flame, noting that the contours remain largely unchanged in the range of 2–25%, making any intermediate value a reasonable choice.

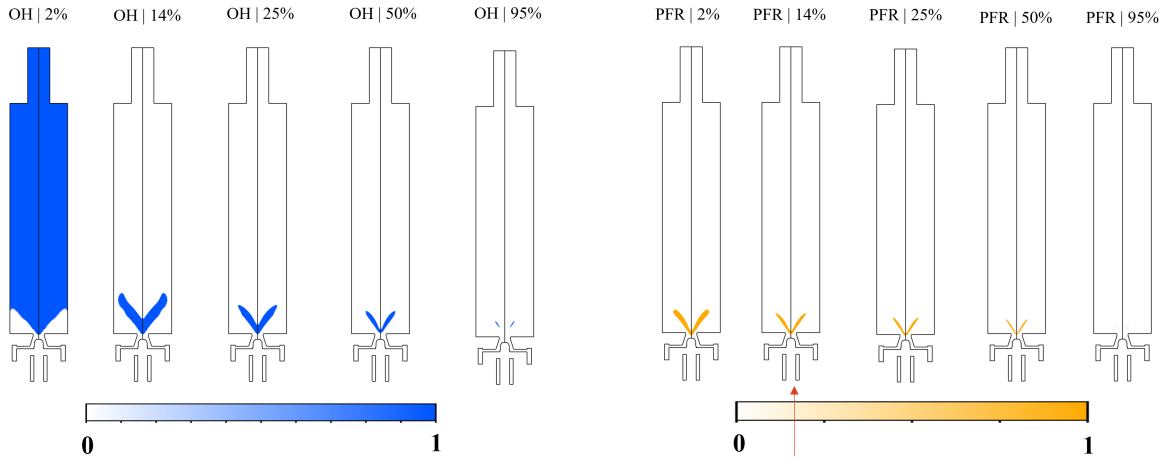

(a) Intensity contours

(b) Product formation rate intensity contours

Figure 7.35: Intensity contours for the LoH definition

The actual spray boundary conditions, which may have a significant influence, are the SMD, spray velocity, spread parameter (q), hollow-cone (and associated swirl fraction), mass-flow distribution, and staggering. Other definitions are known from the geometry; however, it is still assumed that the spray produces an initial spray angle of 60 degrees, irrespective of the mass flow through the atomizer, as this is the angle it produces at its rated mass flow. The tested SMD values result from a 25% increase in the pressure across the atomizer (SMD=10.5, μm) and a 25% decrease (SMD=18.2, μm) with respect to the nominal, by [54] measured pressure used in the SBES simulations. In Figure 7.36, the influences of SMD (7.36a), spray velocity (7.36b), and q (7.36c) are shown. The x-axis displays both the parameter values and the simulation case labels, where each letter corresponds to a parameter and the attached number refers to the specific case within that parameter set. The corresponding contours and spray structures are reported in Figures B.1 and B.2, respectively. Clear trends can be observed: an increasing SMD results in a larger lift-off Height, which is expected as droplets with a larger diameter take longer to evaporate and the flame is pushed downstream. The spray velocity shows an approximately linear positive relation with the LoH, which is consistent with expectations. A higher spray velocity causes the droplets to propagate faster through the chamber, distributing the heating process over a longer distance and hence delaying evaporation spatially. The spread parameter shows an approximate negative relation with the LoH; however, the effect is almost negligible in comparison with the effects of SMD and spray velocity.

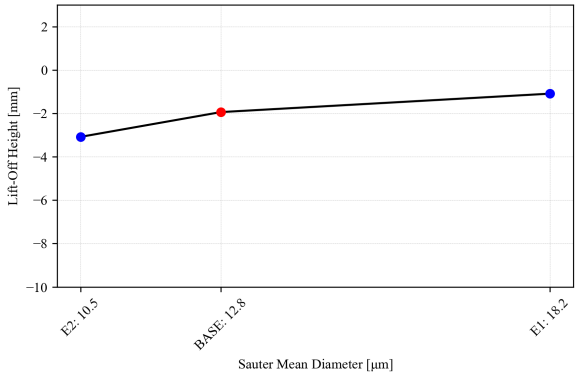

(a) Effect of Sauter mean diameter on the LoH.

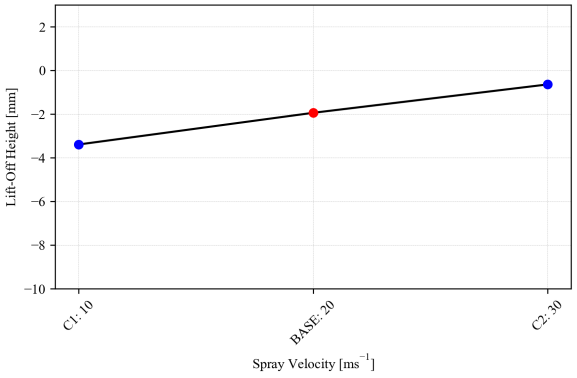

(b) Effect of spray velocity on the LoH.

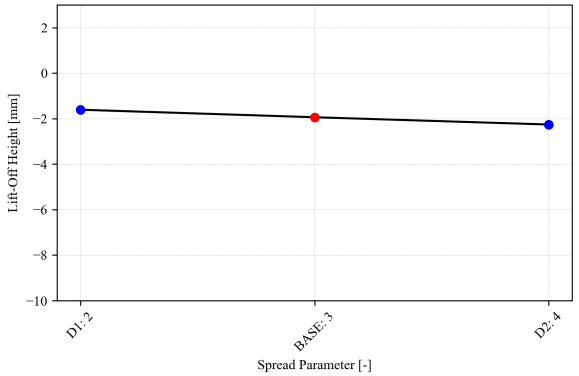

(c) Effect of spray spread parameter on the LoH

Figure 7.36: Influence of key spray parameters on the LoH

The parameters defining different spray types are represented in Figure 7.37. First consider Figure 7.37a; here, the influence of two distinct parameters, staggering and mass flow distribution, is represented. In real atomizers, droplets are not initiated from constant streams, and hence staggering adds spatial randomness in the locations from which droplets are released. Nevertheless, the influence of staggering is limited. The non-uniform mass flow type, however, does have an influence.

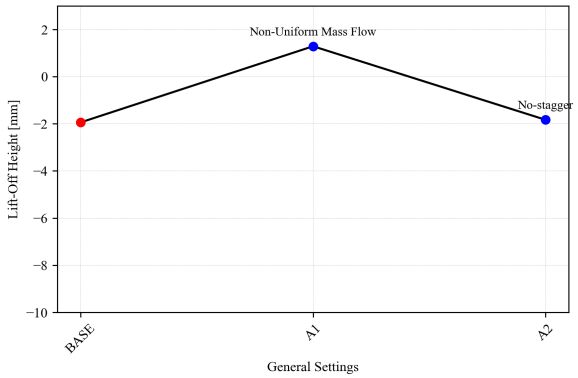

(a) Impact of injector staggering and mass flow distribution on the LoH.

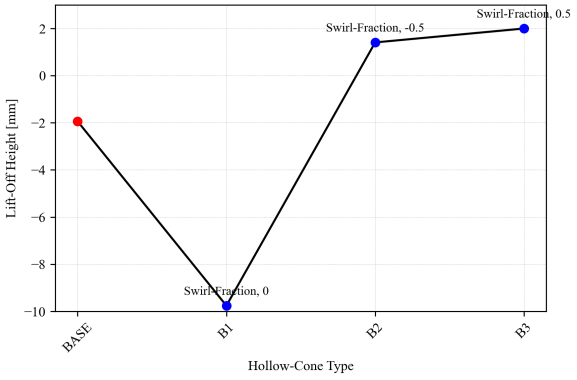

(b) Effect of hollow-cone configuration (with co-rotating, counter-rotating, and non-swirled injection) on the LoH.

Figure 7.37: Influence of spray type on the LoH

Figure 7.38 illustrates the droplet release locations. It can be noted that the arrows are much denser in the center of the cone as opposed to the outer perimeter. Therefore, providing the same mass flow results in a non-uniform

initial distribution of the flow, with more mass flow in the center. Assuming uniform flow provides more mass to the outer arrows, making the mass flow uniform on the cone surface.

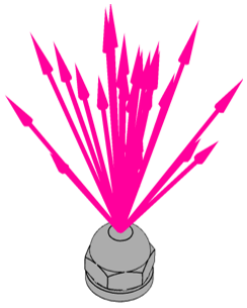

Figure 7.38: Distribution of spray parcels over the cone

The resulting effect of this mass flow distribution on the spray and PFR can be observed in Figure 7.39. The non-uniform distribution shows a downstream-extended saturated core in comparison with the uniform mass flow. Therefore, the PFR follows the same trend, forming a W-shape and increasing the LoH. The non-uniformity is purely due to the application of a constant mass flow along the parcel arrows and is therefore not an inherent physical characteristic of the system (but rather a numerical simplification), and will not be further considered.

(a) Liquid volume fraction

(b) Product formation rate

Figure 7.39: Influence of (non) uniform mass flow distribution

Consider the second sensitivity plot of Figure 7.37. In RANS-FGM, the HC shows a significant impact on the LoH, as reported in Figure 7.37b. Remarkably, the swirl fraction has a major influence, increasing the LoH. The swirl fraction is defined as the ratio of the tangential velocity component to the total velocity magnitude at injection. In Figure 7.40, the contours of the different SC/HC configurations are represented. After reconsidering the atomizer CAD and the swirler geometry, it can be concluded that the swirl is of the co-rotating type and hence the counter-rotating one is not represented. For the SC, the flame cannot propagate towards the atomizer as the region is too saturated by the liquid spray. For the HC without swirl, the LoH is actually reduced in this case, as the spray accumulates near the edges, allowing a gap that reaches the atomizer to exist. Therefore, evaporated $C_{11}H_{22}$ can oxidize from these spray outer edges and burn due to the existing gap in the center. The oxidation is rapid; hence, the V-shape is retained. The addition of a swirl fraction (considering a swirl fraction of 0.5) alters the structure of the spray significantly and the LoH is increased. Adding swirl increases the cone angle due to the higher tangential velocity. The cone angle becomes so wide at the mixing-tube outlet edge that it comes into contact with the spray, thereby disrupting the natural flow of the HC and inducing the turbulent spray as observed in the figure. The PFR field, and consequently the flame structure, is significantly altered. The direct interaction between the spray and the swirler outlet edge causes the flame to anchor at the edge itself.

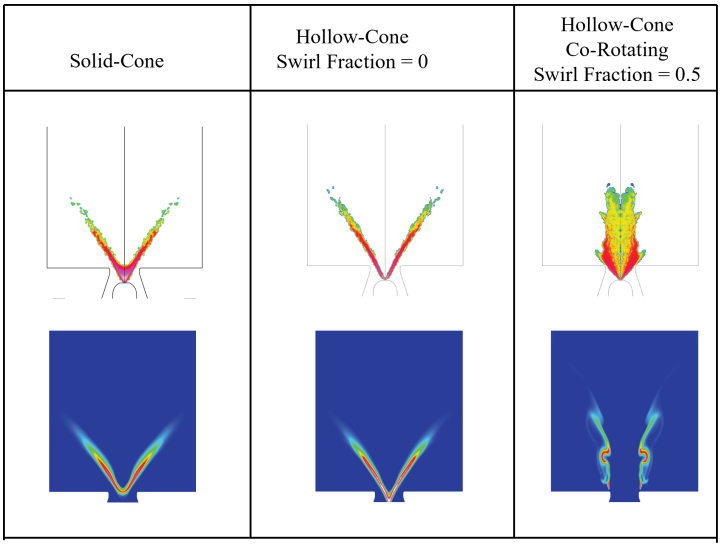

Figure 7.40: Influence of the spray cone angle on the liquid volume fraction (top row) and product formation rate (bottom row) for the solid-cone, hollow-cone and co-rotating hollow-cone

The HC justifies further investigation, as the SIMPLEX pressure atomizer employed in the experimental setup produces at least a partially HC spray and significant differences are observed in the RANS exploration. The exact swirl fraction remains unknown in the experiments and is therefore not considered here, in order to isolate the effect of the HC configuration alone. Nevertheless, it should be noted that the HC reduces the LoH in the RANS simulation, whereas an increase in LoH is desired for better correspondence with the experimental data. A high-fidelity SBES simulation at HPS_g=0.0% is performed with the setup as described in Table 6.1, now equipped with an HC. The resulting spray characteristics from the HC simulation are compared with the previously obtained baseline SC simulation. Before comparing the HC and SC, note that the SBES-retrieved spray characteristics differ considerably from the RANS results. The ”uniform” spray of Figure 7.39a and the SC of Figure 7.40 are the RANS results of the SC part of Figure 7.41a. This difference between RANS and SBES is attributed to the more sophisticated turbulence handling in SBES. The mixing in SBES is much more gradual compared to RANS. Figure 7.41a shows a different initialization between the HC and the SC. The defining characteristic of the HC can be found here, as the edge is much more saturated with liquid droplets compared to the SC, where the spray is more spread out. Due to turbulent mixing, the SBES hollow-cone simulation shows high liquid volume fractions throughout the region directly downstream of the atomizer, in contrast to the RANS result where almost no liquid fuel is present in the central region immediately downstream of the atomizer. The mixing due to turbulence further reduces the HC/SC differences downstream. Nevertheless, the liquid volume fraction of the HC remains slightly narrower than that of the SC. The SMD shown in Figure 7.41b does not show significant differences. However, the HC seems to have finer sprays near the outer edges of the spray. For both HC and SC, the largest droplets are observed further downstream. These droplets appear to persist through the evaporation process; as the overall number of droplets decreases, the average is calculated over a smaller population that increasingly includes these larger surviving droplets. As a result, the SMD peak shifts further downstream.

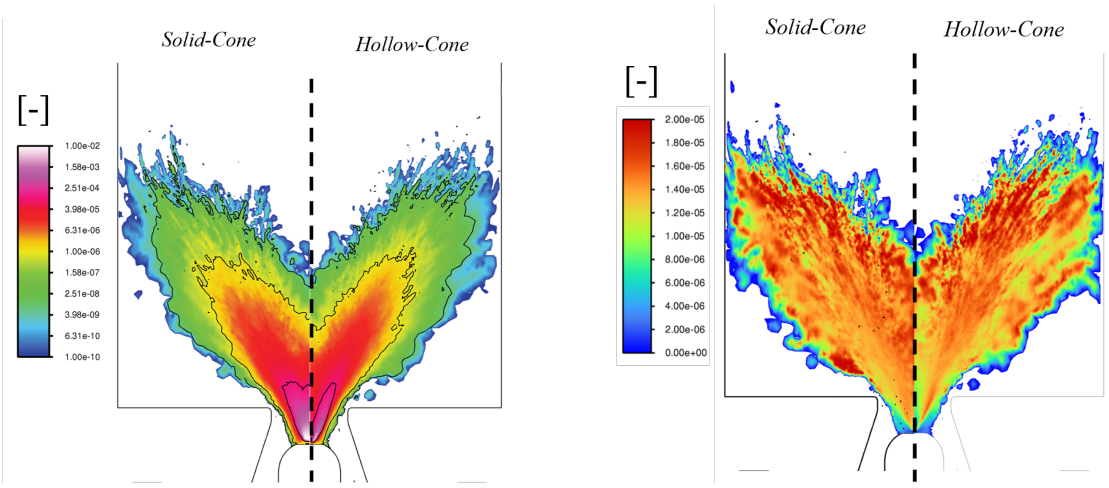

(a) Liquid volume fraction [-] **(b)** Sauter mean diameter [m]

Figure 7.41: The averaged SBES results comparing spray characteristics of hollow-cone and solid-cone injectors for HPS_g=0.0%

The different spray structures affect the distribution of $Y_{C_{11}H_{22}}$, as reported in Figure 7.42a. $Y_{C_{11}H_{22}}$ becomes available slightly further downstream in the HC case, which is attributed to the high liquid volume fraction of the HC at the outer edges directly downstream of the atomizer. The HRR is also comparable; however, moderate differences between the HC and SC are observed. The flame extends slightly further downstream, while propagating along the quartz. More HRR seems to be present in the outer shear layer for the HC, showing a clearer M-shape. Also, the flame is narrower in the HC. The most upstream region of the flame near the center axis has a steeper profile in the HC case, which can be explained by the high liquid volume on the outer edges at the initialization of the HC spray.

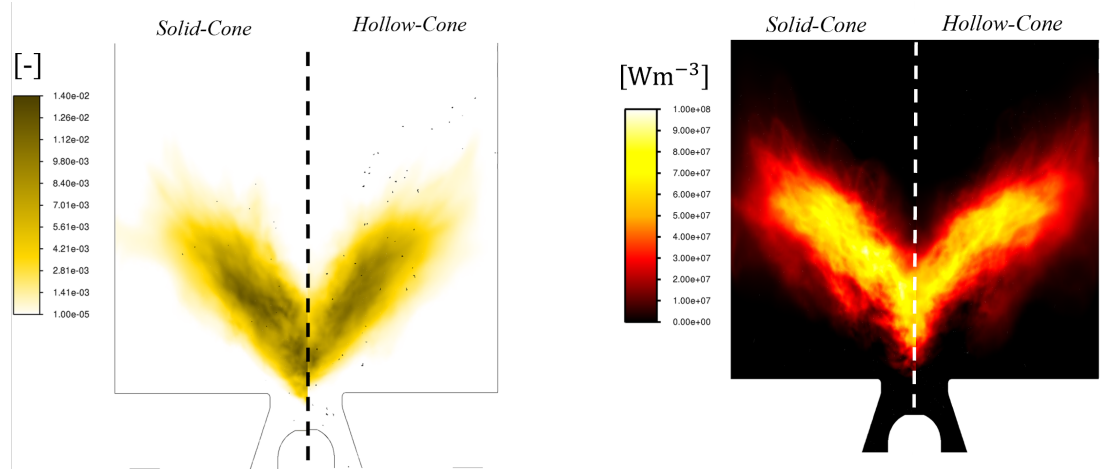

(a) Mass fraction of $C_{11}H_{22}$ [-] **(b)** Heat release rate [Wm^{-3}]

Figure 7.42: The averaged SBES results comparing the $Y_{C_{11}H_{22}}$ and HRR characteristics of hollow-cone and solid-cone injectors for HPS_g=0.0%.

Although no significant differences are found in the SBES results, the following summary can be drawn. The solid-cone configuration is schematically represented in Figure 7.43a. The grey-shaded cone in the figure indicates the SC-spray (no effects of mixing, evaporation etc.). Two flame lobes are connected by a central flame. The central flame exists because evaporation has advanced sufficiently, with the liquid volume fraction low enough to prevent droplet quenching. Further downstream, the IRZ and ORZ anchor the flame in the shear layers. For the hollow-cone case, the HC-spray is indicated by the dashed line and the case is visualized in Figure 7.43b. No substantially different behaviour is expected, as turbulence and evaporation dissolve the HC-spray structure early on. The HC

and SC configurations differ only slightly in the most upstream flame region, where the HC propagates more sharply towards the center.

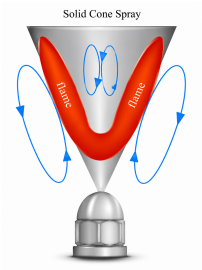

(a) Currently implemented $HPS_g = 0.0\%$ solid-cone flame stabilization.

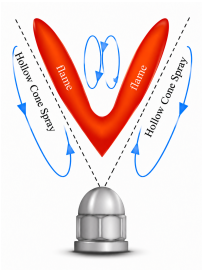

(b) Tested hollow-cone flame stabilization ($HPS_g = 0.0\%$).

Figure 7.43: Comparison of the currently implemented solid-cone and the proposed hollow-cone flame stabilization approaches.

7.3.3. Potential Improvements to the Simulation

The preceding sections investigated the influence of adiabatic wall conditions and spray boundary conditions on the simulation results. Building upon these findings, the insights obtained are now integrated to provide potential improvements for the high-fidelity SBES simulation.

Consider the $HPS_g = 0.0\%$ case again, the SIMPLEX atomizer may exhibit both hollow-cone and solid-cone characteristics (see Figure 2.5a). The combined hollow-cone and solid-cone configuration is visualized in Figure 7.44, where the solid-cone angle is drastically reduced, saturating the core and preventing the flame from anchoring in the center. This central, most upstream part of the flame (in HPS_g=0.0%) might already be weakened if the non-adiabatic BCs are applied. Furthermore, the green arrows indicate the LoH-increasing effect of the non-adiabatic boundary conditions retrieved from the previous section. An additional LoH-increasing effect can be achieved by increasing the spray velocity, which remains an uncertain parameter; however, this is unlikely to be as effective as the non-adiabatic boundary conditions. The SMD also has a LoH-increasing effect; however, as it is approximated by the Lefebvre correlation, it may be more accurately constrained than the spray velocity. Hence, the combination of the solid-cone, hollow-cone, and non-adiabatic boundary conditions is proposed as a more accurate representation of the experimental setup, likely yielding improved agreement with the experimental OH* chemiluminescence data.

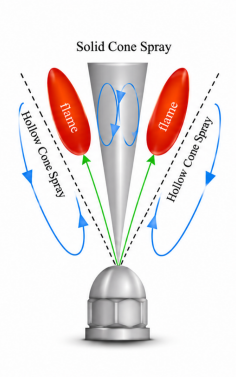

Figure 7.44: Proposed improvement: combination of solid-cone/hollow-cone injection with non-adiabatic wall boundary conditions ($HPS_g = 0.0\%$)

Now consider the multi-fuel cases. The HC/SC spray configuration is also recommended to improve agreement with the kerosene flame. As discussed in the section on adiabatic wall boundary conditions, RANS simulations with wall thermal conduction show significantly lower backplate temperatures compared to the adiabatic case. The temperature falls below the hydrogen autoignition temperature. Consequently, imposing these lower wall temperatures, especially at the backplate, may suppress upstream hydrogen oxidation and improve agreement between experimental results and SBES simulations.

7.4. Extension to Engine Operating Conditions

The pure H_2 take-off conditions are simulated, as these represent the most limiting operating conditions. The corresponding simulation setup is described in subsection 6.5.3. Prior to investigating the limiting engine operating conditions, the simulation is first performed under atmospheric conditions to assess the correspondence between the RANS predictions and the experimental data. The comparison between the RANS simulation and the experimental measurements obtained from the test rig is presented in Figure 7.45. A satisfactory agreement is observed, with both the flame length and flame position being captured accurately. As expected, the agreement between the RANS simulation and the experimental data is inferior to that obtained with SBES, as the latter reproduces the flame shape and thickness more accurately. Nevertheless, the RANS approach remains suitable for conducting exploratory analyses.

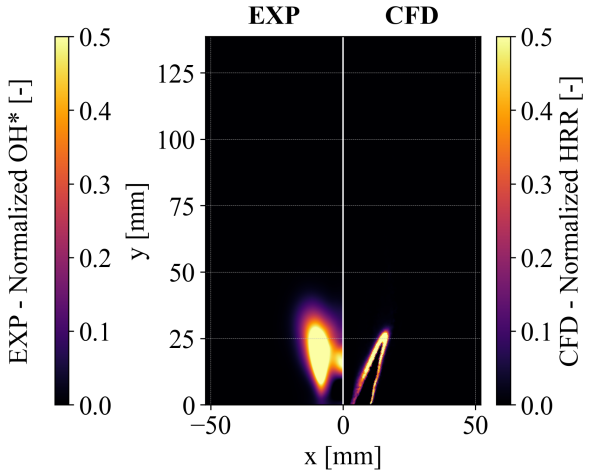

Figure 7.45: The agreement between the experimental data and the RANS simulation employing the Keromnes et al. mechanism under atmospheric conditions at HPS=100.0%

The simulation of the actual engine operating conditions has been performed, and the pressure drop is evaluated on the red plane/line represented in Figure 7.46. In the actual engine, the orifice will not be included, and therefore taking the pressure drop there would include pressure losses associated with the orifice structure. The pressure drop plane is positioned sufficiently far downstream to avoid flame influence, while maintaining adequate separation from the orifice structure and remaining within a region of relatively high mesh density. The reported pressure loss in the system is 24.55%, while reference pressure losses of annular combustors are around 6% [22]. The current pressure drop across the swirler is therefore not feasible, as the system is too inefficient.

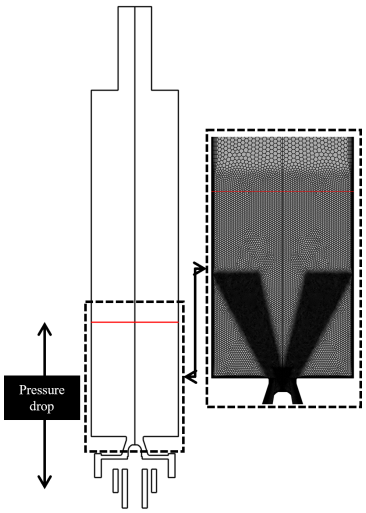

Figure 7.46: Plane of pressure drop determination

Therefore, the swirler will be scaled, by enlarging the domain and thereby reducing the pressure drop. The scaling factor is based on a similar flame condition, as reported in Equation 7.7. The axial velocity and the S_L balance each other; therefore, setting them equal may reproduce similar flame behaviour.

$$\left(\frac{\mathrm{V}_{ax}}{\mathrm{S}_L}\right)_{eoc} = \left(\frac{\mathrm{V}_{ax}}{\mathrm{S}_L}\right)_{atm} \tag{7.7}$$

The equation is evaluated at the mixing-tube exit, which has a diameter of 20 mm in the non-scaled domain. This location is selected to be upstream of the flame, as the flame is not allowed to propagate in the mixing tube, and is hence representative of the S_L-Vax balancing. At this point, the highest velocities are expected, from the continuity equation, considering the cross-sectional diameter and the mass flow. The swirler-exit area ratio of the two conditions can be determined using Equation 7.7 and the (simplified) continuity equation. The ratio can be written as shown in Equation 7.8, where the subscript eoc corresponds to the value in the scaled engine operating conditions.

$$\frac{A_{eoc}}{A_{atm}} = \frac{\dot{m}_{eoc}\rho_{atm}S_{L,eoc}}{\dot{m}_{eoc}\rho_{eoc}S_{L,eoc}} \tag{7.8}$$

The scaling factor is subsequently defined as the ratio of the two diameters, as given in Equation 7.9.

$$\varphi = \frac{D_{\mathrm{eoc}}}{D_{\mathrm{atm}}} \tag{7.9}$$

The scaling factor can be obtained by substituting the scaling relation into Equation 7.8. The S_L values for both conditions are then evaluated using CANTERA premixed freely propagating flame simulations. The corresponding mass flows are known from the simulation and can also be used in the ideal gas law, along with the known temperatures, to retrieve the densities for their corresponding conditions.

$$\varphi = \frac{D_{\mathrm{eoc}}}{D_{\mathrm{atm}}} = \sqrt{\frac{\dot{m}_{\mathrm{eoc}}\rho_{\mathrm{atm}}S_{L,\mathrm{atm}}}{\dot{m}_{\mathrm{atm}}\rho_{\mathrm{eoc}}S_{L,\mathrm{eoc}}}} = 1.61 \tag{7.10}$$

Hence, all parameters are known and the scaling factor is obtained ($\phi = 1.61$), allowing the computation of the scaled diameter ($D_{eoc} \approx 32.2$). The axial velocities of the regular domain (the non-scaled domain) and the scaled domain are compared in Figure 7.47a. The velocities in the scaled domain are significantly reduced; hence, the pressure drop is lowered to 6.64%, which is reasonable. However, the velocity magnitude is not sufficient to prevent the flame from stabilizing in the mixing-tube nozzle, and it even propagates into the swirler vane channels, as can be observed in Figure 7.47.

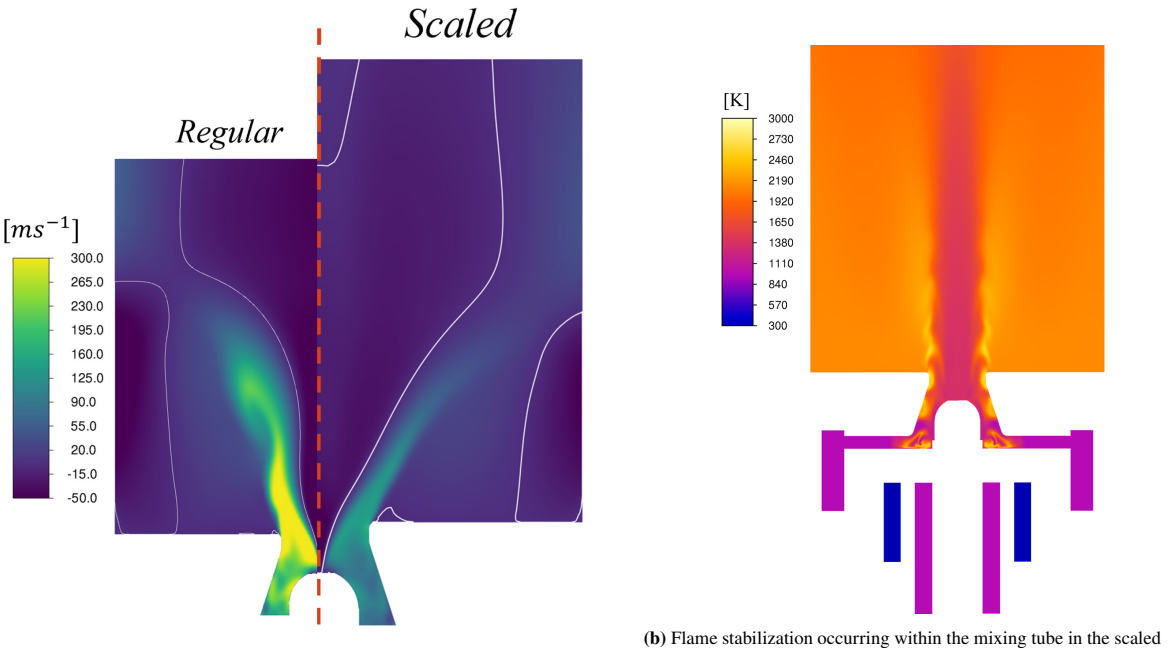

(a) Effect of scaling on axial velocity

(b) Flame stabilization occurring within the mixing tube in the scaled configuration

Figure 7.47: Influence of scaling on flame stabilization; "regular" refers to the baseline atmospheric combustion system, while "scaled" denotes the enlarged configuration intended to reduce the pressure drop.

Higher axial velocities are required to prevent flame stabilization in the mixing-tube, while the pressure drop becomes unmanageable when downscaling is applied again. A possible solution is to introduce diffusive H_2 inlets on the backplate, allowing flashback-resistant H_2 flames to partially supplement the thermal power. The swirler region can then operate at a lower power output under leaner conditions, which reduces S_L, thereby requiring a lower axial velocity to prevent flame stabilization in the nozzle and swirler. The diffusive H_2 flames are accompanied by a significant NOx penalty.

The introduction of diffusive H_2 flames and a further down-scaling of the swirler represent two opposing effects that can be balanced in an optimization framework. The swirler down-scaling increases the axial velocity, allowing for a higher S_L, at the cost of an increased pressure drop, while the diffusive H_2 flames introduce a NOx penalty. Balancing these two competing effects presents a direction for future design optimization. However, it must be noted that this concerns the most limiting condition, HPS_g=100.0% at take-off. The diffusive flames might therefore only be activated in this condition, without compromising NOx performance in different regimes, while scaling of the swirler imposes geometric constraints across all operating conditions. Furthermore, the operational range of the engine also warrants consideration, as the most limiting condition of pure H_2 take-off may not be the most frequently encountered operating point in practice. Designing for this condition may therefore compromise the overall value of the design.

8

Conclusion and Recommendation

This chapter begins by presenting the general conclusions of the study. Subsequently, each sub-question is addressed to systematically answer the main research question. Finally, the chapter provides recommendations for future work.

8.1. Conclusions

The first objective was to obtain a representative SBES-simulation for the hybrid-kerosene combustor with validation on the actual flame shape. The pure H_2 case shows good correspondence with the experiments, as the flame is anchored in both. The general structure of the pure kerosene case is captured, with a central flame region absent in the experiments, which propagates downward, thereby lowering the LoH compared to the experiments. For the dual-fuel cases, the flame is predicted as anchored, while the experiments show a lifted flame. The premature anchoring is attributed to independent H_2 oxidation near the swirler exit corners, where no or negligible kerosene is present. As a consequence, the experimental LoH trend cannot be captured, as the flame is already anchored from the 30% H_2 case onward. The flame height trend is only partially captured, although the decrease in flame length with increasing H_2 content, attributed to the higher reactivity of H_2, is reproduced. The initial decrease in cone angle in the experiments attributed to the spray deterioration is observed across the cases; however, the subsequent widening associated with upstream flame propagation cannot be captured due to premature anchoring.

Although reasonable agreement was obtained between the SBES simulations and the experimental data, the simulations could benefit from further improvements. The adiabatic wall boundary conditions and the spray boundary conditions were identified as potential sources of significant uncertainty. The non-adiabatic boundary conditions analysis revealed that the backplate temperature reaches approximately 600 K for the pure kerosene case, which is below the autoignition temperature of H_2. This contrasts with the adiabatic SBES prediction of approximately 1500 K, well above the autoignition temperature, suggesting that the non-adiabatic conditions may suppress the premature upstream H_2 combustion observed in the adiabatic simulations. Furthermore, the non-adiabatic boundary conditions weakened the central upstream flame in the pure kerosene case, improving agreement with the experimental data, as no such flame is present experimentally. The elimination of this central flame would naturally increase the LoH, as this region corresponds to the most downstream extent of the central flame. After examination of the spray boundary conditions, it was found that the current modeled solid-cone spray might not be representative of the experimental setup, as it was equipped with SIMPLEX pressure atomizers with at least partially hollow-cone characteristics. A dedicated SBES-simulation equipped with a hollow-cone showed minor differences; however, a combination of hollow-cone and solid-cone spray configurations, together with the non-adiabatic boundary conditions, is proposed as a pathway toward further improvement. The non-adiabatic boundary conditions weaken the central flame, while a solid-cone configuration with a reduced spray angle would saturate the core, potentially eliminating the central flame entirely and bringing the SBES predictions into closer agreement with the experimental data.

The second objective was to describe the kerosene–H_2 topology using high-fidelity SBES data, thereby providing improved insight into H_2–kerosene flame behaviour and the interactions between them. To this end, a suitable progress variable has been constructed based on CO_2 and H_2O for multi-fuel cases, as it provides an inherent weighting of the local fuel-mixing conditions. A flame-defining variable for multi-fuel flames has been constructed, namely the Flame Index (FI). The multi-fuel Flame Index is formulated by weighting the fuel mass gradients from the conventional definition by their corresponding lower heating values (LHV), thereby making power, rather than mass, the defining characteristic. The flame transitions from a wide, lifted spray-dominated structure in the pure kerosene case to a more compact, high-intensity anchored flame under pure hydrogen conditions. When employing H_2 and kerosene simultaneously, it was found that H_2 combustion occurs upstream of kerosene, promoting droplet evaporation and thereby assisting kerosene combustion downstream. Since H_2 requires no evaporation, it was immediately available and able to burn independently under leaner conditions, resulting in lean premixed H_2 combustion in the upstream region. Nevertheless, it must be considered that the early anchoring at the mixing-tube outlet edge due to independent upstream H_2 oxidation is not observed in the experiments. As a consequence, this may lead to upstream H_2 combustion occurring before kerosene at the more downstream located kerosene flame, as observed in the simulations. Therefore, this interaction must be reconsidered after implementing the appropriate non-adiabatic boundary conditions (especially at the combustor backplate), eliminating the early anchoring of the flame.

Further, a study was conducted to evaluate the performance of the current combustor under limiting engine operating conditions, thereby addressing the final research objective. Due to the computational complexity associated with these operating conditions, RANS simulations were adopted, resulting in a compromise in predictive accuracy compared to higher-fidelity SBES. Furthermore, no experimental validation data was available for these cases, as the primary purpose of the study was to computationally explore operating conditions. Consequently, the results should be interpreted as preliminary trend analyses rather than fully validated predictions. The current HOPE-combustor shows an unfeasibly high pressure drop at the most limiting conditions, pure H_2 take-off. Therefore, the swirler is scaled to reduce the pressure drop; however, the flame stabilises in the swirler due to the lowered axial velocity.

8.2. Answer to the Research Questions

The objective of this study was to contribute to the advancement of multi-fuel combustion in general and the HOPE combustor in particular. Liquid kerosene spray and gaseous H_2 fuel are simultaneously utilized in the HOPE combustor; however, the current understanding of their interaction remains limited in the literature. Only a limited number of studies have employed LES/SBES (Large Eddy Simulation/Stress Blended Eddy Simulation) for H_2–kerosene flames, despite their capability to resolve flame topology and reveal detailed fuel–mixing interactions. Therefore, the following main research question was formulated:

How do different hydrogen–kerosene blend ratios affect the flame topology in the HOPE combustor under atmospheric conditions, and how does the current design perform under intended engine operating conditions?

To address this, sub-questions were defined. These sub-questions are addressed below before proceeding to the main research question.

To what extent is the LES/SBES approach, coupled with the TFM model, able to capture the flame shape for various kerosene–hydrogen blend ratios?

Answer: *The LES/SBES + TFM approach captures the flame shape for pure H_2, whereas for the pure kerosene case a non-physical central flame is present. For dual-fuel cases, the model fails to reproduce the experimentally observed lifted flame, instead predicting premature anchoring due to early and independent H_2 oxidation. Nevertheless, the trend of decreasing flame height with increasing H_2 content is captured. Improvements are expected through the implementation of non-adiabatic wall boundary conditions and more realistic spray modeling (hollow and solid cone representations), which would likely weaken or eliminate the central flame and mitigate premature anchoring at the mixing-tube outlet edge.*

How can the structural features and flow properties of kerosene–hydrogen blended flames be described and quantified for various blend ratios?

Answer: *The flame transitions from a broad, lifted spray-dominated structure in pure kerosene towards a more compact, high-intensity anchored flame in the pure H_2 case. In dual-fuel operation, the flame topology analysis shows that H_2 combustion occurs upstream of kerosene, promoting droplet evaporation and thereby enhancing downstream kerosene oxidation, which subsequently proceeds in a more diffusive mode at higher equivalence ratios. For $HPS_g = 30.0\%$, the flame exhibits the most partially premixed character among the investigated cases, with most power generated at intermediate flame index values. Increasing the hydrogen content to $HPS_g = 60.0\%$ results in two dominant regions of power generation: a lean upstream H_2 flame and a second region slightly richer than the global equivalence ratio with a stronger kerosene contribution.*

What is the performance of the current combustor under the intended operating conditions, and which modifications are recommended to improve the system?

Answer: *The performance under engine conditions is evaluated for the pure H_2 take-off case, as this represents the most limiting condition. The system exhibits an unfeasibly high pressure drop. To mitigate this, the swirler is enlarged using a scaling factor, which reduces the pressure drop; however, the resulting decrease in axial velocity leads to flame stabilization within the swirler. This introduces a design challenge that requires further investigation.*

Finally, integrating the outcomes of the sub-questions allows the main research question to be addressed:

Under pure kerosene conditions, a broad spray-dominated flame is observed, which becomes progressively more compact with increasing H_2 content due to the higher reactivity of H_2. The results confirm that H_2 combustion occurs upstream of kerosene, promoting droplet evaporation and enhancing downstream kerosene oxidation, while also contributing to richer downstream combustion conditions. However, the exact H_2 power share at which flame anchoring occurs is not fully captured in CFD, most likely due to the assumption of adiabatic backplate conditions, which may alter the upstream H_2–kerosene interaction. In the pure H_2 take-off case, the combustor does not perform satisfactorily due to excessively high pressure drops; while up-scaling the design can mitigate this issue, it leads to flame stabilization within the combustor. The use of diffusive H_2 flames may be a potential strategy to enable operation under these conditions, while accepting a NO_x penalty.

8.3. Recommendations

Based on the findings of the present work, several opportunities for further investigation and model improvement have been identified. Recommendations for improving the simulations are outlined below, after which it is advised to repeat the topology analysis performed in the current study using the improved simulation framework.

- Implement the proposed non-adiabatic boundary conditions and spray boundary conditions for $HPS_g = 0.0\%$, applying both the backplate and quartz temperature profiles and introducing a combined hollow-cone/solid-cone spray. This is done to assess whether the central flame—identified as the region of largest discrepancy between the experimental data and the CFD results—will be eliminated.

- The wall temperature, particularly on the backplate, should be reconsidered for the multi-fuel cases, as the adiabatic boundary condition yields unrealistically high temperatures exceeding the hydrogen autoignition temperature. This leads to upstream hydrogen oxidation that is not observed in the experiments.

- The OH*/HRR response was shown to differ between kerosene and H_2 combustion, likely compromising direct comparison in dual-fuel flames. A correction function or alternative correction mechanism is therefore recommended for further exploration.

- Alternative flame sensor definitions might be further explored. Basing the sensor on oxygen consumption represents a promising option, as does retrieving Ω_0 from tabulated values that dynamically adjust for local mixture conditions, providing a more accurate reference. This, the flame sensor formulation is proposed by [66] and is recommended as a candidate for evaluation.

- It is recommended to investigate the influence of introducing an additional transport equation for the retrieval of α (mass-based hydrogen fraction) in order to assess the impact of the unity Lewis number assumption.

The engine operating condition study highlighted several limitations of the current HOPE combustor design, particularly under the most demanding pure H_2 take-off conditions. The following recommendations are proposed to address these limitations and guide future design iterations.

- Introduce diffusive H_2 inlets which are flashback resistant, allowing the flow through the mixing tube to be leaner, lowering the laminar flame speed, and therefore the axial velocity requirement and with that the pressure drop, however, against a NO_x penalty.

- Narrowing the swirler increases the axial velocity, which reduces the need for H_2 diffusive flames and therefore decreases NO_x formation; however, this comes at the cost of an increased pressure drop. Consequently, swirler down-scaling and the introduction of diffusive H_2 flames represent two opposing design strategies. These competing effects on axial velocity, pressure loss, and NO_x emissions warrant further investigation in a dedicated optimization study. In this context, diffusive flame operation could be selectively activated only under specific operating conditions, thereby limiting the associated NO_x penalty to those regimes, whereas swirler scaling imposes a permanent geometric constraint across all operating conditions.

- It should be noted that the considered engine condition represents the most demanding case of pure H_2 take-off. However, since this operating point is unlikely to occur frequently in practice, it may be reasonable to reconsider the requirement for full 100% hydrogen capability during take-off. Relaxing this constraint could reduce system complexity and cost, thereby improving overall market competitiveness.

- Simulate the take-off conditions for different H_2–kerosene blend ratios to assess the capability of the current HOPE combustor to operate under kerosene-based conditions. In particular, identify the minimum hydrogen fraction at which stable flame stabilization can be maintained, and determine the blend ratios at which flame instability or, in the case of unsteady simulations, flashback occurs.

References

[1] International Energy Agency (IEA). *World Energy Outlook 2024: Executive Summary*. Executive Summary Report. Licence: CC BY 4.0. Paris: International Energy Agency (IEA), 2024. URL: https://www.iea.org/reports/world-energy-outlook-2024/executive-summary.

[2] International Renewable Energy Agency (IRENA). *Sustainable Aviation Fuels in Southeast Asia: A Regional Perspective on Bio-based Solutions*. Tech. rep. Accessed October 19 2025. Abu Dhabi: International Renewable Energy Agency (IRENA), 2024. URL: https://www.irena.org/-/media/Files/IRENA/Agency/Publication/2024/Dec/IRENA_Sustainable_aviation_fuel_Southeast_asia_2024.pdf.

[3] Intergovernmental Panel on Climate Change (IPCC). *Climate Change 2023: Synthesis Report. Contribution of Working Groups I, II and III to the Sixth Assessment Report of the Intergovernmental Panel on Climate Change*. Sections from the longer Synthesis Report PDF version. Geneva, Switzerland: IPCC, 2023, pp. 35–115. DOI: 10.59327/IPCC/AR6-9789291691647. URL: https://www.ipcc.ch/report/ar6/syr/downloads/report/IPCC_AR6_SYR_LongerReport.pdf.

[4] World Health Organization. *Climate change and health*. https://www.who.int/news-room/fact-sheets/detail/climate-change-and-health. 2023.

[5] Sarah S. Abdul-Nabi. "Climate change and its environmental and health effects from 2015 to 2022: A scoping review". In: *Heliyon* 11.2 (2025), e25812. DOI: https://doi.org/10.1016/j.heliyon.2025.e42315.

[6] European Council. *The Versailles Declaration, 10 and 11 March 2022*. Informal meeting of the Heads of State or Government. Accessed: 2026-04-04. 2022. URL: https://www.consilium.europa.eu/en/press/press-releases/2022/03/11/the-versailles-declaration-10-11-03-2022/.

[7] European Commission. *Making the most of the EU's innovative potential: An intellectual property action plan to support the EU's recovery and resilience*. Communication COM(2020) 760 final. Brussels, Belgium: European Commission, 2020.

[8] European Commission. *A New Industrial Strategy for Europe*. Communication COM(2020) 102 final. Brussels, Belgium: European Commission, 2020.

[9] International Civil Aviation Organization. *Report of the Expert Group on the Long-term Aspirational Goal (LTAG) for International Aviation CO2 Emissions Reduction Options*. Tech. rep. Montreal, Canada: ICAO, 2022.

[10] International Civil Aviation Organization (ICAO). *ICAO Strategic Plan 2026–2050*. https://www.icao.int/. Approved by the ICAO Council on 1 November 2024. Montréal, Canada, 2024.

[11] Nitesh Subedi et al. "Hydrogen as an energy carrier: Production pathways, thermochemical constraints, and electrolysis-based green hydrogen prospects". In: *International Journal of Hydrogen Energy* 220 (2026), p. 154100. ISSN: 0360-3199. DOI: 10.1016/j.ijhydene.2026.154100.

[12] A. Leitão et al. "A review of hydrogen aircraft propulsion systems: Recent advances and environmental perspectives". In: *International Journal of Hydrogen Energy* 176 (2025), pp. 402–426. DOI: 10.1016/j.ijhydene.2024.12.285.

[13] International Energy Agency. *Net Zero Roadmap: A Global Pathway to Keep the 1.5 °C Goal in Reach — 2023 Update*. Tech. rep. Accessed: 2026-04-04. Paris, France: IEA, 2023. URL: https://www.iea.org/reports/netzero-roadmap-a-global-pathway-to-keep-the-15-0c-goal-in-reach.

[14] European Commission. *Consortium for the AdVent of aero-Engine Demonstration and aircraft Integration Strategy with Hydrogen (CAVENDISH)*. Grant Agreement 101102000. Project duration: 2023–2026. Horizon Europe Clean Aviation, 2026.

[15] European Commission. *Novel Fuel-Flexible ultra-Low Emissions Combustion systems for Sustainable aviation (FFLECS)*. Grant Agreement 101096436. Project duration: 2023–2026. Horizon Europe Research and Innovation Actions, 2026.

[16] European Commission. *Medium-range hybrid low-pollution flexifuel/hydrogen sustainable engine (MYTHOS)*. Grant Agreement 101096286. Project duration: 2023–2026. Horizon Europe Research and Innovation Actions, 2026.

[17] *HOPE: Hydrogen Optimized multi-fuel Propulsion system for clean and silEnt aircraft*. https://hope-eu-project.eu/. Project funded under Horizon Europe GA n° 101096275. Co-funded by UKRI under guarantee n° 10068673. 2025. URL: https://hope-eu-project.eu/.

[18] Kenneth K. Kuo. *Principles of Combustion*. 2nd. 768 pages. Hoboken, New Jersey: John Wiley & Sons, Inc., 2005. ISBN: 978-0-471-04689-9.

[19] Philippe Dagaut and Michel Cathonnet. "The ignition, oxidation, and combustion of kerosene: A review of experimental and kinetic modeling". In: *Progress in Energy and Combustion Science* 32.1 (2005), pp. 48–92. DOI: 10.1016/j.pecs.2005.10.003.

[20] Stephen Dooley et al. "The experimental evaluation of a methodology for surrogate fuel formulation to emulate gas phase combustion kinetic phenomena". In: *Combustion and Flame* 159.3 (2011), pp. 1444–1466. DOI: 10.1016/j.combustflame.2011.11.002.

[21] Jürgen Warnatz, Ulrich Maas, and Robert W. Dibble. *Combustion: Physical and Chemical Fundamentals, Modeling and Simulation, Experiments, Pollutant Formation*. 4th. Berlin, Heidelberg: Springer, 2006. DOI: 10.1007/978-3-540-45363-5.

[22] Sara McAllister, Jyh-Yuan Chen, and A. Carlos Fernandez-Pello. *Fundamentals of Combustion Processes*. New York: Springer, 2011. ISBN: 978-1-4419-7942-1. DOI: 10.1007/978-1-4419-7943-8.

[23] S. Ravi and E. L. Petersen. "Laminar flame speed correlations for pure-hydrogen and high-hydrogen content syngas blends with various diluents". In: *International Journal of Hydrogen Energy* 37.24 (2012), pp. 19177–19189. ISSN: 0360-3199. DOI: 10.1016/j.ijhydene.2012.09.086. URL: https://doi.org/10.1016/j.ijhydene.2012.09.086.

[24] Arthur H. Lefebvre and Vincent G. McDonell. *Atomization and sprays*. en. Second edition. Combustion: an international series. Boca Raton London New York: CRC Press, Taylor and Francis Group, 2017. DOI: 10.1201/9781315120911.

[25] T. D. Fansler and S. E. Parrish. "Spray measurement technology: A review". In: *Measurement Science and Technology* 26 (2015), pp. 1–35.

[26] International Civil Aviation Organization. *ICAO Environmental Report 2010*. Montreal, Canada: International Civil Aviation Organization (ICAO), 2010.

[27] David S. Lee et al. "The contribution of global aviation to anthropogenic climate forcing for 2000 to 2018". In: *Atmospheric Environment* 244 (2020), p. 117834. DOI: 10.1016/j.atmosenv.2020.117834.

[28] Arthur H. Lefebvre and Dilip R. Ballal. *Gas Turbine Combustion: Alternative Fuels and Emissions*. 3rd ed. Boca Raton, FL: CRC Press, 2010. ISBN: 9781420086041.

[29] Arvid Åkerblom, Niklas Zettervall, and Christer Fureby. "Comparing Chemical Reaction Mechanisms for Jet Fuel in Turbulent Premixed Combustion Simulations". In: *AIAA Journal* 63.9 (2025). DOI: 10.2514/1.J065162.

[30] Kaushal Dave et al. "Kerosene-H2 blending effects on flame properties in a multi-fuel combustor". In: *Fuel Communications* 23 (2025), p. 100139. DOI: 10.1016/j.jfueco.2025.100139.

[31] Joel H. Ferziger and Milovan Perić. *Computational Methods for Fluid Dynamics*. 3rd. Springer, 2002. DOI: 10.1007/978-3-642-56026-2. URL: https://doi.org/10.1007/978-3-642-56026-2.

[32] G. Boudier et al. "Comparison of LES, RANS and experiments in an aeronautical gas turbine combustion chamber". en. In: *Proceedings of the Combustion Institute* 31.2 (Jan. 2007), pp. 3075–3082. ISSN: 15407489. DOI: 10.1016/j.proci.2006.07.067. URL: https://linkinghub.elsevier.com/retrieve/pii/S1540748906000824 (visited on 10/07/2025).

[33] A. Sadiki et al. "Unsteady methods (URANS and LES) for simulation of combustion systems". en. In: *International Journal of Thermal Sciences* 45.8 (Aug. 2006), pp. 760–773. ISSN: 12900729. DOI: 10.1016/j.ijthermalsci.2005.11.001. URL: https://linkinghub.elsevier.com/retrieve/pii/S1290072905002504 (visited on 10/07/2025).

[34] Flight Safety Foundation. *FSF ALAR Briefing Note 8.3 - Landing Distances*. Tech. rep. Available via SKYbrary Bookshelf. Flight Safety Foundation, 2000. URL: https://skybrary.aero/sites/default/files/bookshelf/2478.pdf.

[35] L. Q. Maurice et al. "Advanced aviation fuels: a look ahead via a historical perspective". In: *Fuel* 80 (2001), pp. 747–756.

[36] Hamna Khalid et al. "Next generation sustainable aviation fuels powered by renewable energy". In: *Biomass and Bioenergy* 211 (2026), p. 109164. ISSN: 0961-9534. DOI: 10.1016/j.biombioe.2026.109164.

[37] Hukam C. Mongia. "GE Aviation Low Emissions Combustion Technology Evolution". In: *SAE Technical Paper Series*. 2007-01-3924. Warrendale, PA: SAE International, Sept. 2007. DOI: 10.4271/2007-01-3924.

[38] Sulabh K. Dhanuka et al. "Vortex-shedding and mixing layer effects on periodic flashback in a lean premixed prevaporized gas turbine combustor". In: *Proceedings of the Combustion Institute* 32.2 (2009), pp. 2911–2918. DOI: 10.1016/j.proci.2008.06.213.

[39] Yize Liu et al. "Review of modern low emissions combustion technologies for aero gas turbine engines". In: *Progress in Aerospace Sciences* 94 (2017), pp. 12–45. DOI: 10.1016/j.paerosci.2017.08.001.

[40] I. Staffell et al. "Energy density and storage challenges of hydrogen fuel". In: *Applied Energy* (2019). DOI: 10.1016/j.apenergy.2019.113128.

[41] *H2ELIOS Project - Liquid Hydrogen Storage for Zero-Emission Aircraft*. https://www.clean-aviation.eu/research-and-innovation/clean-aviation/clean-aviation-projects/h2elios. Clean Aviation Joint Undertaking, European Union, accessed 2026-06-25. 2023.

[42] Linyuan Huang et al. "An experimental study on the laminar burning velocities of RP-3 kerosene and its surrogate fuel at elevated pressures and temperatures". In: *Fuel* 88.8 (2009), pp. 1520–1529. DOI: 10.1016/j.fuel.2009.04.024.

[43] Chen Dong et al. "Experimental study on the laminar flame speed of hydrogen/carbon monoxide/air mixtures". In: *Fuel* 330 (2022), p. 125844. DOI: 10.1016/j.fuel.2022.125844.

[44] Francis Oppong et al. “Intrinsic instability of different fuels spherically expanding flames: A review”. en. In: *Fuel Processing Technology* 234 (Sept. 2022), p. 107325. ISSN: 03783820. DOI: 10.1016/j.fuproc.2022.107325. URL: https://linkinghub.elsevier.com/retrieve/pii/S0378382022001655 (visited on 09/19/2025).

[45] Don W. Green and Robert H. Perry. *Perry’s Chemical Engineers’ Handbook*. 8th ed. New York: McGraw-Hill, 2007.

[46] David R. Lide. *CRC Handbook of Thermophysical and Thermochemical Data*. Boca Raton: CRC Press, 1994.

[47] National Institute of Standards and Technology. *NIST Chemistry WebBook*. Accessed: 2026-04-24. 2024. URL: https://webbook.nist.gov/chemistry/.

[48] Hiroyuki Hiroyasu et al. “An Experimental Study on Kerosene-Hydrogen Hybrid Combustion in a Gas Turbine Combustor”. In: *Bulletin of JSME* 23.184 (1980), pp. 1655–1662. DOI: 10.1299/jsme1958.23.1655.

[49] G. L. Juste. “Hydrogen injection as additional fuel in gas turbine combustor. Evaluation of effects”. In: *International Journal of Hydrogen Energy* 31.14 (2006), pp. 2112–2121. DOI: 10.1016/j.ijhydene.2006.02.006.

[50] Joseph Burguburu et al. “Effects of H2 enrichment on flame stability and pollutant emissions for a kerosene/air swirled flame with an aeronautical fuel injector”. In: *Proceedings of the Combustion Institute* 33.2 (2011), pp. 2927–2935. DOI: 10.1016/j.proci.2010.07.019.

[51] J. P. Frenillot et al. “Impact of H2 addition on flame stability and pollutant emissions for an atmospheric kerosene/air swirled flame of laboratory scaled gas turbine”. In: *International Journal of Hydrogen Energy* 34.9 (2009), pp. 3930–3944. DOI: 10.1016/j.ijhydene.2009.02.059.

[52] Luigi Miniero et al. “Soot-free and low-NO combustion of Jet A-1 in a lean azimuthal flame (LEAF) combustor with hydrogen injection”. In: *Proceedings of the Combustion Institute* 39.4 (2023), pp. 4309–4318. DOI: 10.1016/j.proci.2022.08.006.

[53] Samarjeet Singh et al. “Effect of H2 and Jet-A1 fuel split on flame stability and pollutant emissions from low-swirl burner”. In: *Proceedings of the Combustion Institute* 41 (2025), p. 105858. DOI: 10.1016/j.proci.2025.105858.

[54] Kaushal Atul Dave et al. “Emission and Flame Characterization of a Novel Kerosene-H_2 Multi-Fuel Injector”. In: *Proceedings of the Combustion Institute* 42.PROCI-D-26-00957 (2026). Manuscript Draft, App: Low-Speed Propulsion.

[55] Qingyang Peng et al. “Progress in CFD numerical study on hydrogen and its blended homogeneous fuels combustion”. In: *International Journal of Hydrogen Energy* 215 (2026), p. 153806. ISSN: 0360-3199. DOI: 10.1016/j.ijhydene.2026.153806. URL: https://doi.org/10.1016/j.ijhydene.2026.153806.

[56] Gang Pan et al. “Numerical research on dual fuel combustor combustion performance”. In: *ASME Turbo Expo 2013: Turbine Technical Conference and Exposition*. Vol. 6A: Energy. San Diego, California, USA, 2013, V06AT07A015.

[57] Hongtao Zheng et al. “Effect of Dual Fuel Nozzle Structures on Combustion Flow Field in CRGT Combustor”. In: *Mathematical Problems in Engineering* 2013 (2013). DOI: 10.1155/2013/913837.

[58] V. E. Kozlov, N. S. Titova, and S. A. Torokhov. “Numerical Study of the Effect of Hydrogen or Syngas Additions to n-Decane on the Harmful Substance Emission from a Homogeneous Combustion Chamber”. In: *Russian Journal of Physical Chemistry B* 14.3 (2020), pp. 395–406.

[59] Serhiy Serbin et al. “Investigations of the emission characteristics of a dual-fuel gas turbine combustion chamber operating simultaneously on liquid and gaseous fuels”. In: *Polish Maritime Research* 28.2 (2021), pp. 85–95.

[60] Mustafa Ilbas, Osman Kumuk, and Serhat Karyeyen. “Modelling of the gas-turbine colorless distributed combustion: An application to hydrogen enriched e kerosene fuel”. In: *International Journal of Hydrogen Energy* 47.24 (2022), pp. 12354–12364.

[61] Hüsamettin Alperen Alabaş and Bilge Albayrak Çeper. “Effect of the hydrogen/kerosene blend on the combustion characteristics and pollutant emissions in a mini jet engine under CDC conditions”. In: *International Journal of Hydrogen Energy* 52 (2024), pp. 1275–1287.

[62] Chuanlong Hu et al. “Large eddy simulation of combustion characteristics during dual fuel switching process in gas turbine combustor”. In: *International Journal of Heat and Fluid Flow* 106 (2024). DOI: 10.1016/j.ijheatfluidflow.2024.109329.

[63] Faizan Habib Vance, Hendrik Nicolai, and Christian Hasse. “A numerical investigation into the stabilization of hydrogen enriched n-dodecane premixed flames”. In: *International Journal of Hydrogen Energy* 56 (2024), pp. 611–620.

[64] Lorenzo Palanti et al. “CFD-BASED SCOUTING FOR THE DESIGN OF A MULTI-FUEL KEROSENE/HYDROGEN ATMOSPHERIC BURNER”. In: *34th Congress of the International Council of the Aeronautical Sciences (ICAS)*. Florence, Italy, 2024.

[65] Lorenzo Palanti et al. “Simulation of a multi-fuel kerosene-hydrogen burner with modified Thickened Flame Model”. In: *VAD25 Springer (Submitted)* (2025).

[66] H. J. Vargas Ruiz et al. “Extension of the dynamic Thickened Flame model for partially-premixed multi-fuel multi-injection combustion and application to an ammonia–hydrogen swirled flame”. In: *Combustion and Flame* 274 (2025). DOI: 10.1016/j.combustflame.2025.113992.

[67] Daniele Pampaloni et al. “Numerical Predictions of Pollutant Emissions of Novel Natural Gas Low NOx Burners for Heavy Duty Gas Turbine”. In: *2018 Joint Propulsion Conference*. Cincinnati, Ohio, USA: American Institute of Aeronautics and Astronautics (AIAA), July 2018. DOI: 10.2514/6.2018-4562.

[68] I. M. Khan and G. Greeves. “A Method for Calculating the Formation and Combustion of Soot in Diesel Engines”. In: *Heat Transfer in Flames*. Ed. by N. H. Afgan and J. M. Beer. Washington, DC: Scripta, 1974. Chap. 25.

[69] Denis Veynante and Luc Vervisch. “Turbulent combustion modeling”. en. In: *Progress in Energy and Combustion Science* (2001).

[70] Florian R. Menter. “Stress-Blended Eddy Simulation (SBES)—A New Paradigm in Hybrid RANS-LES Modeling”. In: *Notes on Numerical Fluid Mechanics and Multidisciplinary Design*. Vol. 137. Cham: Springer International Publishing, 2018, pp. 27–37. DOI: 10.1007/978-3-319-70031-1_3. URL: https://doi.org/10.1007/978-3-319-70031-1_3.

[71] Florian Menter et al. “An Overview of Hybrid RANS–LES Models Developed for Industrial CFD”. In: *Applied Sciences* 11.6 (Mar. 2021), p. 2459. DOI: 10.3390/app11062459. URL: https://doi.org/10.3390/app11062459.

[72] Florian R. Menter. *Improved Two-Equation k-ω Turbulence Models for Aerodynamic Flows*. Tech. rep. Technical report. 1992.

[73] Franck Nicoud and François Ducros. "Subgrid-Scale Stress Modelling Based on the Square of the Velocity Gradient Tensor". In: *Flow, Turbulence and Combustion* 62.3 (1999), pp. 183–200. DOI: 10.1023/A:1009995426001. URL: https://doi.org/10.1023/A:1009995426001.

[74] R.W. Bilger, S.H. Stårner, and R.J. Kee. "On reduced mechanisms for methane–air combustion in non-premixed flames". In: *Combustion and Flame* 80.2 (May 1990), pp. 135–149. DOI: 10.1016/0010-2180(90)90122-8.

[75] Simone Castellani et al. "A general formalism for determining the unburnt composition in multi-stream species transport-based CFD simulations". en. In: *Combustion and Flame* 276 (June 2025), p. 114128. ISSN: 00102180. DOI: 10.1016/j.combustflame.2025.114128. URL: https://linkinghub.elsevier.com/retrieve/pii/S001021802500166X (visited on 09/09/2025).

[76] O. Colin et al. "A thickened flame model for large eddy simulations of turbulent premixed combustion". en. In: *Physics of Fluids* 12.7 (July 2000), pp. 1843–1863. ISSN: 1070-6631, 1089-7666. DOI: 10.1063/1.870436. URL: https://pubs.aip.org/pof/article/12/7/1843/313715/A-thickened-flame-model-for-large-eddy-simulations (visited on 09/18/2025).

[77] Lorenzo Palanti et al. "Joint Experimental and Numerical Investigation of a Multi-Fuel Hydrogen–Kerosene Burner Developed Within the HOPE Project". In: *Proceedings of ASME Turbo Expo 2026: Turbomachinery Technical Conference and Exposition*. GT2026 GT2026-179330. Milan, Italy, June 2026.

[78] V. Zimont. "Gas premixed combustion at high turbulence. Turbulent flame closure combustion model". In: *Experimental Thermal and Fluid Science* 21 (Mar. 2000), pp. 179–186. DOI: 10.1016/S0894-1777(99)00069-2.

[79] F. Charlette, C. Meneveau, and D. Veynante. "A power-law flame wrinkling model for LES of premixed turbulent combustion Part I: non-dynamic formulation and initial tests". In: *Combustion and Flame* (2002). DOI: 10.1016/S0010-2180(02)00400-5. URL: https://doi.org/10.1016/S0010-2180(02)00400-5.

[80] J-P Legier, Thierry Poinsot, and Denis Veynante. "Dynamically thickened flame LES model for premixed and non-premixed turbulent combustion". In: *Center for Turbulence Research Proceedings of the Summer Program 2000*. 2000, pp. 157–168.

[81] David Barré. "Numerical simulation of ignition in aeronautical combustion chambers". PhD thesis. PhD thesis. Université de Toulouse / Institut National Polytechnique de Toulouse, June 2014. URL: http://ethesis.inp-toulouse.fr/archive/00002619/.

[82] Alex B. Liu, Daniel Mather, and Rolf D. Reitz. "Modeling the Effects of Drop Drag and Breakup on Fuel Sprays". In: *SAE Technical Paper* 930072 (1993). DOI: 10.4271/930072.

[83] S.V. Apte, M. Gorokhovski, and P. Moin. "LES of atomizing spray with stochastic modeling of secondary breakup". In: *International Journal of Multiphase Flow* 29.12 (2003), pp. 1503–1522. DOI: 10.1016/S0301-9322(03)00111-3.

[84] Sergei S. Sazhin. "Advanced models of fuel droplet heating and evaporation". In: *Progress in Energy and Combustion Science* 32.2 (2006), pp. 162–214. DOI: 10.1016/j.pecs.2005.11.001.

[85] Wim Munters, Charles Meneveau, and Johan Meyers. "Shifted periodic boundary conditions for simulations of wall-bounded turbulent flows". In: *Physics of Fluids* 28.2 (2016), p. 025112. DOI: 10.1063/1.4941912.

[86] Ruifeng Dou et al. “Effects of contact pressure, interface temperature, and surface roughness on thermal contact conductance between stainless steel surfaces under atmosphere condition”. In: *International Journal of Heat and Mass Transfer* 94 (2016), pp. 156–163. DOI: 10.1016/j.ijheatmasstransfer.2015.11.069.

[87] Harish Gopalan, Stefan Heinz, and Michael K. Stöllinger. “A unified RANS–LES model: Computational development, accuracy and cost”. In: *Journal of Computational Physics* 249 (2013), pp. 249–274. ISSN: 0021-9991. DOI: 10.1016/j.jcp.2013.03.066. URL: https://doi.org/10.1016/j.jcp.2013.03.066.

[88] Tamás Varga et al. “Development of a Joint Hydrogen and Syngas Combustion Mechanism Based on an Optimization Approach”. In: *International Journal of Chemical Kinetics* 48.8 (2016), pp. 407–422. DOI: 10.1002/kin.21006.

[89] Alan Keromnes et al. “An experimental and detailed chemical kinetic modeling study of hydrogen and syngas mixture oxidation at elevated pressures”. In: *Combustion and Flame* 160.6 (2013), pp. 995–1011. DOI: 10.1016/j.combustflame.2013.01.001.

[90] Carsten Olm et al. “Comparison of the Performance of Several Recent Hydrogen Combustion Mechanisms”. In: *Combustion and Flame* 161.9 (2014), pp. 2219–2234. DOI: 10.1016/j.combustflame.2014.03.006.

[91] S. M. Burke et al. “An experimental and modeling study of hydrogen combustion”. In: *Combustion and Flame* (2012). NUIG hydrogen oxidation mechanism foundation work.

[92] Z. Hong.W, D. F. Davidson, and R. K. Hanson. “A comprehensive kinetic modeling study of hydrogen combustion”. In: *Combustion and Flame* (2011). Detailed H2 oxidation mechanism used in shock-tube validation studies.

[93] Combustion Research Group University of California San Diego. *Chemical-Kinetic Mechanisms for Combustion Applications (San Diego Mechanism)*. https://combustion.ucsd.edu. 2011.

[94] J. Li et al. “A comprehensive kinetic mechanism for hydrogen and syngas combustion”. In: *International Journal of Chemical Kinetics* (2015). Updated hydrogen/syngas mechanism based on earlier USC/NUIG developments.

[95] Shijun Dong et al. “A new detailed kinetic model for surrogate fuels: C3MechV3.3”. In: *Applications in Energy and Combustion Science* 9 (2022), p. 100043.

[96] Pierre Boivin. “Reduced-Kinetic Mechanisms for Hydrogen and Syngas Combustion Including Autoignition”. PhD thesis. Leganés, Spain: Universidad Carlos III de Madrid, Dec. 2011.

[97] J. A. van Oijen and L. P. H. de Goey. “Modelling of Premixed Laminar Flames Using Flamelet-Generated Manifolds”. In: *Combustion Science and Technology* 161.1 (2000), pp. 113–137.

[98] Francesco G. Schiavone et al. “On the adequacy of OH* as a heat release marker for hydrogen–air flames”. In: *Proceedings of the Combustion Institute* (2024). Received 4 December 2023; Accepted 31 May 2024. DOI: 10.1016/j.proci.2024.105248.

[99] Boris I. Loukhovitski and Alexander S. Sharipov. “A Detailed Kinetic Submechanism for OH* Chemiluminescence in Hydrocarbon Combustion”. In: *Combustion and Flame* 272 (2025), p. 113865. DOI: 10.1016/j.combustflame.2024.113865.

[100] Francesco G. Schiavone et al. “On the Adequacy of OH* as Heat Release Marker for Hydrogen–Air Flames”. In: *Proceedings of the Combustion Institute* 40.1–4 (2024), p. 105248. DOI: 10.1016/j.proci.2024.105248.

[101] Thomas Jaravel. “Prediction of pollutants in gas turbines using Large Eddy Simulation”. PhD thesis. Institut National Polytechnique de Toulouse, 2016.

[102] Ludovic Durand and Wolfgang Polifke. “Implementation of the Thickened Flame Model for Large Eddy Simulation of Turbulent Premixed Combustion in a Commercial Solver”. In: *Proceedings of ASME Turbo Expo 2007: Power for Land, Sea and Air*. Vol. 2. 2007, pp. 869–878.

[103] Benedetta Franzelli et al. “Large Eddy Simulation of combustion instabilities in a lean partially premixed swirled flame”. In: *Combustion and Flame* 159.2 (2012), pp. 621–637.

[104] Bastien Rochette et al. “A generic and self-adapting method for flame detection and thickening in the thickened flame model”. In: *Combustion and Flame* 212 (2020), pp. 448–458.

[105] Matthias Ihme, Lee Shunn, and Jian Zhang. “Regularization of Reaction Progress Variable for Application to Flamelet-Based Combustion Models”. In: *Journal of Computational Physics* 231 (2012), pp. 7715–7721. DOI: 10.1016/j.jcp.2012.06.029.

[106] H. Yamashita, M. Shimada, and T. Takeno. “A numerical study on flame stability at the transition point of jet diffusion flames”. In: *Twenty-Sixth Symposium (International) on Combustion*. The Combustion Institute, 1996, pp. 27–34.

[107] Pascale Domingo, Luc Vervisch, and Ken N. C. Bray. “Partially premixed flamelets in LES of non-premixed turbulent combustion”. In: *Combustion Theory and Modelling* 6.4 (2002), pp. 529–551. DOI: 10.1088/1364-7830/6/4/304.

[108] Agnieszka Wawrzak et al. “Hydrogen Jet Flame Control by Global Mode”. In: *Flow, Turbulence and Combustion* 112 (2024), pp. 61–83. DOI: 10.1007/s10494-023-00466-7.

[109] S. A. Ferraris and J. X. Wen. “Large eddy simulation of a lifted turbulent jet flame”. In: *Combustion and Flame* 150 (2007), pp. 320–339. DOI: 10.1016/j.combustflame.2007.04.011.

[110] Pascale Domingo, Luc Vervisch, and Julien Réveillon. “DNS analysis of partially premixed combustion in spray and gaseous turbulent flame-bases stabilized in hot air”. In: *Combustion and Flame* 140 (2005), pp. 172–195. DOI: 10.1016/j.combustflame.2004.11.006.

[111] E. Knudsen and H. Pitsch. “A general flamelet transformation useful for distinguishing between premixed and non-premixed modes of combustion”. In: *Combustion and Flame* 156 (2009), pp. 678–696.

[112] David A. Rosenberg, Patton M. Allison, and James F. Driscoll. “Flame index and its statistical properties measured to understand partially premixed turbulent combustion”. In: *Combustion and Flame* 162 (2015), pp. 2808–2822. DOI: 10.1016/j.combustflame.2015.04.007.

[113] Hesheng Bao et al. “Large Eddy Simulation of cavitation effects on reacting spray flames using FGM and a new dispersion model with multiple realizations”. In: *Combustion and Flame* 236 (2022), p. 111764. DOI: 10.1016/j.combustflame.2021.111764.

[114] E. Oldenhof, M. J. Tummers, and D. J. E. M. Roekaerts. “Ignition kernel formation and lift-off behaviour of jet-in-hot-coflow flames”. In: *Combustion and Flame* 157.6 (2010), pp. 1167–1178. DOI: 10.1016/j.combustflame.2010.01.002.

[115] Stephen B. Pope. *Turbulent Flows*. Cambridge, UK: Cambridge University Press, 2000. DOI: 10.1017/CBO9780511840531.

A

Mesh Quality

The mesh quality is assessed using three complementary criteria: the SBES shielding function, the Pope criterion, and the near-wall y^+ distribution.

Figure A.1a shows the shielding function of the SBES model, highlighting that a LES approach is adopted in the core region of the flow, while URANS is applied near the walls. For reference, the SBES stress formulation introduced in Equation 5.1 is reproduced in Equation Equation A.1. The shielding function is represented by f_{SBES}, where $f_{\text{SBES}} = 1$ corresponds to the URANS formulation and $f_{\text{SBES}} = 0$ corresponds to the LES formulation. Consequently, the value of f_{SBES} determines the local blending between the two turbulence modeling approaches.

$$\tau_{ij}^{\text{SBES}} = f_{\text{SBES}}\, \tau_{ij}^{\text{URANS}} + (1 - f_{\text{SBES}})\, \tau_{ij}^{\text{LES}} \tag{A.1}$$

Figure A.1b reports the Pope criterion [115], which is generally considered satisfied for values above 0.8. The Pope criterion is a CFD mesh quality metric used to quantify how regular and well-shaped a computational cell is relative to an ideal reference geometry. In the case of polyhedral cells, it provides a single scalar value that represents how efficiently a cell fills space and how well-balanced its face distribution is around the centroid. Values close to one indicate compact, isotropic cells with good numerical properties, while lower values indicate increasing mesh distortion, such as skewness, stretching, or uneven face distribution. In practice, the criterion is used as a general indicator of overall cell quality in unstructured meshes [115]. From Figure A.1b, it can be concluded that the Pope criterion is sufficiently met within the burner and in the most critical combustion regions.

The non-dimensional wall distance y^+ is defined as:

$$y^+ = \frac{\rho u_\tau y}{\mu} \tag{A.2}$$

where y is the distance from the wall to the first cell center, u_τ is the friction velocity, ρ is the density, and μ is the dynamic viscosity. Values of $y^+ \approx 1$ are required for wall-resolved LES values [115]. The swirler is the most critical region for resolving the near-wall boundary layer, as the strong velocity gradients lead to high wall shear stress and consequently a high u_τ. Figure A.1c shows that relatively low y^+ values are obtained throughout the domain, although they are not consistently below 1. Nevertheless, the overall y^+ level remains low, and is therefore not expected to introduce a significant source of error in the present simulations. However, a dedicated mesh sensitivity study is recommended as future work to further assess and quantify mesh independence.

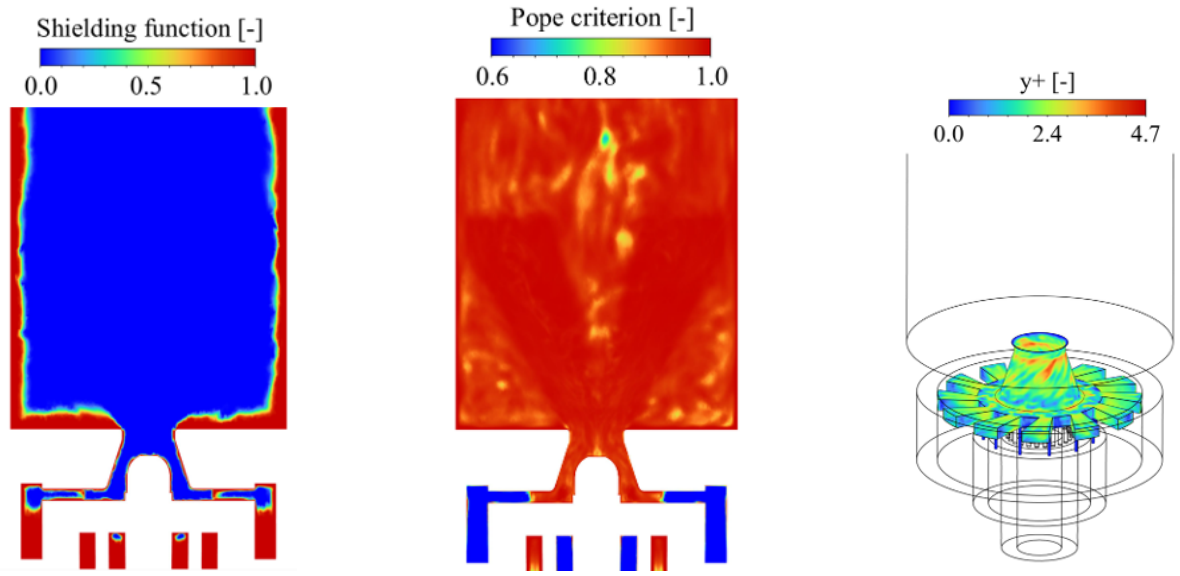

(a) Shielding **(b)** Pope criterion **(c)** y^+ distribution HPS+60.0%

Figure A.1: Mesh quality and near-wall diagnostics: shielding, Pope criterion, and y^+.

B

Contours and Sprays of the Spray Sensitivity Analysis

The sensitivity of the flame to spray modeling assumptions is assessed through a series of RANS-simulations, with the resulting flame contours and spray characteristics presented in Figures B.1 and B.2, respectively. The BASE case represents the reference configuration, corresponding to the baseline spray settings used in the original solid-cone SBES simulations.

Case A1 investigates the effect of a non-uniform mass flow distribution among injector elements. This leads to a noticeable change in flame topology, resulting in a W-shaped flame structure instead of the V-shaped flame observed in the BASE case. In Case A2, the influence of staggering the droplet release position is evaluated; however, this modification yields only negligible differences in both flame shape and spray dispersion.

Case B1 examines the impact of adopting a hollow-cone spray model. This change has a pronounced effect on the flame structure, as the V-shaped flame extends further upstream and approaches the atomizer region, indicating increased interaction between the spray and the recirculation zone. In Cases B2 and B3, variations in swirl fraction are considered. These cases show a strong sensitivity of the flame topology to swirl intensity, with significant deformation of the flame structure and direct impingement of the spray on the atomizer edges, leading to a substantially altered combustion zone.

Cases C1 and C2 explore variations in injection velocity. An increased injection velocity (C1) slightly increases the flame height due to enhanced spray penetration into the reaction zone, whereas a reduced velocity (C2) shortens the flame and weakens its axial development.

Cases D1 and D2 investigate the influence of the spray spread parameter (q = 2 and q = 4, respectively). These variations have only a minor effect on the overall flame structure and product formation rate, indicating low sensitivity to this parameter within the tested range.

Finally, Cases E1 and E2 assess the effect of the Sauter Mean Diameter (SMD). A reduced SMD (E1) leads to faster evaporation and a marginally shorter flame, while an increased SMD (E2) delays evaporation, resulting in a slightly elongated flame and increased flame height. Overall, the analysis highlights that the flame is most sensitive to spray cone structure, swirl fraction, and mass distribution, whereas parameters such as droplet release staggering and spread exponent have comparatively limited influence.

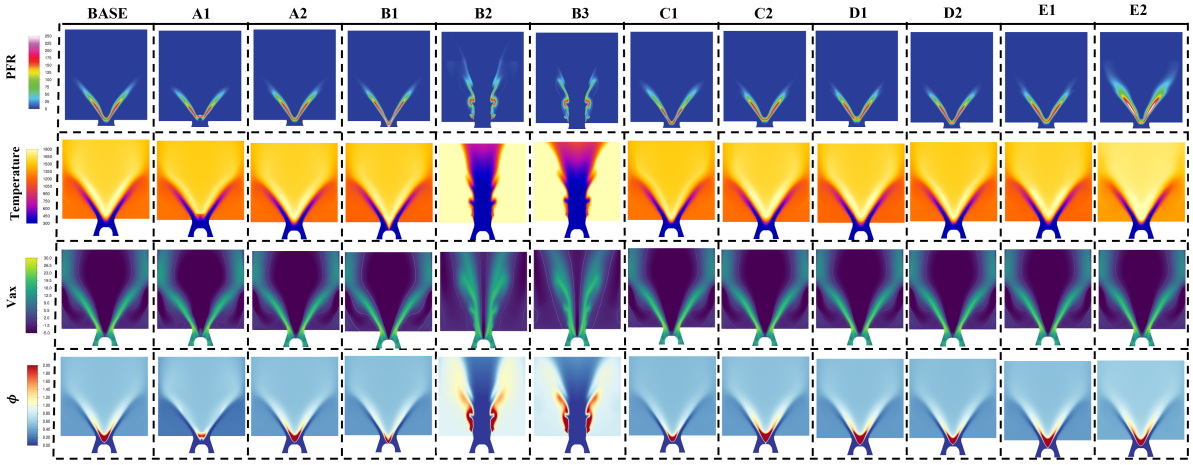

Figure B.1: Contours of the sensitivity analysis with varying spray boundary conditions

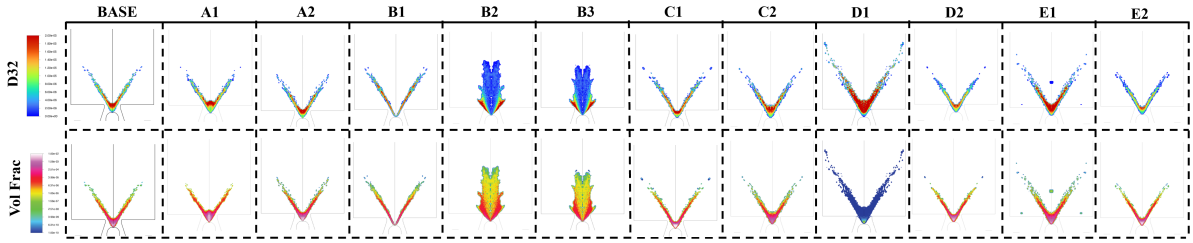

Figure B.2: Sprays of the sensitivity analysis with varying spray boundary conditions

C

Flame Sensor Performance for HPS=100.0%

In this appendix, additional considerations regarding the flame sensor are presented. First, the performance of the flame sensor is demonstrated for the pure hydrogen case. Figure C.1 shows the heat release rate (HRR), flame sensor, and thickening factor for the pure hydrogen case. The corresponding contours for HPS=60.0% are presented in Figure 7.8. It can be observed that, for HPS=100.0%, the flame sensor performs adequately and correctly captures the flame region. Pronounced thickening is observed near the atomizer outlet edge, which coincides with the region of highest heat release rate.

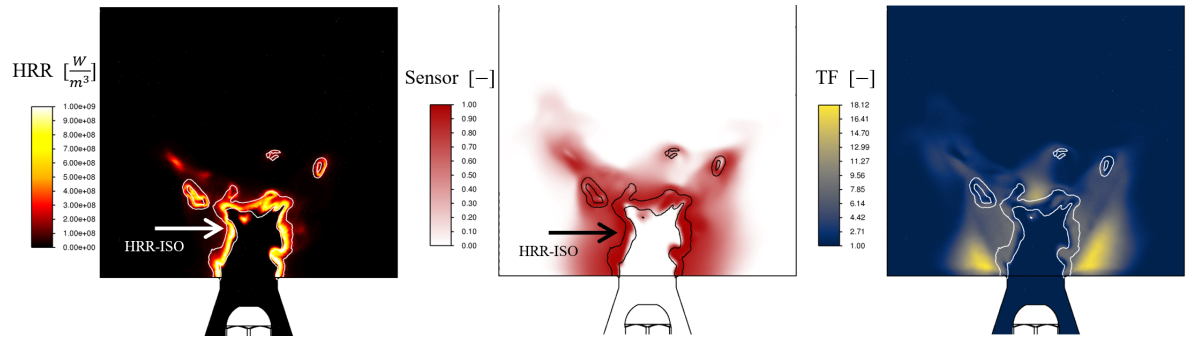

Figure C.1: Flame sensor with Ω defined based on $OH + HO_2 \rightarrow O_2 + H_2$ for atmospheric conditions and HPS = 100.0%, left the heat release rate in Wm^{-3}, middle the flame sensor [-] and right the resulting thickening factor [-].

D

Additional Considerations and Results for the Conjugate Heat Transfer Simulations

Chapter D focuses on the HPS = 0.0% case, as the agreement between SBES results and experimental data for HPS = 100.0% is already satisfactory. Nevertheless, the influence of different thermal contact conductance (TCC) values on the flame structure is assessed for the HPS = 100.0% condition. In addition, the neglect of the pre-heating effects of imposing the thermal boundary conditions on the SBES simulation will be discussed.

D.1. Conjugate Heat Transfer Results for HPS = 100.0%

The CHT method is applied for HPS = 100.0%, considering both disconnected and fully connected solid configurations, as well as the range of TCR values identified in [86]. The resulting temperature profiles are presented in Figures D.1a and D.1b for the backplate and quartz, respectively. Within the practical TCR range of 1000 to 15000, $\mathrm{Wm^{-2}K^{-1}}$, the differences between the retrieved temperature distributions are negligible for both surfaces. When the thermal contact is treated as fully disconnected, a pronounced temperature peak appears near the axis at a backplate coordinate of 0 mm, indicating flame anchoring within the injector and impingement on the atomizer. In contrast, the remaining CHT configurations do not exhibit this behaviour, as the central flame region is displaced further downstream. A small temperature discontinuity is observed around the backplate position of 30 mm, which is attributed to imperfect thermal contact between the two solid blocks. The discontinuity intensifies with decreasing TCC and vanishes completely in the full-solid case. Finally, the radially outer solid region exhibits higher temperatures than the central region, consistent with the elevated thermal conditions in the outer recirculation zone (ORZ).

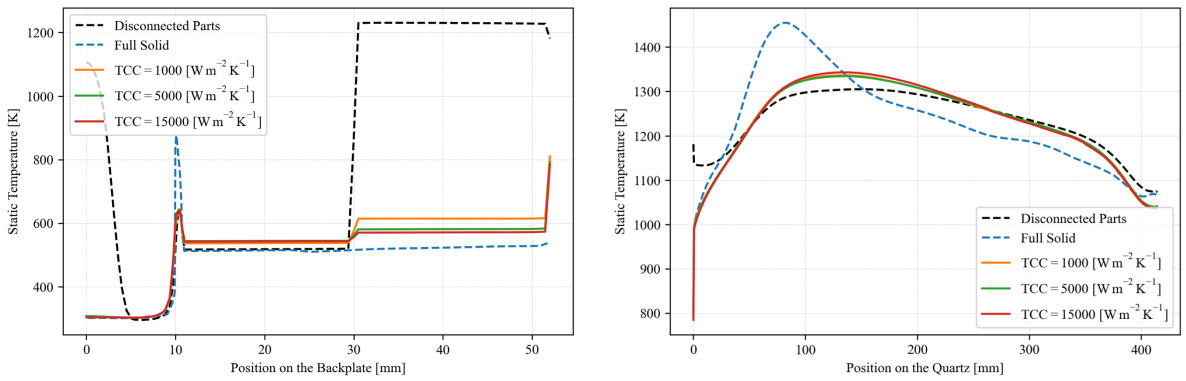

(a) Backplate **(b)** Quartz

Figure D.1: Resulting thermal boundary conditions at HPS = 100%

The flame structure primarily governs the quartz temperature, and for $1000 \leq \text{TCR} \leq 15000$, a comparable flame shape is obtained, resulting in similar temperature distributions, as shown in Figure D.2. A value of $TCC = 5000$, $\text{Wm}^{-2}\text{K}^{-1}$ is ultimately selected based on estimates of contact pressure, surface roughness, and temperature conditions.

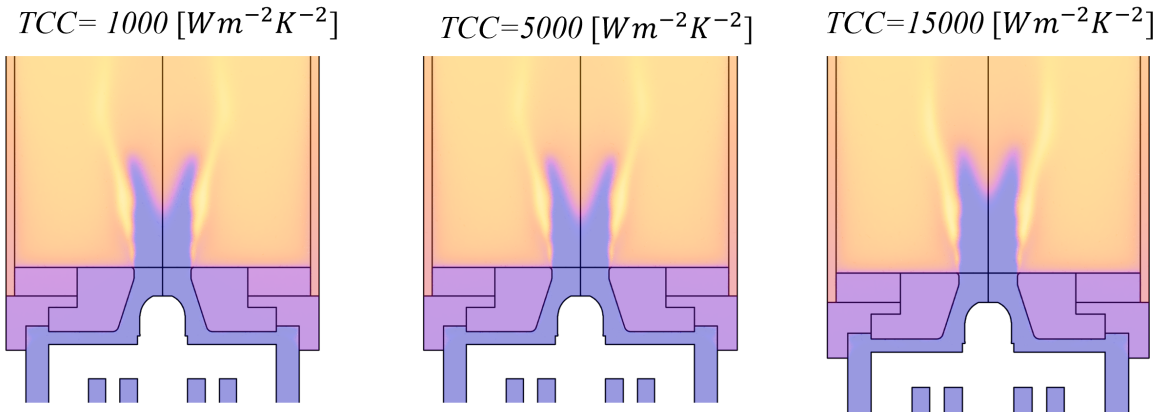

Figure D.2: CHT result flame-shapes for HPS = 100%

D.2. Pre-heating Considerations

Figure D.3a illustrates the method used to impose the retrieved boundary conditions from the CHT simulation onto the SBES case. The solid blocks are removed for clarity, revealing that the backplate temperature is significantly lower than the surrounding fluid domain, as indicated by the predominantly blue on the surface. In this setup, only the backplate temperature and quartz wall profile are retained, while solid-phase heat conduction effects are neglected. As a result, pre-heating of the incoming flow is not represented in the SBES model, as no heat conduction through the solid structures is accounted for, in contrast to the CHT results (see Figure D.3b). In the CHT simulation, heat is conducted through the solid components towards the nozzle, swirler, and plenum, leading to measurable pre-heating of the incoming mixture. Although this effect is absent in the SBES boundary condition treatment, its influence on the overall flame behaviour is expected to be limited, as the associated temperature increase is spatially confined and not sufficiently extensive to significantly alter the global flame structure or lift-off height (LoH).

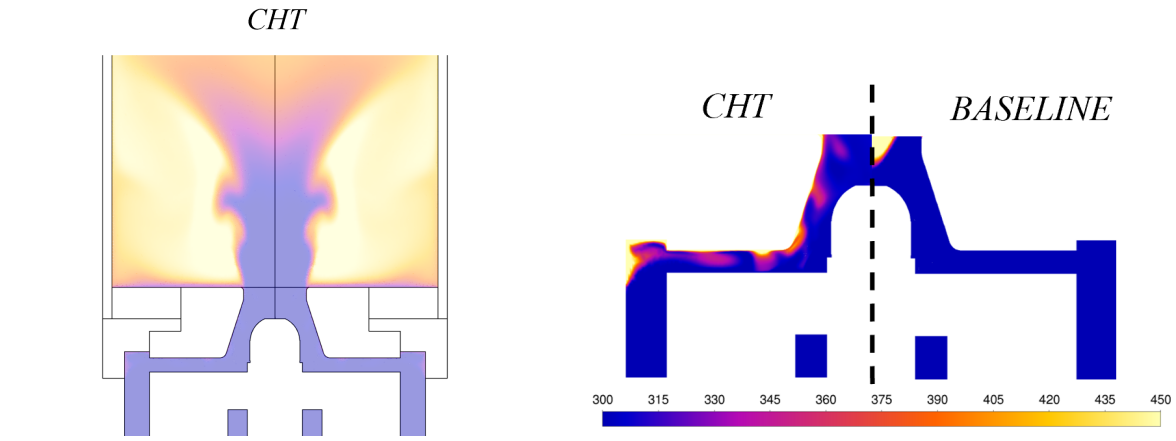

(a) Imposing the boundary conditions from CHT (showing a temperature profile)

(b) Temperature [K] in the nozzle and ducts showing pre-heating due to heat conduction

Figure D.3: Thermal boundary conditions application in SBES and pre-heating effects HPS=0.0%